



Bergische Universität Wuppertal
Fachbereich Mathematik und Naturwissenschaften
Fachgruppe Physik

Enhanced Field Emission from Metallic Surfaces and Nanowires

Dissertation zur Erlangung des Doktorgrades
des Fachbereichs Physik der Bergischen Universität Wuppertal

Arti Dangwal

Wuppertal
02 November 2007
WUB-DIS 2007- 08

Diese Dissertation kann wie folgt zitiert werden:

urn:nbn:de:hbz:468-20070849

[<http://nbn-resolving.de/urn/resolver.pl?urn=urn%3Anbn%3Ade%3Ahbz%3A468-20070849>]

Abstract

Metallic surfaces free from enhanced field emission (EFE) are prerequisite for getting the optimum performance of high-voltage vacuum devices such as superconducting niobium radiofrequency cavities for e^+e^- accelerators. With the advancement of surface preparation and cleaning techniques, high performance of superconducting multi-cell cavities with surface fields typically up to 50 MV/m have been achieved. However, the onset of field emission at higher fields still imposes the limitation for future linear accelerators like the European X-ray Free Electron Laser and International Linear Collider. Therefore, systematic field emission investigations were performed on broad area copper and niobium cathodes by means of dc field emission scanning microscope, which has been modernized recently for fast scans.

Dry ice cleaning is found to suppress EFE from polycrystalline Cu and Nb and single crystal Nb surfaces more efficiently than the conventionally used high pressure water rinsing. The cleaning effects on the emitting sites were investigated up to the fields of 250 MV/m. The number density of emitters at given fields was drastically reduced by dry ice cleaning. Fowler-Nordheim parameters are partially discussed with respect to the morphology and impurity content of the emitters localized by means of a high resolution scanning electron microscope equipped with energy dispersive x-ray spectroscopy. The microscopy results prove the effective removal of field-emitting particulates down to 400 nm as well as the partial smoothing of surface protrusions by the use of this technique.

Measurements on high purity single crystal and large grain Nb samples showed the effects of surface preparation on EFE, with its onset observed at high fields (120 – 200 MV/m), due to very smooth surfaces. A low temperature (~ 150 °C) heat treatment in high vacuum for 14 hours on a selected large grain Nb sample gives the evidence for the grain boundary assisted field emission at very high fields above 250 MV/m. An interesting correlation between sizes of all investigated emitters derived from SEM images with respect to their respective onset fields has been found, which might facilitate the quality control of superconducting radio-frequency cavities for linear accelerators.

Electron field emission from nanostructures has attracted wide attention in vacuum micro/nano-electronics. Besides various nanostructures, metallic nanowires have been investigated for this purpose. Copper, nickel and gold nanowires of varying wire lengths, diameters and number densities were deposited electrochemically in to the pores of etched ion-track membrane. Electric field maps on Ni nanowire cathodes show up to 10 % of deposited wires as emitters. Thin gold coating on Cu and Ni nanowires has improved the cathode emission properties in terms increased emitter number density and better emission stability. Stable Fowler-Nordheim-like emission was obtained on average up to the currents of ~ 8 μ A for individual emission site on Au coated Ni nanowire sample.

Au nanowire cathodes yielded up to 40% of deposited nanowires as emitters. A controlled field enhancement β with the small spread factor (1.23) of individual emitting sites was achieved for thin Au nanowire cathode. The emission current density up to 78 mA/cm² was obtained from agglomerated Au nanowire cathode without any current saturation. Linear dependence of β on electrode spacing d has been established for all Au nanowire cathodes.

Contents

Abbreviations

1. Introduction	1
References	4
2. Theoretical background	7
2.1. Fowler-Nordheim (FN) theory for field emission (FE)	7
2.2. Models for enhanced FE from metallic surfaces	10
2.2.1. Metallic Microprotrusion (MM) model	11
2.2.1.1. Geometrical field enhancement for metallic nanowires	13
2.2.2. Screening effect	14
2.2.3. Metal-Insulator-Vacuum (MIV) model	15
2.2.4. Metal-Insulator-Metal (MIM) model	17
2.2.5. Adsorbate effects	18
2.3. Conditioning effects	20
2.3.1. Current conditioning	20
2.3.2. Breakdown conditioning	22
2.3.3. Gas conditioning	23
2.3.4. Heat treatment	24
2.3.5. Current conditioning and pressure effects on metallic nanowires	24
2.4. Avoiding enhanced FE from metallic surfaces	26
References	28
3. ‘DC field emission scanning measurements on electropolished niobium samples’	31
3.1. Introduction	32
3.2. Experimental	32
3.3. Results and Discussion	34
3.4. Conclusions	39
References	40
4. ‘Effective removal of field-emitting sites from metallic surfaces by dry ice cleaning’	41
4.1. Introduction	42
4.2. Experimental techniques	43
4.3. Results and Discussion	45
4.3.1. Statistical reduction of FE by DIC	45
4.3.2. FN analysis and stability of emitters	48
4.3.3. Morphology and composition of emitters	51
4.4. Conclusions	54
References	56
5. ‘Field emission from single crystal and large grain niobium cathodes’	59
5.1. Introduction	60
5.2. Sample preparation and surface quality control	61

5.3. Field emission results and discussion	63
5.3.1. Statistical overview of the emitters	63
5.3.2. Grain boundary effects and low temperature heat treatment	66
5.3.3. Single emitter investigations	66
5.3.4. Intrinsic FE measurements	68
5.3.5. Emitter size vs. onset electric field (E_{on})	69
5.4. Conclusions	70
References	71
Addendum to chapter 3, 4 and 5	73
6. 'Field emission of copper nanowires grown in polymer ion-track membranes'	79
6.1. Introduction	80
6.2. Experimental	81
6.3. Results and Discussion	82
6.4. Conclusions	87
References	88
7. 'Field emission properties of bare and gold-coated nickel nanowires grown in polymer ion-track membranes'	91
7.1. Introduction	92
7.2. Experimental techniques	92
7.3. Results and Discussion	94
7.4. Conclusions	99
References	100
8. 'Field emission properties of electrochemically deposited gold nanowires'	101
References	109
Summary and outlook	111
Appendix A	115
Appendix B	117
Appendix C	119
Acknowledgements	121

Abbreviations

AES	Auger Electron Spectroscopy
AFM	Atomic Force Microscope
BCP	Buffered chemical polishing
CEA	Commissariat Energie Atomique
CNT	Carbon Nanotube(s)
CryNb	Crystalline Nb
DC	Direct current
DESY	Deutshes Elektronen-synchrotron
DIC	dry ice cleaning
E	Electric field
EDX	Energy Dispersive X-ray Analysis
EFE	Enhanced field emission
E_{acc}	Accelerating electric field
E_{max}	Maximum electric field, maximum effective field
E_{on}	Onset electric field
E_{surf}	Surface electric field
EP	Electropolishing
FE	Field Emission
FED	Field Emission Display
FEM	Field Emission Microscope
FESM	Field Emission Scanning Microscope
Fig.	Figure
FLASH	Free-electron LASer in Hamburg
FN	Fowler-Nordheim
GPIB	General Purpose Interface Bus
h	Height
HPR	High pressure ultra pure water rinsing
HT	Heat treatment
I	Current
ILC	International linear collider
J	Current density
LGNb	Large grain Nb

MAFIA	Solution of the Maxwell equations by the Finite Integration Algorithm
MIV	Metal – insulator – vacuum
MIM	Metal – insulator – metal
N	Emitter number density
n.m.	Not measured
NW	Nanowire
p	Pressure
PC	Personal Computer
PID	Proportional-Integral-Derivative
r	Radius
RF	Radio Frequency
RIA	Rare isotope accelerator
S	Effective emitting surface
SCNb	Single crystal Nb
SEM	Scanning Electron Microscope
SNS	Spallation neutron source
t	Time
T	Temperature
Tab.	Table
TESLA	TeV Superconducting Linear Accelerator
UHV	Ultra High Vacuum
V	Voltage
XFEL	X-ray free electron laser
XRD	X-ray Diffraction
α	Anode geometric field correction factor
\emptyset	Diameter
Φ	Work function
β	Field enhancement factor

Introduction

The electron field emission from cold metal surfaces by intense electric field was first observed by R. W. Wood [1] in 1897. W. Schottky [2] in year 1923 made the first attempt to explain the phenomenon, based on classical theory, but it was found experimentally that the fields capable of initiating electron emission are 10-50 times lower than that suggested by this theory. In 1928, R. H. Fowler and L. W. Nordheim gave a theory of field emission based on quantum mechanical tunneling of electrons through the surface potential barrier, which accurately describes the dependence of emission current on the electric field and work function.[3] An important development in the study of field emission was the invention of the field emission microscope by E. W. Müller in 1936.[4] In 1940, R. Haefler used transmission electron microscope to study emitter's shape and emitting area and made more accurate field calculations. Fowler-Nordheim (FN) theory was experimentally proved by E. Müller and R. Haefler for clean W tips and showed for the first time field emission occurring at $\sim 3\text{GV/m}$. [5, 6]

Electron field emission from broad-area (cm^2) metal surfaces appears to be completely different. They start to emit at fields up to 1000 times smaller than predicted by FN theory. [7] Emission does not take place on the whole electrode surface, but is restricted to some micron-sized sites. Experimentally, enhanced field emission (EFE) from an individual site appears to obey FN theory, provided effective parameters are introduced: multiplying the applied electric field by a factor β of the order of 100, and the effective area of emission S must be taken in the range of $10^{-17} - 10^{-12} \text{ m}^2$. These parameters are reasonable for assuming the emitting site as a sharp conducting protrusion. Many mechanisms have been proposed to explain the EFE from broad area cathodes, [8-10] but only microprotrusion model has obtained confirmation.

Field emission is a fundamental limitation in high-voltage vacuum devices such as superconducting niobium cavities in particle accelerators operating at high accelerating field gradient ($\sim 30 \text{ MV/m}$).[11] For such high accelerating gradients the cavity surface must be capable to sustain high surface electric fields ($\sim 2 \times$ accelerating fields). However, in regular accelerating structures, field emission often limits the cavity performance above 20 MV/m surface fields. Excessive heating from field emission current increases exponentially with field, thus making FE loaded structures unattractive especially for superconducting cavities. To systematically investigate the causes of enhanced field emission, a direct current field emission scanning microscopes have been built in several labs (at Geneva in 1980, Wuppertal in 1993 and Newport News in 2002).[12-14] The microscopic analysis has shown that EFE

sites are frequently associated with micron or submicron particulates and surface irregularities, with or without impurity inclusions.[15-18] The strength and number of emission sites strongly depends on the preparation history and handling of the surface.

Enormous technological efforts have been made over past three decades to develop specialized procedures for suppressing the onset of EFE from cavity surface. Careful surface preparation and advanced cleanliness techniques like high pressure ultra pure water rinsing (HPR) have improved the regular cavity performance at high accelerating gradients, e.g. up to about $E_{acc} = 30$ MV/m for nine-cell 1.3 GHz structures [19]. An approach towards improving the cavity fabrication for future linear accelerators like X-ray free electron laser [20] and international linear collider [21] has been made by using large grain or single crystal Nb instead of regularly used polycrystalline Nb. Recently reported preliminary tests of single cell cavities made from large grain Nb have yielded E_{acc} up to 45 MV/m, which is one of the highest gradients in superconducting cavities achieved yet. [22]

Electron field emission from nanostructures has attracted intensive attention as cold cathodes for many vacuum microelectronic applications [23]. The most familiar structure of a cold cathode is an array of microtips or ‘Spindt tips’ named after Capp Spindt who first described the fabrication of these structures in 1968 [24]. An apparently successful field emission display was fabricated by Kupryashkin *et al.* in 1991 [25], and later in 1995 by Tcherepanov *et al.* using graphite containing pastes [26].

The discovery of carbon nanotubes in year 1991 [27, 28] and first report of their field emission properties by Rinzler *et al.* in 1995 [29], had opened a new era in this field. A triode electron gun device was fabricated with a nanotube cold cathode [30], followed by a sealed nanotubes containing fluorescent display module [31], and a fully sealed single-walled nanotube based field emission display by Samsung [32]. However, mass-production and uncontrolled growth of carbon nanotubes has always posed a problem, particularly if a batch containing similar sizes and similar microstructures is required. Besides carbon nanotubes, different semiconductor [33-35] and metallic [36-39] nanowires grown by various methods have been investigated for field emission applications. Electrodeposition process is found suitable for large scale synthesis of metallic nanowires with well defined aspect ratios. However, the research is going on world wide to know about the best material and optimized growth conditions for optimum performance of the field emission devices.

The goal of the present work is to study the enhanced field emission from metallic surfaces for improved cavity performance in accelerators, and from metallic nanowires for cold cathode applications. Automization of existing field emission scanning microscope

(FESM) using LabVIEW 7.1[®] was the first step for faster measurements and data analysis. Broad area niobium and copper cathodes with different surface preparations and cleaning techniques were investigated by means of dc FESM under UHV conditions, SEM, AFM, FRT Profilometer and XRD. Our results have shown the high quality performance of dry ice cleaned samples and strengthen for its use in accelerator industry. Advantages of large grain or single crystal niobium surfaces over the polycrystalline ones have also been focused. In our study, highest onset fields for field emission were observed for single crystal niobium samples. On the other hand, electrochemically deposited metallic nanowires of Cu, Ni and Au of varying geometries were measured and optimized for their field emission applications. The investigated broad area cathodes were fabricated in Deutsches elektronen-synchrotron (DESY) Hamburg and nanowires in Technischen Universität Darmstadt and Gesellschaft für Schwerionenforschung (GSI) Darmstadt.

References

- [1] R.W. Wood, *Rhys. Rev.* 5(1), 1 (1897).
- [2] W. Schottky, *Z. Physik* 14, 63 (1923).
- [3] R. H. Fowler, L. W. Nordheim, *Proc. Royal Soc.(London) A* 119, 173 (1928).
- [4] E. W. Müller, *Z. Physik* 106, 541 (1937).
- [5] E. W. Müller, *Z. Physik* 108, 668 (1938).
- [6] R. Haefer, *Z. Physik* 116, 604 (1940).
- [7] R. J. Noer, *Appl. Phys. A* 28, 1 (1982).
- [8] N. K. Allen, B. Cox and R. V. Latham, *J. Phys. D* 12, 969 (1979).
- [9] K. H. Bayliss and R. V. Latham, *Proc. Royal Soc.(London) A* 403, 285 (1986).
- [10] N. S. Xu and R. V. Latham, *J. Phys. D* 19, 477 (1986).
- [11] R. V. Latham, *High Voltage Vacuum Insulation: Basic concepts and technological practice* (Academic Press, London, 1995).
- [12] Ph. Niedermann, These No 2197, University of Genf/Switzerland (1986).
- [13] E. Mahner, Dissertation, WUB-DIS 95-7, University of Wuppertal (1995).
- [14] T. Wang, C. E. Reece, and R. M. Sundelin, *Rev. Sci. Instrum.* 73, 3215 (2002).
- [15] N. Pupeter, Dissertation, WUB-DIS 96-16, University of Wuppertal (1996).
- [16] E. Mahner, N. Minatti, H. Piel, and N. Pupeter, *Appl. Surf. Sci.* 67, 23 (1993).
- [17] T. Wang, C. E. Reece, and R. M. Sundelin, *J. Vac. Sci. Technol. B* 21, 1230 (2003).
- [18] A. Dangwal, G. Müller, D. Reschke, K. Floettmann, and X. Singer, *J. Appl. Phys.* 102, 2007.
- [19] G. Ciovati, *Proc. LINAC 2006, Knoxville, Tennessee USA*, p. 818.
- [20] <http://xfel.desy.de>
- [21] <http://www.interactions.org/linearcollider>
- [22] P. Kneisel, G. R. Myneni, G. Ciovati, J. Sekutowicz, and T. Carneiro, *Proc. 2005 Part. Acc. Conf., Knoxville, Tennessee*, p3991.
- [23] G. Fursey, *Field emission in vacuum microelectronics*, (Kluwer Academic/ Plenum Publishers, New York, 2005).
- [24] C. A. Spindt, *J. Appl. Phys.* 39, 3504 (1968).
- [25] A. S. Kupryashkin, V.A. Seliverstov, A.G. Shakhovskoy, And E.P. Sheshin, *Proc. 4th Int. Vac. Micro. Conf.*, 124 (1991).
- [26] A. Y. Tcherepanov, A.G. Chakhovskoi, And V.B. Sharov, *J. Vac.Sci. Technol. B* 13, 482 (1995).

-
- [27] S. Iijima, *Nature*, 354, 56 (1991).
- [28] T.W. Ebbesen And P.M. Ajayan, *Nature* 358, 220 (1992).
- [29] A.G. Rinzler, J.H. Hafner, P. Nikolaev, L. Lou, S.G. Kim, D. Tomanek, P. Nordlander, D.T. Colbert, And R.E. Smalley, *Science*, 269, 1550 (1995).
- [30] W.A. De Heer, A. Chatelain, And D. Ugarte, *Science* 270, 1179 (1995).
- [31] Y. Saito, K. Hamaguchi, S. Uemura, K. Uchida, Y. Tasaka, F. Ikazaki, M. Yumura, A. Kasuya, And Y. Nishina, *Appl. Phys. A* 67, 95 (1998).
- [32] W.B. Choi, D.S. Chung, J.H. Kang, H.Y. Kim, Y.W. Jin, I.T. Han, Y.H. Lee, J.E. Jung, N.S. Lee, G.S. Park, And J.M. Kim, *Appl. Phys. Lett.* 75, 3129 (1999).
- [33] A. M. Morales and C. M. Lieber, *Science* 279, 208 (1998).
- [34] X. Duan, Y. Huang, Y. Cui, J. Wang, and C. M. Lieber, *Nature* 409, 66 (2001).
- [35] X. Duan, C. M. Lieber, *Adv. Mater.* 12, 298 (2000).
- [36] T. C. Wong, C. P. Li, R. Q. Zhang, and S. T. Lee, *Appl. Phys. Lett.* 84, 407 (2004).
- [37] B. E. Alaca, H. Sehitoglu, and T. Saif, *Appl. Phys. Lett.* 84, 4669 (2004).
- [38] R. S. Chen, Y. S. Huang, Y. M. Liang, C. S. Hsieh, D. S. Tsai, and K. K. Tiong, *Appl. Phys. Lett.* 84, 1552 (2004).
- [39] F. Zhang, R. Barrowcliff, G. Stecker, W. Pan, D. Wang, and S. Hsu, *Jpn. J. Appl. Phys.* 44, 398 (2005).

2. Theoretical background

Field emission (FE) is the phenomenon of ejection of electrons from the surface of a solid caused by strong electric fields lying in the range of 10^9 - 10^{10} V/m. The first generally accepted explanation of FE was given by Fowler and Nordheim for metal-vacuum interface, which was based on quantum mechanics. Fowler-Nordheim (FN) theory describes the quantum mechanical tunnelling of electrons through the modified surface potential barrier that results from the presence of high external electric field acting on an atomically-clean metal surface. Experimental observations on FE from flat metal surfaces and nanostructures differ strongly, though the basic theory behind it remains the same. Various models have been proposed for the deviations from original FN theory. The geometry and characteristics of microstructures present on the flat metallic surface, adsorption of gas atoms on the surface and geometry of the nanostructures are the key factors influencing the emission.

FE from metallic surfaces imposes the major limitation for various applications and is detrimental to the high voltage vacuum devices such as superconducting cavities for high gradient accelerator applications like TESLA [1]. That is why it is needed to be suppressed by studying the cause of its origin. On the other hand, enhanced field emission from the nanostructures, such as carbon nanotubes and semiconductor or metallic nanowires, has emerged to be very useful for the application in the field of vacuum micro/nano electronics. [2] Thus our present study on enhanced field emission has the two fold goals: firstly, to suppress FE from metallic surfaces to avoid the failure risks in high voltage applications, and secondly, to optimize metallic nanowires as cold cathodes with improved FE properties.

2.1. Fowler-Nordheim (FN) theory for field emission (FE)

In Fowler and Nordheim theory, the conduction electrons in the metal are treated as a gas of free particles obeying the Fermi-Dirac statistics. The metal surface is taken to be planar and the calculations are performed for zero kelvin temperature. In the absence of any electric field, electrons energies are less than the work function ϕ required for them to escape and so electrons are confined to the metal by the infinitely thick potential barrier at the metal-vacuum interface. In the presence of an electric field, the original potential barrier is deformed into a triangular, finite thickness barrier. The triangular barrier is further lowered and rounded at its tip due to the image force i.e. the attractive force generated between emitted electrons and the conducting surface. The shape of potential barrier is thus

where j is in A/cm^2 , work function ϕ in eV, E in MV/m , constants $A = 154$, $B = 6830$ and $t(y)$ and $v(y)$ are tabulated functions [3], which depend on the relative reduction of the barrier through the image charge

$$y = \frac{\Delta\phi}{\phi} = \frac{3.79 \cdot 10^{-6} \sqrt{E}}{\phi} \quad \dots (5)$$

$t(y)$ in the pre-exponential factor of FN formula is close to unity and varies weakly with argument while $v(y)$ varies significantly with y . Often used estimations are $t^2(y) = 1$ and $v(y) = 0.95 - y^2$, which are set equal to unity if the image charge is ignored.

The other form of FN formula in terms of tunnelling current through the barrier is written as:

$$I(E) = j(E) \cdot S = \frac{ASE^2}{\phi t^2(y)} \exp\left[-\frac{B\phi^{3/2}}{E} v(y)\right] \quad \dots (6)$$

with I as tunnelling current through barrier and S as the emitting area. For a rough approximation, taking Nordheim functions equal to unity, the plot of $\ln(I/E^2)$ versus $1/E$ yields a straight line, known as Fowler-Nordheim (FN) plot.

For a typical metallic surface with ϕ of 4.5 eV (e.g. for W), electric fields of the order of 10^9 MV/m are needed to get measurable emission currents. An increase in E of only a factor of 2 from 1×10^9 MV/m to 2×10^9 MV/m increases the current density by 15 orders of magnitude, i.e. from 10^{-18} to 10^{-3} A/cm^2 , which is due to rapid variation of the exponential function.

For non zero temperatures, the above theory must be modified to take into account the thermal excitation of electrons above Fermi level. As the excited electrons will observe a narrower surface barrier than those at Fermi level, they will have a higher tunnelling probability. In practical terms, this implies that the FE current density would be expected to show strong temperature dependence at high temperatures. [4] For $T < 1500\text{K}$, the temperature assisted FE current density $j(E, T)$ can be accurately described by the expression:

$$j(E, T) = j(E, 0) \frac{\pi p}{\sin(\pi p)} \quad \dots (7)$$

where $j(E, 0)$ is given by (2.4) and p is a dimensionless temperature and field dependent parameter given by

$$p \approx 9.3 \times 10^5 \times \phi^{1/2} \times (T/E) \quad \dots (8)$$

However, at higher temperatures, where $p > 2/3$ the approximations leading to the above expression become invalid and the tabulated data by Christov have to be used. [4]

FN formula was confirmed by a number of experiments on clean metal tips, but not found suitable for flat metallic surfaces. For niobium ($\phi \approx 4$ eV), equation 2.6 predicts that field levels on the order of 3 GV/m are required to achieve microampere emission currents from the emission area of $0.01 \mu\text{m}^2$. In fact, field emission currents on the order of microamperes are generally observed from Nb flat surface at fields about or below 40 MV/m. Nevertheless the observed emission current follows the Fowler-Nordheim law, provided one makes the substitution of $(\beta \cdot E)$ for all occurrences of E [5], stating that electric field is enhanced by a factor of β at the site of emission, and β is called field enhancement factor. So, we get the modified Fowler Nordheim formula for the enhanced field emission (EFE):

$$I(E) = \frac{AS\beta^2 E^2}{\phi \cdot t^2(y)} \exp\left[-\frac{B\phi^{3/2}}{\beta E} v(y)\right] \quad \dots (9)$$

$$y = \frac{\Delta\phi}{\phi} = \frac{3.79 \cdot 10^{-6} \sqrt{\beta E}}{\phi} \quad \dots (10)$$

Generally, β lies in the range $50 < \beta < 1000$ and S values in the range of $10^{-18} \text{ m}^2 < S < 10^{-9} \text{ m}^2$ have been observed. Though more careful direct current (dc) FE studies in past even showed S values as low as 10^{-22} m^2 and as high as 10^{-4} m^2 [6]. Thus, β and S can not be deduced from physical geometry of the field emitters alone. Nevertheless β and S work as the fit parameters in FN formula, and provide a valuable means of characterizing the emission current.

2.2. Models for enhanced FE from metallic surfaces

The basic principle of field emission is understood, but the mechanisms for physical processes associated with broad area metallic surfaces are still lacking. The electron emission from a broad-area metallic cathode is localized at some tens of sites per cm^2 , each with a diameter which appears to be not greater than some $10 \mu\text{m}$ and may well even much smaller. Some models have been developed to describe various experimental findings and deviations from FN theory: Metallic microprotrusion (MM) model, Metal – Insulator – Vacuum (MIV) model, and Metal – Insulator – Metal (MIM) model. [4] The emission mechanism envisaged by all these models are all associated with various types of ‘contaminating’ microstructures that are found on the surface of typical high voltage cathode surfaces.

2.2.1. Metallic Microprotrusion (MM) model

According to this model, electrons are assumed to be field emitted from the tip of a microprotrusion on the surface of a broad-area cathode, such as shown in Fig. 2, where the macroscopic gap field is geometrically enhanced to a higher microscopic value at the tip of the protrusion. The ratio of the microscopic to macroscopic fields is defined as the field enhancement factor β , with its magnitude depending on the geometry and dimensions of a given protrusion. Number of simple projection geometries was used to calculate the values of β . Various calculations have been carried out by for a hemispheroidal projection [7] and for a cylindrical projection capped by a hemisphere [8]. For each of these geometries, Tab.2.1 and Fig. 2 show the relative dimensions necessary for the range of observed values of β . It can be seen that very sharp projections are needed in order to account for the smallest observed β , whatever the geometry assumed.

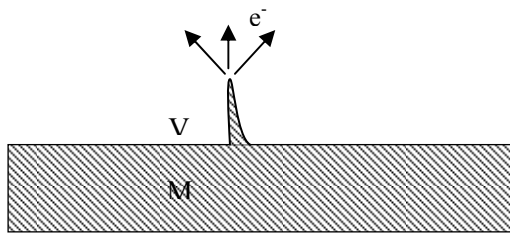


Fig. 2: Schematic illustration for a microprotrusion on a metallic surface.

β	Spheroid		Cylinder
	h/r	h/R	h/r
10	9	3	8
100	256	16	98
1000	3600	60	998

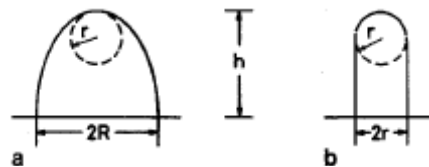


Table. 2.1: Dimensions for different geometries of Fig.3.

Fig. 3: Projection geometries assumed in Table 2.1 for (a) spheroid and (b) cylinder capped with hemisphere.[11]

Generally it has been shown that if the β factors are computed as a function of h/r , the ratio of their height h to tip radius of curvature r , they can be characterized to a good approximation by the following expression:

$$\beta \approx 2 + \frac{h}{r} \quad \dots (11)$$

provided $h/r \geq 5$. [4]

The Field enhancement factors calculated for simple structures are typically $\beta \leq 10$. [9, 10] However, values of β for emitters found in FE studies range from $\beta = 100 - 1000$ [11]. It is very rare that geometric structures with aspect ratios required for β values up to 1000 could be identified in FE measurements from metallic surfaces. Higher β values can be obtained for geometric structures with moderate aspect ratios if we assume that a small whisker is present on the tip of a larger one (see Fig.4). According to this protrusion-on-protrusion model, the β values of each structure roughly multiply to give the overall

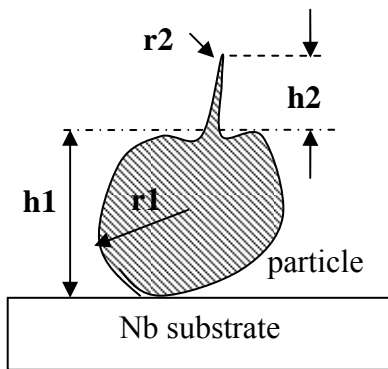


Fig.4: Schematic illustration for protrusion-on-protrusion.

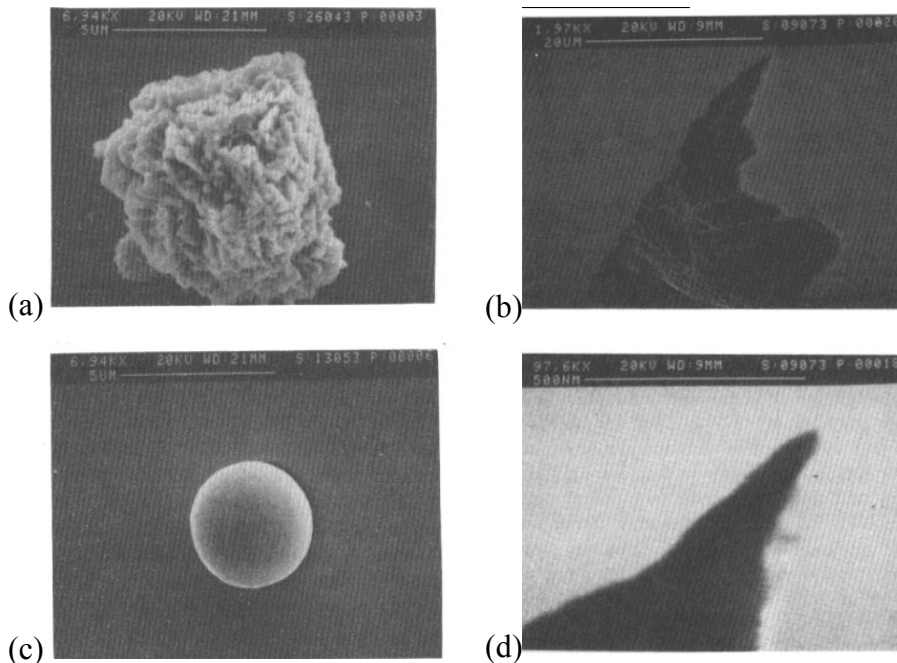


Fig.5: (a) DC field emitting nickel particle. Emission was recorded at fields as low as 20 MV/m. (b) Spherical nickel particle of $\beta \approx 4$, found not to emit up to 120 MV/m in the same experiments. (c), (d) Geometrical defect with two superposed projections (threshold field 15 MV/m). [9]

enhancement factor. [9] If each whisker has a β value of 10, then the total enhancement factor is close to 100. Studies at Saclay have indeed shown that artificially introduced particles with jagged edges (Fig.5 (a)) and also scratches (Fig.5 (b, d)) emitted with β values as given by their projections, whereas smooth spherical particles (Fig.5 (c), $\beta \approx 4$) did not emit. [9]

There were many observations inconsistent with the simple geometric explanation of electron field emission. For example, the unphysical values for S . Values of $S = 10^{-4} \text{ m}^2$ are many orders of magnitude larger than the largest emission sites found, and $S = 10^{-22} \text{ m}^2$ is equally unphysical because the emission region would have to be subatomic in size. Furthermore, it was found in dc experiments that despite their similar geometric appearance only a small fraction (5 – 10 %) of all particles present on a niobium surface field emit. [12, 13]

In some cases, field emitters have been shown to suddenly activate irreversibly. This cannot be explained by geometric field enhancement. Such events can be precipitated by administering gases, like oxygen, to the cavity. [14] Another observation inconsistent with geometric field enhancement is the fact that field emission from niobium surfaces can be deactivated by vacuum baking the sample to 1400 °C. [6, 12, 13] One might believe that geometric defects become less acute due to the heat treatment. However, subsequent heating to 200 – 600 °C activates many emitters, thereby ruling out that hypothesis.

2.2.1.1. Geometrical field enhancement for metallic nanowires

Nanowires exhibit diameters in the nanometer range and lengths in the micrometer range, so they provide high aspect ratios which generate large electric field enhancements for FE at low operation voltages, required for the application, e.g., in FE flat panel displays. Similar to the case of micro protrusions on the flat metallic surface, the microscopic field at the tip of metallic nanowire is enhanced by a factor β depending on the wire length and tip radius. For a simple example, considering a metallic nanowire as a conducting cylinder with half sphere on the top as shown in Fig.6 (a), the field enhancement factor is given by $\beta \approx h/r$. However, it is also found that for well defined nanostructures, e.g. metallic nanowires deposited electrochemically, the experimentally retrieved values of β are higher than the predicted ones.

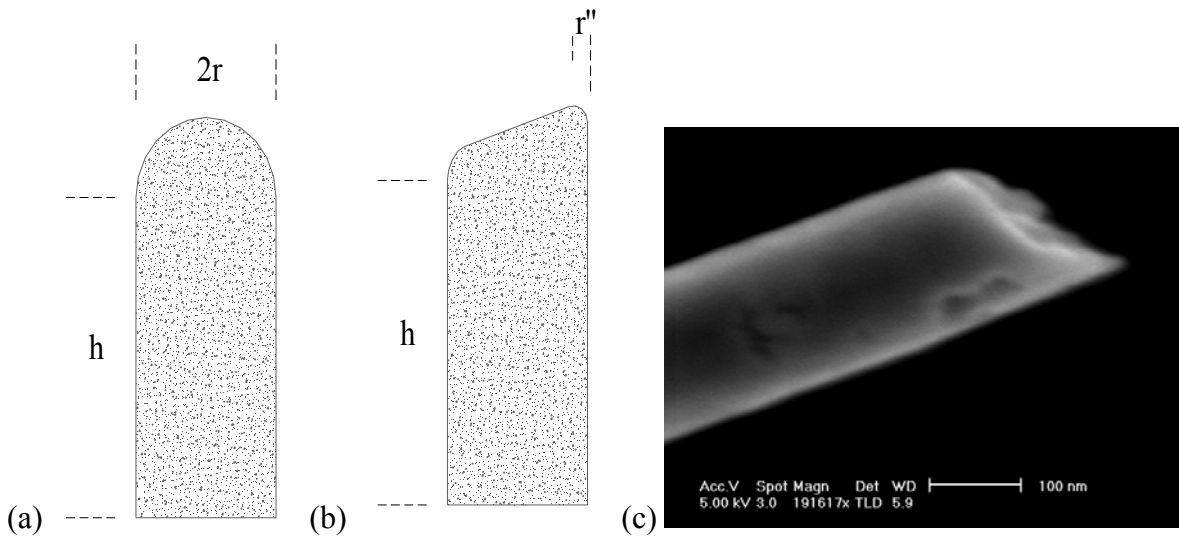


Fig.6: (a) Ideal case of a well defined nanowire structure, (b) generally observed form of nanowires with sharp edge radius r'' at the tip (c) SEM image of Au nanowires tip.

Widely different shapes of nanowire tips with sharp edge radius as shown in Fig.2.6 (b), might account for the higher values of β . The sharper edge features at the tips of metallic nanowires, deposited by electrochemical method, have been confirmed by SEM images, as shown in Fig.6 (c). Thus, the effective β becomes larger than the geometrically retrieved β value, given by $\beta = h/r''$, for the geometry given in Fig.6 (b).

2.2.2. Screening effect

For carbon nanotubes, it is found that the height and the inter emitter distances have strong influence on the emission current density and highly dense emitter arrays are not optimal field emitters due to mutual screening effect. [15-17] The equipotential lines over the emitters change due to neighbouring emitters in the manner shown in Fig.7 (a), and thus the corresponding field enhancement factor β is also affected strongly by the variation in inter-emitter distances. The observations, as shown in Fig.7 (b), show that the field amplification drops rapidly for inter-emitter distances $l \leq 2h_0$, where h_0 is the emitter length. Since the density of emitters increases with decreasing distance, there is an optimum distance for a maximal current density equal to one to two times of the emitter heights. [16, 17] Nilsson et al. [16] observed a rather inhomogeneous emission pattern on low density films.

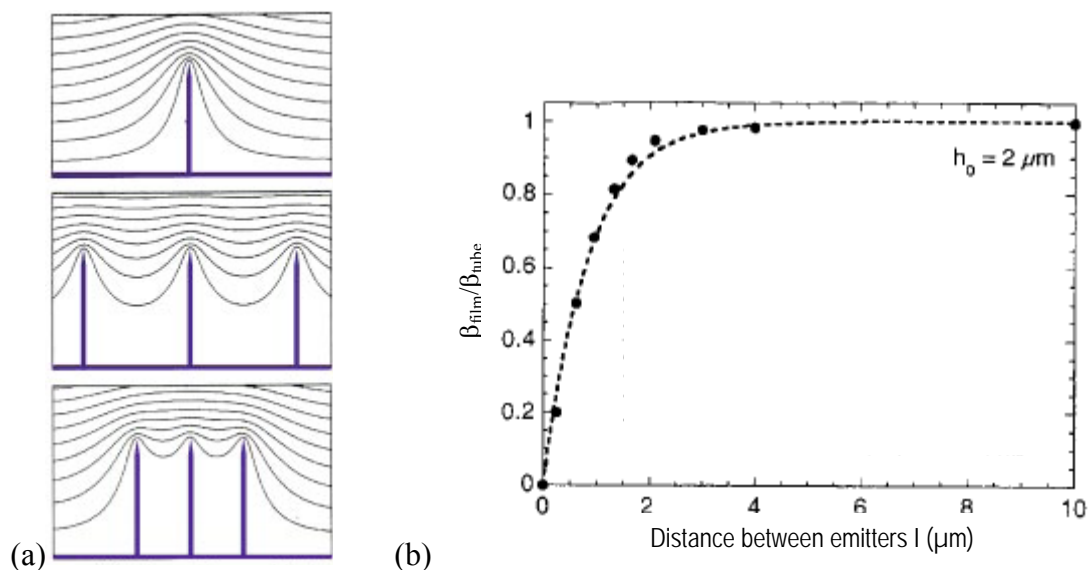


Fig. 7: (a) Electrostatic simulation of the equipotential lines for carbon nanotubes emitters [15], (b) Dependence of the enhancement factor ($\beta_{film}/\beta_{tube}$) on the inter-tube distance I for different carbon nanotubes samples, reported by Bonard [17]. β_{tube} corresponds to single nanotube, while β_{film} correspond to the entire emitter array. The dashed line is simulated curve for fitting.

The emission was far more homogenous for medium density films as all the features of the patterns could be clearly detected. High density films yielded results comparable to the low density ones but with an emitted current higher by one order of magnitude. Thus, for optimum performance of the FE devices, it is important to optimize the fabrication parameters i.e. length, radius and density of nanostructure emitters.

2.2.3. Metal – Insulator – Vacuum (MIV) model

Latham and co-workers have proposed MIV model, which assumes that an insulator is present on the metallic surface in the form of foreign inclusion or an anomalously thick oxide aggregation. In MIV system, the electrons can not emit even when the surface potential barrier at the insulator-vacuum interface is narrow enough for conduction electrons to tunnel through it, since, very few electrons exist behind the barrier. Thus, for the occurrence of FE in this system, a ‘switch-on’ is required to give rise to a steady state emission current. Switch-on process is illustrated in Fig.8, which shows that no significant current is measured in a vacuum gap formed by fresh electrodes until a sudden jump occurs in the current, when a site is said to be ‘switched-on’. Once the emitter is switched-on, it shows a reversible I-V characteristic of steady emission.

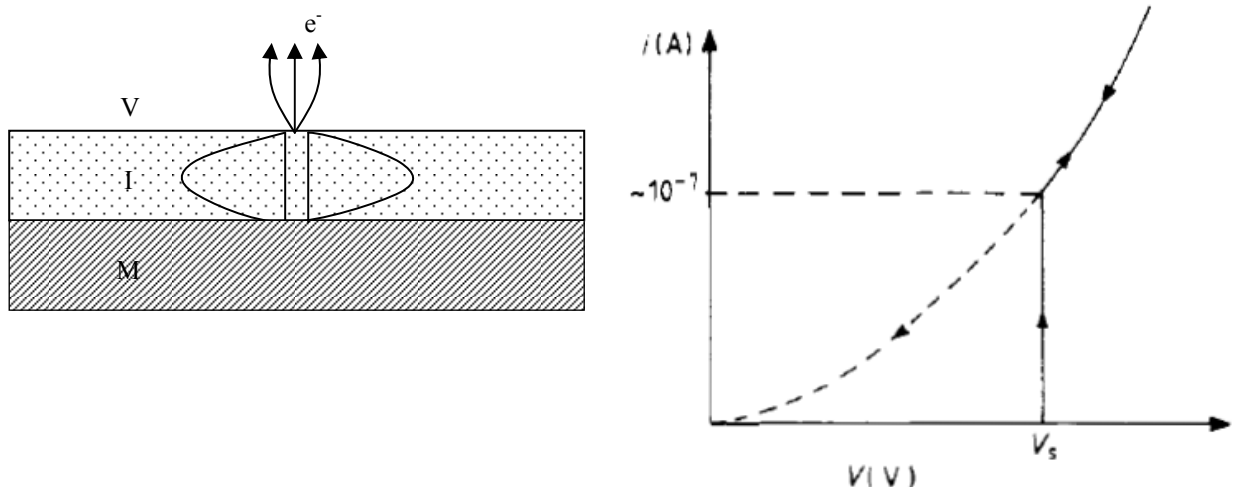


Fig.8: (a) schematic illustration for electron emission in a MIV system, (b) The current-voltage characteristic associated with a switch-on of an emitter: V_s is the switch-on voltage for a given gap setting. [18]

For this model, Latham and co-workers have used the energy band diagram, as shown in Fig.9. The blocking contact at the metal-insulator interface under zero field conditions prevents the injection of electrons into the insulator. However, when an electric field is applied it penetrates the insulator, and at sufficiently high fields electrons can be injected into the conduction band of the insulator. In the insulator region, the electrons gain energy (are heated) by the electric field and are emitted thermionically into the vacuum at the

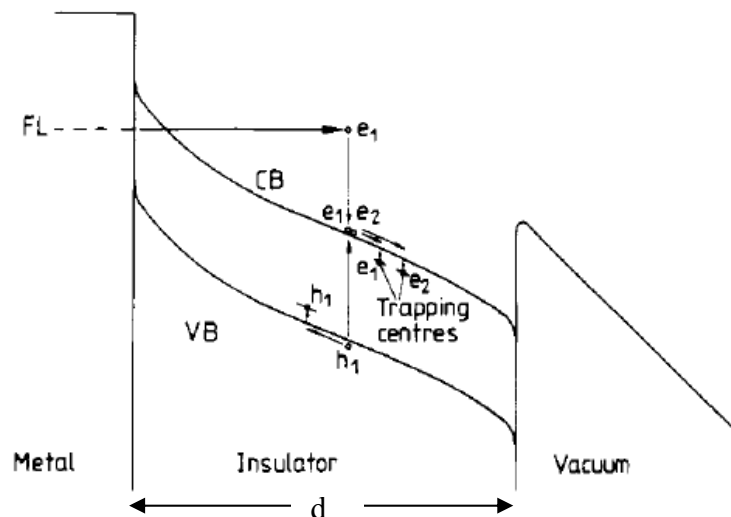


Fig.9: Initiating mechanism for switching on an emitting site by Athwal and Latham [18]

second interface (see Fig.9). Emission therefore follows the Richardson-Dushman law of thermionic emission:

$$J = C \cdot T_e^2 \exp\left(-\frac{\chi}{k_b T_e}\right) \quad \dots (12)$$

where χ is the electron affinity of the insulator, T_e Temperature of the electrons and C is a constant. T_e was calculated by Latham [19] as:

$$T_e = \frac{2ed}{3k\varepsilon_r} \quad \dots (13)$$

by considering the potential drop of $V = E \cdot d / \varepsilon_r$ across the insulator of thickness d , with E as the macroscopic field and ε_r is the relative dielectric constant of the insulator. So according to MIV model

$$j \propto E^2 \exp\left(-\frac{3\chi\varepsilon_r}{2dE}\right) \quad \dots (14)$$

which has the form of the Fowler-Nordheim equation.

2.2.4. Metal – Insulator – Metal (MIM) model

MIM model explains the FE process occurring at the metal-insulator-metal system illustrated in Fig.10. It was initially proposed to explain how a carbon graphite particle artificially deposited on a Cu electrode could promote low field (< 10 MV/m) ‘cold’ electron emission [20]. In this case it was proposed that the flake like structure of graphite particle would form a MIM microstructure with the substrate electrode and its ambient oxide layer. It has also been found that such MIM structures are the predominant electron emission sources on heat-treated broad area niobium electrodes. [13]

The basic emission mechanism of emission in this case is the same as with the MIV model. In addition to this, it was assumed that the superficial metallic particle or flake sits on top of the point of contact. However, because the flake is not grounded it ‘probes’ the electric field nearby and adopts the potential close to the equipotential at the flake's highest point. [21] The potential at this point is thereby ‘transmitted’ to the particle-insulator interface. If the flake height is h and the insulator thickness is d then the externally applied field is enhanced by a factor on the order of h/d in the insulator region, and thereby resulting into an enhanced field across its contact point with insulator. Thus, in a switch-on process, a

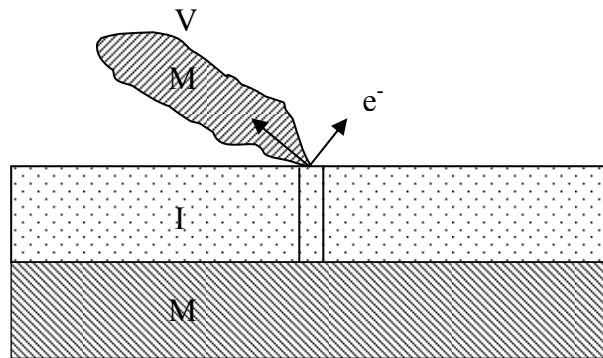


Fig.10: Schematic illustration for electron emission in a MIM system.

conducting channel is formed in this region. In the steady emission stage, electrons are assumed to be injected from the metallic substrate into the conduction channel, which are subsequently accelerated in the channel by the internal field to become the hot electrons. Thus, the emission occurs by the same mechanism as described in MIV model.

2.2.5. Adsorbate effects

Field emission requires a very clean vacuum to follow FN theory. Enhanced field emission from metals with the adsorbed atomic layer on its surface can be attributed to the changes in effective value of the work function. The effect of adsorbates and their diffusion on typical field emitter (sharp metallic needle) was studied in detail by R. Gomer [22] using FE microscopy (FEM), who observed the shape/shadow of adsorbed molecules on the emission pattern.

In-situ deposition of individual metal atoms on the tip has been shown to cause jumps in the emitted current. Todd and Rhodin [23] showed that they could distinguish one two and three tungsten-atoms and their subsequent desorption when the field remained on. Then they investigated the response of individual tungsten (hkl) faces to the adsorption of different alkali adatoms (Na, K, Cs), which all increase emission via lowering of work function.

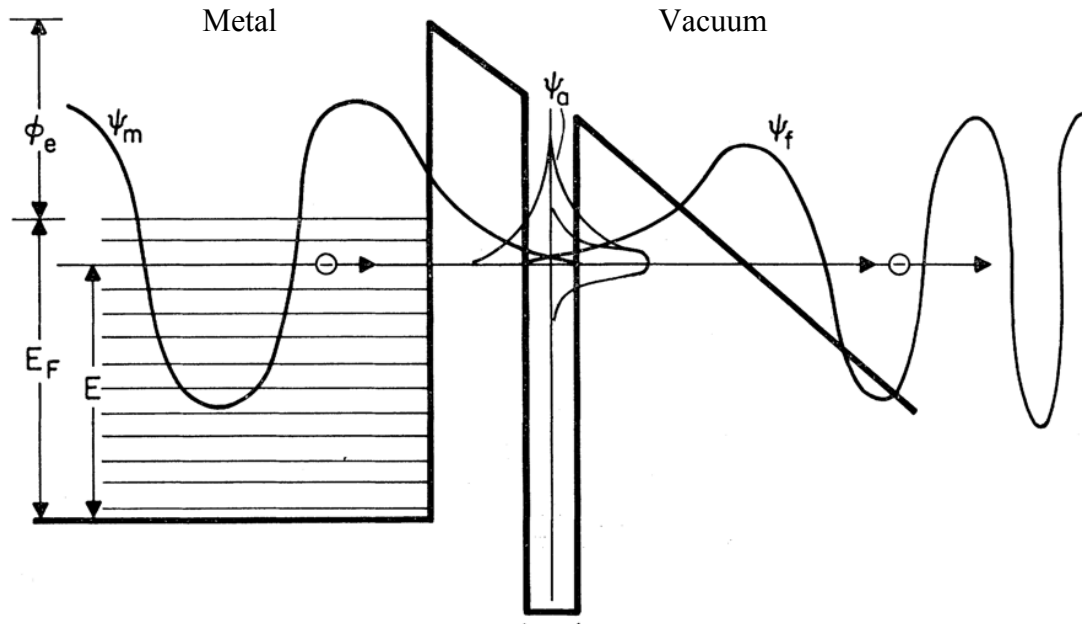


Fig.11: Band diagram used in the model of resonant tunnelling given by Gadjuk for a metal-vacuum interface with a local energy level due to the presence of an adsorbed atom. The electron wave functions are: ψ_m , the unperturbed metal function; ψ_a , the localized impurity function; and ψ_f , the emitted electron function. [25]

The enhanced field emission observed due to adsorbates could not be described satisfactorily only by considering the change in effective work function of the metal surface, and the theory of resonant tunneling was firstly pointed out by Duke and Alferieff [24] and later studied in detail by Gadjuk [25]. To account for enhanced emission from gas condensation, this model assumes that adsorbed atoms are responsible for creating localized energy levels near the metal surface as is schematically shown in Fig.11. This model was designed to reflect the atomistic nature of a single adsorbate atom or a monolayer of adsorbates. One dimensional calculations show that the tunneling process of electrons with energies close to the localized states can be resonantly enhanced.

If the adsorbate atom has an energy level at or near the Fermi level of the underlying metal, resonance effects can occur as electrons with that energy tunnel coherently from the metal into the adsorbate level and then out into the vacuum, thus increasing the emission probability. The effect can be clearly seen as a bump in the energy distribution of the emitted electrons [26, 27]. Its appearance in the total emission current can vary depending on the parameters of the resonant level and the range of fields employed. It can increase the emission current by a factor of 10^2 to 10^4 and lead to curvature at sufficiently high fields in a FN plot. In the other case, if the adsorbates have the bound states below the conduction band of the cathode metal, this can lead to a decrease in both the emission current and the slope of

the FN plot. Such result inconsistent with a simple change in work function in FN theory, and has been seen in point-to-plane configuration of FE measurements [28].

Halbritter [29] has suggested that adsorbed water with its strong dipole moment is crucial to enhanced electron field emission. To desorb such impurity atoms from the surface, baking of metallic surfaces in UHV conditions is the frequently used method for cavities. Water is certainly one of the main adsorbates on the cavity walls, especially if the cavity is not baked following assembly, as is customary. The one dimensional current calculations predict that tunneling is enhanced by up to a factor of 10^4 for adsorbates less than a single monolayer thick. Resonant tunneling of electrons due to adsorbates was accounted for unrealistically high and widely varying values of S [30]. Although this mechanism alone is still insufficient to turn a β value of 10 due to a geometric enhancement into a β value of 100, it may, in conjunction with other mechanisms, explain the observation that adsorbed gases enhance field emission [14, 31]. In the light of the present knowledge and level of understanding, it now is believed that field emission enhancement is due to a combination of geometric field enhancement and some other models, and therefore depends on foreign particulates as well as the interface or condensed gases.

2.3. Conditioning effects

The emission characteristics of a particular broad-area cathode are often seen to change during a series of measurements. These changes are frequently spontaneous and found uncontrollable. Such changes are generally said to result from "conditioning" processes; the converse is "deconditioning". Conditioning effects are important in the practical context of minimizing the emission current between a given pair of electrodes (and maximizing their breakdown voltage); they are also important in studying the emission processes themselves. [11]

2.3.1. Current conditioning

The initial emission from a fresh pair of electrodes is often unstable and uncontrollable. After a sufficient flow of charge or lapse of time under high voltage, however, it is frequently found that the current will stabilize itself. Alpert et al. [32] found initial current spikes which disappeared after 30 s, while Sayag et al. [33] observed that after cycling of the voltage below the breakdown field 3 or 4 times and then allowing a current of about 1 μA to pass for 1-2 h, instabilities were eliminated and almost reproducible I-V

characteristics could be rendered. Powell and Chatterton [34] made an extended study on tungsten, copper, aluminium and stainless steel electrodes, and found four different types of instabilities as discussed below.

(i) *Microdischarges* consist of short (ms) irregular selflimiting discharges or pulses, often thought to result from the transit of small particles of material from anode to cathode. According to Powell and Chatterton, they appear only above a particular (electrode-dependent) threshold voltage and are seen only with large electrode separations (> 1 mm). They occur independently of the magnitude of any steady FE currents that may be present, though conversely such steady currents are reported to be unaffected, increased, initiated, or decreased by the occurrence of microdischarges [11, 34-36]. SEM observation of cathode surfaces after microdischarges shows the presence of μm -sized pits [37] and projections [38] as given in Fig.12.

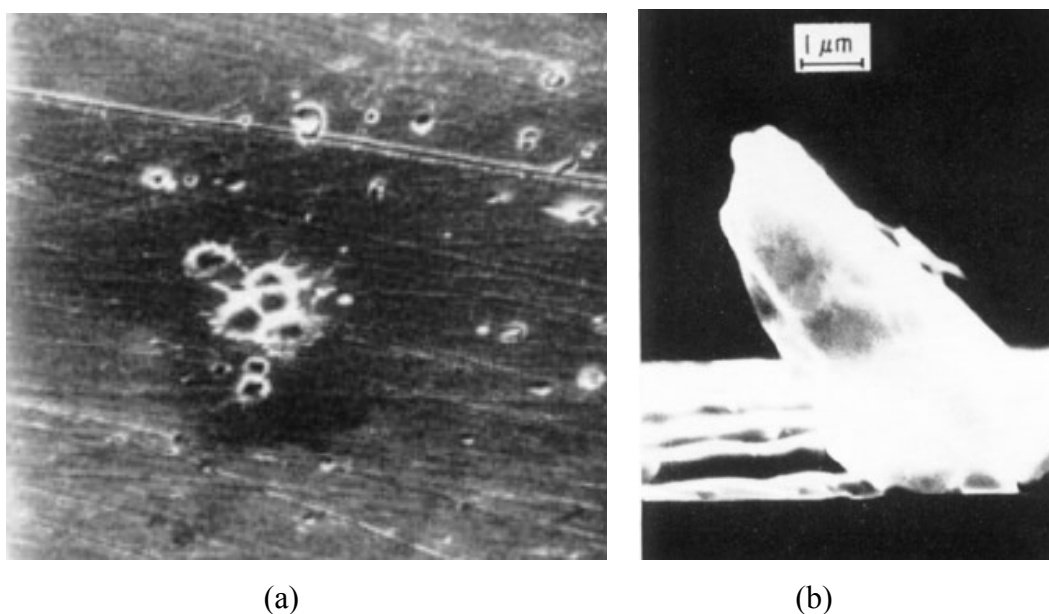


Fig.12: (a) Pits of μm size [37], and (b) projection [38] on a cathode surface, formed after microdischarges.

(ii) *Rectangular pulses* were observed by Powell and Chatterton as a sort of on-off increment, of duration between several hundred μs and several s, superposed on an otherwise steady emission current. They suggest that these pulses may result from the migration of small groups of adsorbed atoms across emission sites. Similar pulses are reported by others [39-41].

(iii) *Ignition*, as described by Powell and Chatterton, refers to an abrupt and reproducible jump in the steady emission current, typically by a factor of 10, as the voltage is

increased. The jump is reproduced in the opposite sense, at a slightly lower voltage, as the voltage is reduced. Similar phenomenon was observed in gaps of $d > 1$ mm, although the jump does not occur in the reverse sense as the voltage is reduced; a recovery period of about 10 min is necessary before the original ignition can be reproduced.

(iv) *Ageing* effects were seen by Powell and Chatterton following an increase of emission current into the milliamperage range. These consist of a suppression of the ignition effect and a reduction in the number and size of rectangular pulses, presumably as a result of local heating of emission sites, driving off whatever adsorbates are responsible for these phenomena. The rectangular pulses return about 20 min after the current is reduced to zero (in a pressure of 3×10^{-7} Torr), while the ignition jump is restored by a deliberate contamination of the vacuum or by the passage of several days.

2.3.2. Breakdown conditioning

Breakdown discharges ("sparks"), contrary to the microdischarges, are true discharges in which the current flow is limited only by the capability of the external power supply. They are believed to result from the vaporisation of small quantities of electrode material, resulting from various sources, e.g. from the impact of charged microparticles on an electrode surface after being accelerated across the gap, from the heating of a cathode emission site by the FE current flowing from it, or from the local heating of an anode by the FE current bombarding it. It has long been known that such breakdowns can be effective in conditioning a cathode, not only in removing the instabilities initially observed in the emitted current [42-44], but also in reducing the magnitude of the current for a given voltage.

Generally it is observed that emission which initially fits a FN relation continues after a discharge to follow a FN relation but with different S and different (generally lower) β . Williams and Williams [45] found that three breakdowns were sufficient to give straight-line FN plots for their stainless steel cathodes; 40 breakdowns reduced β from an initial 150 to an apparently asymptotic value of about 90. Similar conditioning effects are reported by Hackam and others [46].

The effect of breakdown discharges on a cathode surface can be seen directly by the scanning electron micrographs. Cox [47], and Cox and Williams [48] showed microphotographs of a cathode region before and after a discharge; in each case little damage is caused by the discharge, but a formerly emitting dust particle is found to be absent. More

intense discharges clearly alter the cathode surface and create potentially emitting projections [49-51], e.g. shown in Fig.13 for the case of a copper surface.

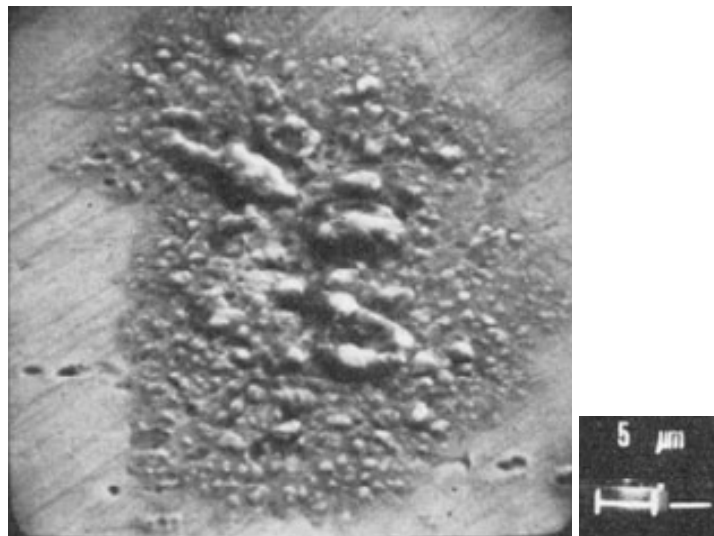


Fig.13: Typical micrographs of arc damage on copper surface. [50]

Hantzsche et al. [52] studied breakdown damage from very short voltage pulses. Cathodes conditioned with several thousand pulses, each of 5-10 ns duration, were found to be densely covered with many submicrometer sized ridges, craters, and potentially emitting protrusions; β 's of 20-30 were measured for the overall cathode surfaces. Such cathodes subsequently spark conditioned with shorter pulses (2-5 ns), however, showed much smoother surfaces and correspondingly gave β 's less than 3. Hantzsche et al. argue that the transition from smoothing to roughening effects occurs when the pulse length τ equals $\sim\tau_a$, the time for a localized molten surface region to move significantly under the discharge plasma forces.

2.3.3. Gas conditioning

Another method of changing the emission characteristics of a particular cathode surface is to draw current from it in the presence of a low-pressure gas. Thus Alpert et al. [53] subjected a cathode ($\beta=100$) to 10^{-4} Torr of argon; after several hours of operation at 100 μ A of emission current, the Ar was removed and a value below 20 was obtained. The effect was attributed to the selective sputtering of the projections assumed to be responsible for the emission. Bloomer and Cox [54], in a more extensive study, found that 10^{-4} to 10^{-3} Torr of Hg or Ar with tens of nanoamperes for 15min could reduce β 's initially ~ 100 by some 25 %, the

effect again being attributed to sputtering. Oxygen had a much more marked effect: 10^{-6} Torr with a starting current of 100nA brought about a roughly exponential decrease in current. These conditions being judged insufficient for significant sputtering, the conditioning effect was attributed to a work function increase of 1.7 eV for the Mo cathode due to chemisorbed oxygen. A similar effect was later seen with a Cu cathode [50].

2.3.4. Heat treatment

To the extent that the pulses and instabilities in emission current discussed earlier are caused by superficial, loosely bound impurities and adsorbates, one would expect that they could be reduced or eliminated by baking out the electrodes. Indeed, such thermal conditioning is routinely observed (more frequently in the heating which accompanies UHV bakeout). Williams and Williams [45] reported that a 300 °C anneal was sufficient to remove the discontinuities they had observed in the I-V characteristics of stainless steel electrodes, though curvature in their FN plots remained; Davies and Biondi [55] found that 850 °C was necessary to stabilize the currents from their Cu cathodes.

Ultra high vacuum heat treatments at 1400 °C for 30 min, followed by a fast cool down (< 200 °C after 5 min) suppressed the dc FE from niobium cathodes up to 100 MV/m, while annealing at moderate temperatures (200-800 °C) results in a strong activation of EFE [56, 57]. On high purity niobium cathodes showing no EFE up to 100 MV/m, strong activation of EFE was observed after UHV heat treatment at 400 °C from formerly non-emitting isolating particles sticking on the surface. [58] Ultra high vacuum heat treatments on niobium cavities have also been developed to deactivate emitters [59, 60]. It is believed that the interface between the emitting particles and the niobium surface plays an important role in governing field emission. Heat treatment is responsible for changing this interface layer.

2.3.5. Current conditioning and pressure effects on metallic nanowires

Highly improved current stability of nanostructures has been obtained by current conditioning, for example the effects on Si nanowires are shown in Fig.14. During conditioning, the adsorbates are partially removed from the emitters' surface or they are rearranged in a more stable energetic configuration and the current density decreases to a

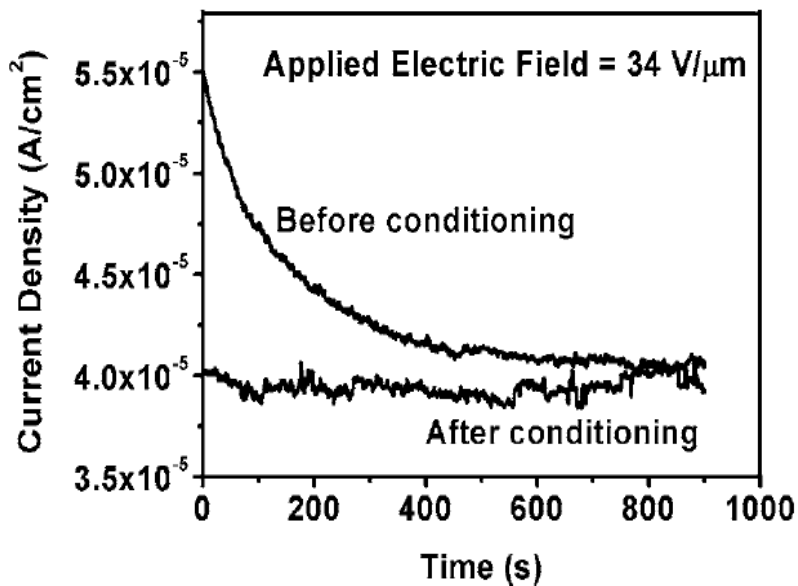


Fig.14: Current conditioning effects shown for Si NW: field emission current density as a function of time for an applied electric field of $34 \text{ V}/\mu\text{m}$ for preconditioning and after-conditioning processes. [61]

very stable level of $3.95 \times 10^{-5} \pm 1.1\% \text{ A}/\text{cm}^2$. Thus, the conditioning of the samples at higher current greatly increase the emission current stability. [61]

The stability improvements of Au nanowire cathodes has been confirmed by long term current processing in the pressure range between 10^{-4} and $5 \times 10^{-7} \text{ mbar}$ (Fig.15). [62] For the initial current of $55 \pm 5 \mu\text{A}$, it degraded continuously over 7 hours to values of 85%

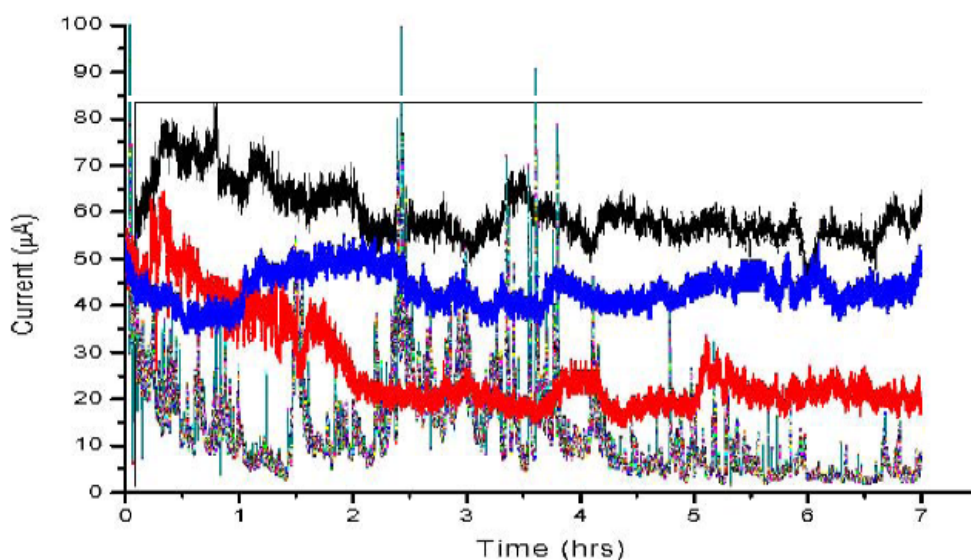


Fig.15: Long-term current stabilities of a 50 nm^2 Au-NW sample at various pressures/fields: $5 \cdot 10^{-7} \text{ mbar}/10.5 \text{ V}/\mu\text{m}$ (black curve); $1 \cdot 10^{-6} \text{ mbar}/11.3 \text{ V}/\mu\text{m}$ (blue curve); $1 \cdot 10^{-5} \text{ mbar}/12.5 \text{ V}/\mu\text{m}$ (red curve); $1 \cdot 10^{-4} \text{ mbar}/15 \text{ V}/\mu\text{m}$ (green curve). [62]

for 10^{-6} mbar, 36% for 10^{-5} mbar and 8% for 10^{-4} mbar. Thus, the ambient pressure of the cathodes is a key factor deciding their FE performance. The emission current remains at 93% level of the initial for $5 \cdot 10^{-7}$ mbar, demonstrating excellent current stability of $60 \pm 5 \mu\text{A}$ for several hours.

Metallic nanowires have the most attractive application as cold cathode in field emission displays, which are one class of display that aims to replace the ubiquitous cathode ray tube (CRT). For this purpose, the cold cathode must be capable of emitting electrons at low macroscopic electric fields (typically in the range 1-20 V/ μm) with sufficient current density (typically in the range 10-100 mA cm^{-2}) to generate bright fluorescence from the associated phosphor on the anode. To be usefully incorporated in a FED, it must be deposited with relative ease, accuracy, and uniformity over the entire active area of the display and be a vacuum compatible material.

2.4. Avoiding enhanced FE from metallic surfaces

Micro-particles with or without impurity inclusions, surface irregularities and hydrocarbons have been identified as major sources of enhanced FE (EFE) by several investigations on metallic (niobium) samples and superconducting cavities. Most field emitters are conducting particles of irregular shape with a typical size of 0.5-20 μm , and found to contain foreign elements such as iron, chromium, nickel, copper, and carbon. One example of such an emitting particle is shown in Fig.5 (a). Investigations with dc field emission scanning microscopes (FESM) have shown that all the particles do not emit, only 5-10 % are observed as field emitters.

Of paramount importance is cleanliness during the surface preparation stage. The use of high purity solvents/water and working in clean rooms is well accepted for this purpose. Several micrometers of surface material have to be removed to get rid off the damage layer caused by mechanical stress and any embedded impurities. For Nb surfaces, this is done either by electropolishing (EP) and/or buffered chemical polishing (BCP) methods. It was concluded from the investigations that for good performances of cavities a damaged layer of $> 50 \mu\text{m}$ had to be removed by BCP or EP. These results were “confirmed” by a series of cavity tests, in which material was successively removed and the cavity performance (peak electric fields E_{peak}) was recorded; see Fig.16 [63].

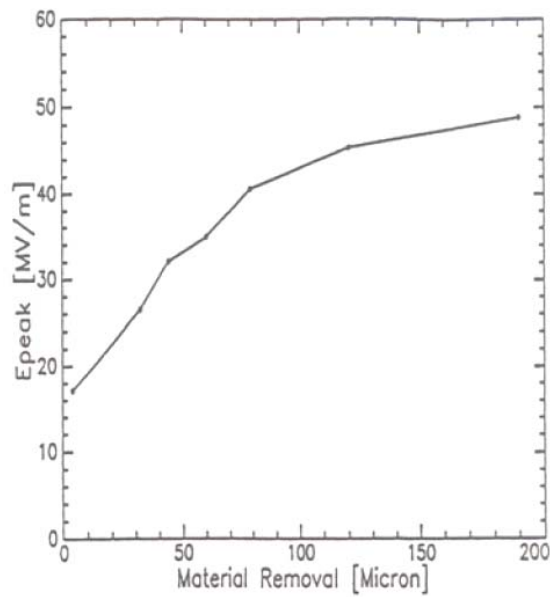


Fig.16: Effect of removal of surface damage layer on the performance of a single cell niobium cavity [63]

Improved cleaning techniques, such as high pressure ultra pure water rinsing (HPR) [64, 65] have resulted significant suppression of EFE from cavities by removing contaminants on the surface. Dry-ice cleaning (DIC) [66] has shown up interesting initial results on niobium cavities and samples. [67, 68] Detailed and systematic investigations on the efficiency of DIC for suppressing EFE from niobium and copper surfaces has been performed by us and will be discussed later in this thesis.

References

- [1] <http://tesla-new.desy.de>
- [2] G. Fursey, *Field emission in vacuum microelectronics*, (Kluwer Academic/ Plenum Publishers, New York, 2005).
- [3] E. L. Murphy and R. H. Good, *Physical Review* 102 (6), 1464 (1956).
- [4] R. V. Latham, *High Voltage Vacuum Insulation: Basic concepts and technological practice* (Academic Press, London, 1995).
- [5] H. A. Schwettman, J. P. Turneaure, and R. F. Waites, *Journal of Applied Physics* 45, 914 (1974).
- [6] N. Pupeter, A. G'ohl, T. Habermann, A. Kirschner, E. Mahner, G. Müller, and H. Piel, *Proceedings of the 7th Workshop on RF Superconductivity*, pp. 67, Gif-sur-Yvette, France, 1995.
- [7] D. Alpert, D. A. Lee, E. M. Lyman, and H. E. Tomaschke: *J. Vac. Sci. Technol.* 1, 35 (1964).
- [8] G. Vibrans : MIT Lincoln Lab. Report 353 (1964).
- [9] M. Jimenez, R. J. Noer, G. Jouve, J. Jodet, and B. Bonin. *Journal of Physics D* 27, 1038 (1994).
- [10] D. Alpert, D. A. Lee, E. M. Lyman, and H. E. Tomaschke. *J. Vac. Sci. Technol.* 1, 35 (1964).
- [11] R. J. Noer. *Applied Physics A* 28, 1 (1982).
- [12] Ph. Niedermann, PhD thesis, University of Geneva, 1986. Dissertation number 2197.
- [13] E. Mahner. *Proceedings of the 6th Workshop on RF Superconductivity*, Newport News, pp. 252, (1993).
- [14] Q. S. Shu, K. Gendreau, W. Hartung, J. Kirchgessner, D. Moffat, R. Noer, H. Padamsee, D. L. Rubin, and J. Sears. *IEEE Transactions on Magnetics: Proceedings of the 14th Applied Superconductivity Conference MAG-25*, 1868 (1989).
- [15] O. Gröning, O. M. Küttel. C. Emmengger, P. Gröning, and L. Schlapbach, *J. Vac. Sci. Techn. B* 18, 665 (2000).
- [16] L. Nilsson, O. Groening, C. Emmenegger, O. Kuettel, E. Schaller, L. Schlapbach, H. Kind, J. M. Bonard, and K. Kern, *Appl. Phys. Lett.* 76, 2071 (2000).
- [17] J. M. Bonard, N. Weiss, H. Kind, T. Stockli, L. Forro, K. Kern, and A. Chatelain, *Adv. Mater.* 13, 184 (2001).
- [18] C. S. Athwal and R V Latham *J. Phys. D: Appl. Phys.*,17 1029 (1984).
- [19] R. V. Latham, *Vacuum*, 32, 137 (1982).

-
- [20] C. S. Athwal, K. H. Bayliss, R. Calder, and R. V. Latham, *IEEE Trans. Plasma Sci.* 13, 226 (1985).
- [21] N. S. Xu. *High Voltage Vacuum Insulation*, edited by R. V.Latham, pp. 115 (Academic Press, London, 1995).
- [22] R. Gomer , *Rep. Prog Phys.* 53, 917, (1990).
- [23] Todd and Rhodin, *Surface Sci.* 42, 109 (1974).
- [24] C. B. Duke, and M. E. Alferieff, *J. Chem. Phys.* 46, 923 (1967).
- [25] J. W. Gadzuk, *Phys. Rev. B* 1, 2110 (1970).
- [26] E. W.Plummer, and R.D.Young, *Phys. Rev. B*1, 2088-2109 (1970).
- [27] L. W.Swanson, and L.C.Crouser, *Surf. Sci.* 23, 1-29 (1970).
- [28] G. Ehrlich, and F.G.Hudda, *J. Chem. Phys.* 35, 1421-1439 (1961).
- [29] J. Halbritter. *IEEE Transactions on Electrical Insulation* EI-18(3), 253 (1983).
- [30] T. Habermann, *Dissertation, university of Wuppertal*, 1999, WUB-DIS-98-18.
- [31] J. Knobloch, *Dissertation, Cornell university*, 1997, CLNS THESIS 97-3.
- [32] D. Alpert, D. A. Lee, E. M. Lyman, and H. E. Tomaschke: *J. Vac. Sci. Technol.* 1, 35-50 (1964).
- [33] G. J. Sayag, N. T. Viet, H. Bergeret, and A. Septier: *J. Phys.* E10, 176-179 (1977).
- [34] H. P. S. Powell, and P. A. Chatterton, *Vacuum* 20, 419 (1971).
- [35] I. Brodie, *J. Appl. Phys.* 35, 2324 (1964).
- [36] J. J. Maley, *J. Vac. Sci. Technol.* 8, 697 (1971).
- [37] R. V. Latham, E. Braun, *J. Phys.* D3, 1663 (1970).
- [38] P. I. Biradar, and P. A. Chatterton, *J. Phys.* D3, 1653 (1970).
- [39] G. P. Beukema, *J. Phys.* D7, 1740-1755 (1974).
- [40] R. N. Allan, and P.K.Bordoloi, *J. Phys.* D8, 2170 (1975).
- [41] H. E. Tomaschke, D. Alpert: *J. Vac. Sci. Technol.* 4, 192 (1967).
- [42] G. A. Farrall, *J. Appl. Phys.* 42, 2284 (1971).
- [43] G. P. Beukema, *J. Phys.* D7, 1740 (1974).
- [44] P. Kranjec, and L. Ruby, *J. Vac. Sci. Technot.* 4, 94 (1967).
- [45] D. W. Williams, and W. T. Williams, *J. Phys.* D7, 1173 (1974).
- [46] R. Hackam, *J. Appl. Phys.* 45, 114 (1974).
- [47] B. M. Cox, *J. Phys.* D8, 2065-2073 (1975).
- [48] B. M. Cox, and W. T. Williams, *J. Phys.* D 10, L5-9 (1977).
- [49] R. Hackam, *J. Appl. Phys.* 45, 114 (1974).
- [50] B. M. Cox, *J. Phys.* D 7, 143 (1974).

- [51] G. P. Beukema, *J. Phys. D* 7, 1740 (1974).
- [52] E. Hantzsche, B. Juttner, V. F. Pochkarov, W. Rohrbeck, and H. Wolff, *J. Phys. D* 9, 1771 (1976).
- [53] D. Alpert, D. Lee, E. M. Lyman, and H. E. Tomaschke, *J. Appl. Phys.* 38, 880 (1967).
- [54] R. N. Bloomer, and B. M. Cox, *Vacuum* 18, 379 (1968).
- [55] D. K. Davies, and M. A. Biondi, *J. Appl. Phys.* 37, 2969 (1966).
- [56] N. Sankarraman, Ph. Niedermann, R. J. Noer, and Ø. Fischer, *J. Phys.*, Vol. 47, C7-133, (1986).
- [57] E. Mahner, Proc. 6th Workshop on RF Superconductivity, Newport News, USA, Oct (1993).
- [58] N. Pupeter, E. Mahner, A. Matheisen, G. Müller, H. Piel, and D. Proch, EPAC (1994).
- [59] H. Padamsee, K. Gendreau, W. Hartung, J. Kirchgessner, D. Moffat, R. Noer, D. L. Rubin, J. Sears, and Q. S. Shu., *Linear Accelerator Conference Proceedings*, Newport News, VA, (1988).
- [60] H. Padamsee, P. Barnes, J. Kirchgessner, D. Moffat, D. Rubin, J. Sears, and Q. S. Shu, *Proceedings of the IEEE Particle Accelerator Conference*, pp. 2420, San Francisco, CA, (1991).
- [61] R. Riccitellia, A. Carlo, A. Fiori, S. Orlanducci, M. L. Terranova, A. Santoni, R. Fantoni, and A. Rufoloni, *J. Appl. Phys.* 102, 054906 (2007).
- [62] C. S. Pandey, external report, Bergische Universität Wuppertal, UW-R2-07, 2007.
- [63] E. Mahner et al., Proc. 6th workshop on RF superconductivity, Newport News, Virginia, p.1085 (1993).
- [64] P. Kneisel, B. Lewis, and L. Turlington. *Proceedings of the 6th Workshop on RF Superconductivity*, Newport News, Virginia, (1993).
- [65] D. Reschke, 12th International Workshop on RF Superconductivity, Cornell, USA, (2005).
- [66] R. Sherman and W. Whitlock, *J. Vac. Sci. Technol. B* 8, 563 (1990).
- [67] D. Proch, D. Reschke, B. Guenther, G. Müller, and D. Werner, Proc. of 10th Workshop on RF Superconductivity, Tsukuba, p. 463 (2001).
- [68] D. Reschke, A. Brinkmann, D. Werner, and G. Müller, Proc. of the LINAC 2004, Lübeck, Germany (2004).

Chapter 3

DC field emission scanning measurements on electropolished niobium samples

A. Dangwal, D. Reschke, G. Müller

Physica C 441 (2006) 83–88

Abstract

Electropolished (EP) Nb samples were investigated by a dc field emission scanning microscope, which has recently been modernized for the fast scans on large samples. Measurements on EP samples before and after high pressure rinsing (HPR) are compared. Reproducible voltage scans at various surface fields have been obtained partially down to 1 nm resolution. The statistical overview of the density of emitting sites at 120 MV/m shows a reduction from about 30 before to 14 emitters/cm² after HPR. Local measurements of selected emitters prove increased onset fields E_{on} at 1 nA and decreased values after HPR. High resolution SEM images and EDX measurements of the identified emitters will also be presented.

Keywords: Field emission; Scanning microscope; Electropolishing; Niobium; High pressure rinsing

3.1. Introduction

Enhanced field emission (EFE) from particulates and surface irregularities is one major obstacle which has to be overcome for efficient high gradient operation of superconducting niobium cavities. Accelerating gradients up to 30 (40) MV/m, corresponding to peak electric surface fields of about 60 (80) MV/m at the cavity irises, are envisaged for accelerators like the X-ray free electron laser (XFEL) approved at DESY [1] and the international linear collider (ILC) under design now [2], respectively.

In order to avoid EFE in these cavities reliably, typical field emitters on Nb surfaces resulting from the actual surface preparation techniques must be identified. Since electropolished (EP) Nb surfaces are considered to improve the achievable cavity fields, we have started to investigate large area EP Nb samples by means of the dc field emission scanning microscope (FESM) [3]. This apparatus has recently been modernized with new hardware components (Keithley picoammeter with 1 kHz rate, FUG power supply with PID regulation) [4] and LabVIEW based programs, resulting in fast voltage scans of large samples thus improving the statistics of the FESM measurements. First results of voltage scans up to 120 MV/m with a successive change of resolution by anode tip diameters ranging from 300 μm to 2 μm and local measurements are presented. The density of emitting sites, onset field E_{on} at 1 nA and values of localized emitters will be compared on a EP Nb sample before and after high pressure rinsing (HPR). High resolution SEM images and EDX analysis of selected emitting sites will also be presented.

3.2. Experimental

Two Nb samples of 28 mm diameter previously tested after buffered chemical polishing [5] were electropolished (140 μm) and clean water rinsed at CEA Saclay. Contamination of these samples was avoided by clean room assembly and a special transport system which has been opened inside the load lock of the field emission scanning microscope at 10^{-6} mbar. For comparison, one sample (SEP2) was cleaned in a new HPR facility at DESY with similar parameters as used for cavities, i.e. at a pump pressure of 150 bar, a rotation speed of 4–5 rpm and a vertical speed of 10 mm/min. FE measurements were performed under ultra high vacuum conditions ($<10^{-9}$ mbar). The sample stage is movable in xyz directions by computer controlled motors with about 70 nm step width or by piezo translators with nm resolution. The electrode spacing, d , is controlled by a long distance

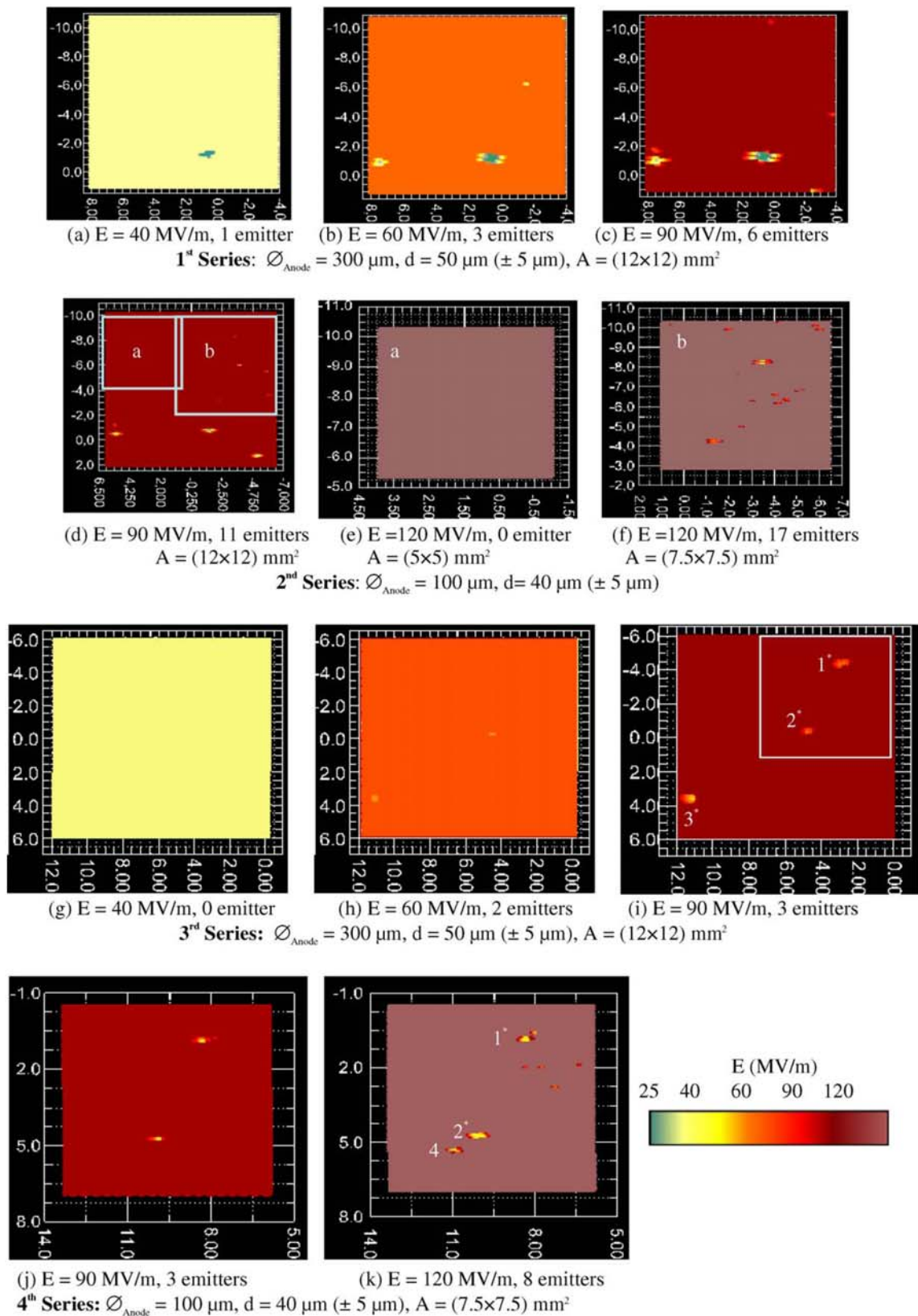


Fig. 1: Voltage maps of the same EP Nb sample before (a–f) and after HPR (g–k) taken at different field levels and showing the onset field of emitters (see color bar). The maps in (e, f, j, k) correspond to the marked areas in (d, i) respectively (For interpretation of the references in colour in this figure legend, the reader is referred to the web version of this article).

optical microscope with CCD video camera and varies less than 1 μm for well-tilted flat samples [3].

$\varnothing_{\text{Anode}}$ (μm)	E (MV/m)	N ($\#/\text{cm}^2$)	
		EP only	EP + HPR
300	40	0.7	0
300	60	2.1	1.4
300	90	4.2	2.1
100	90	7.6	5.3
100	120	30.2	14.2

Table 1: Number density of emitters for various anode diameters and electric fields extracted from Fig. 1.

Emitter distributions were obtained by the voltage scans, $V(x,y)$, with a constant PID-regulated current of 1 nA, the spatial resolution of which is limited by the selected W anode and electrode spacing. Five different anodes (tip diameters $\varnothing_{\text{Anode}} = 2\text{--}300 \mu\text{m}$) were used for the complete series of measurements. The resulting typical measurement time for one map of 100 x 100 pixels is about 1 h. At pronounced emitting sites, appropriate subroutines provide $V(z)$ plots at constant current (1 nA) for distance and field calibration and $I\text{--}V$ curves for Fowler–Nordheim (FN) analysis. Finally in situ SEM images with moderate spatial resolution ($\sim 1 \mu\text{m}$) are taken as a guide for the relocalization of emitters in the high resolution SEM (nm) with EDX analysis. A more detailed description of the measurement techniques is given elsewhere [4].

3.3. Results and Discussion

At first both EP Nb samples were investigated in the FESM by regulated voltage scans up to 120 MV/m. Sample SEP1 showed the onset of FE at 60 MV/m and about 11 emitters/ cm^2 at 90 MV/m, which were clustered in a small part of the sample (0.25 cm^2), while for most of the surface no FE occurred up to 120 MV/m. The emitter distributions measured for sample SEP2 before and after HPR are shown in Fig. 1. It should be noted that the low resolution scan series (1st series before and 3rd series after HPR) were made in the same surface area of the sample, while the zoomed-in area of the 2nd and 4th series were slightly different according to the location of emitters.

In general, most of the emitters in Fig. 1(a–f) and (g–k) are reproducible for increasing field level as well as for zooming into higher resolution, but some emitters become

activated or better resolved then. As expected, sample SEP2 provides similar FE performance in terms of onset field and number density of emitters

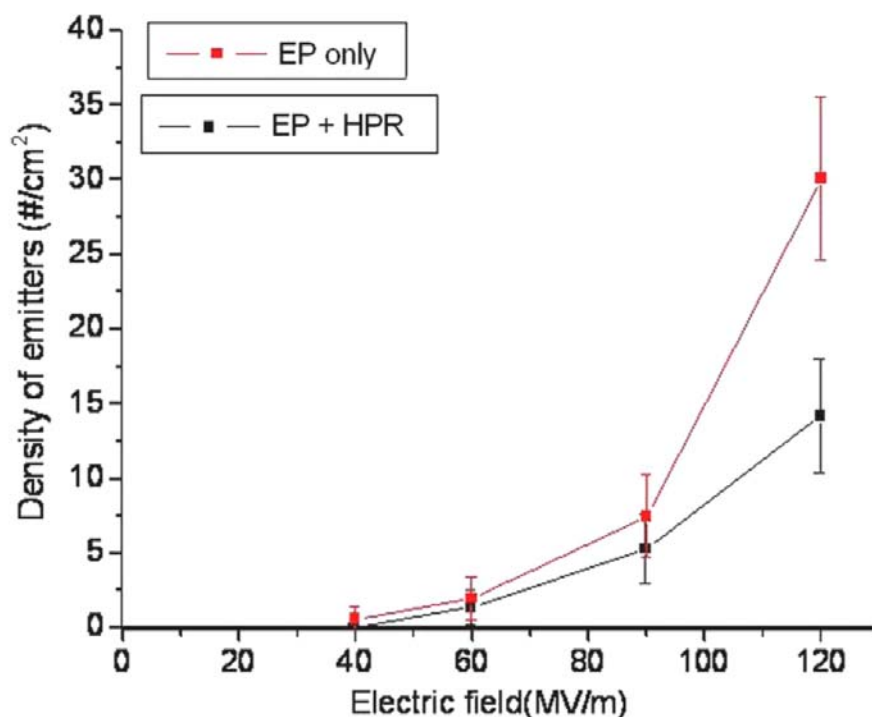


Fig. 2: Reduction of FE for SEP2 by HPR.

as sample SEP1 before HPR but improved values after HPR. Comparing Fig. 1(d) and (i) in detail, most of the emitters at 90 MV/m have been removed by HPR. In Fig. 1(f) and (k) at 120 MV/m, however, many weak emitters occur before as well as after HPR. The number density of emitters N resulting from the maps for different resolution and electric field E is given in Table 1. The comparison of these $N(E)$ data in Fig. 2 clearly proves the benefit of HPR against FE.

In order to learn more about the nature of the emitters, high resolution voltage scans were performed in the most interesting area (Fig. 1(f)) of sample SEP2 before HPR. In high resolution scans, the effective electric field between the electrodes in tip-plane configuration is $V/(\alpha \cdot d)$, where α is a geometric correction factor which depends on the tip geometry and electrode spacing [6]. Fig. 3(a) shows more emitters than the corresponding area in Fig. 1(d), thus demonstrating the activation of emitters by high fields. The strongest emission site there splits into three FE sites for 10 μm resolution (Fig. 3(b)), which are further resolved in (Fig. 3(c)), where the resolution limit set by the actual surface roughness is reached.

Some of the emitters localized in Figs. 3(b) and 1(k) were chosen for stability and FN analysis as shown in Fig. 4. With exemption of the rather unstable emitter #1(a), all emitters

clearly showed stable metallic FN behaviour partially with slight activation (e.g. #1(b) and #3*) or deactivation (e.g. #1*) effects which are well known as switch-on/off due to unstable microstructures and surface influences [7]. Obviously the emitters on this EP Nb sample were stronger before than after HPR, i.e. the onset fields E_{on} (1 nA) changed from 33–46 MV/m to 48–77 MV/m. The field enhancement factors β resulting from the slopes (for a work function Φ of 4 eV) vary less systematically between 31 and 231 and are balanced by the values of effective emission area, S , lying in the range of 10^{-20} and 10^{-12} m². These values are typical for EFE of Nb surfaces and can be explained by the projection model of irregular shaped particulates of μ m size [8] and resonant tunneling through electronic surface states [6].

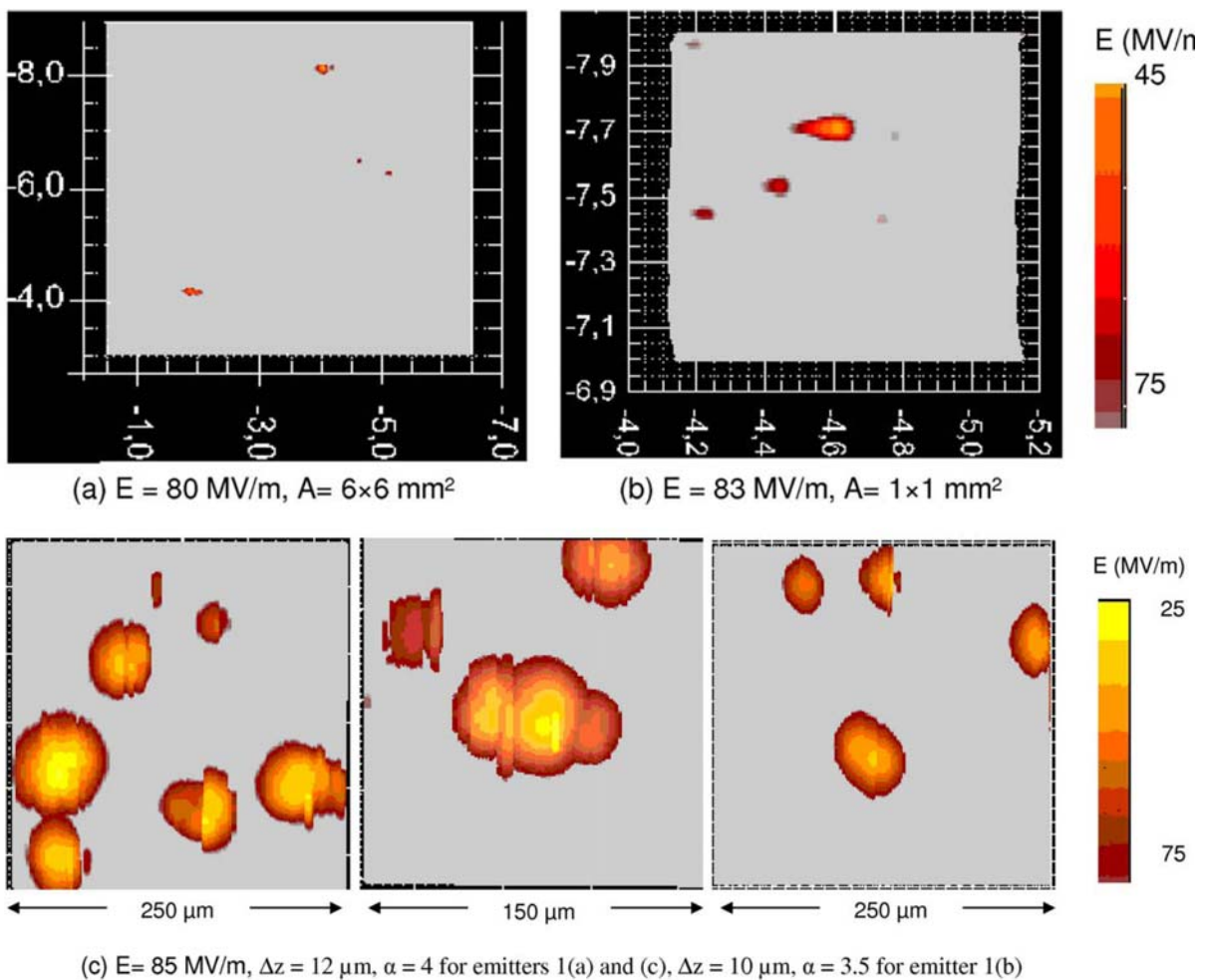


Fig. 3: Zooming into emitters of sample SEP2 before HPR by high resolution maps with reduced anode diameter of (a) 30 μ m, marked square resolved in (b) 10 μ m and emitters #1 (a–c) resolved in (c) 2 μ m.

It should be noted that only one emitter on SEP2 (#2) has survived the HPR cleaning process but weakened as shown in Fig. 5(a–b). Initially, this emitter on the EP Nb sample

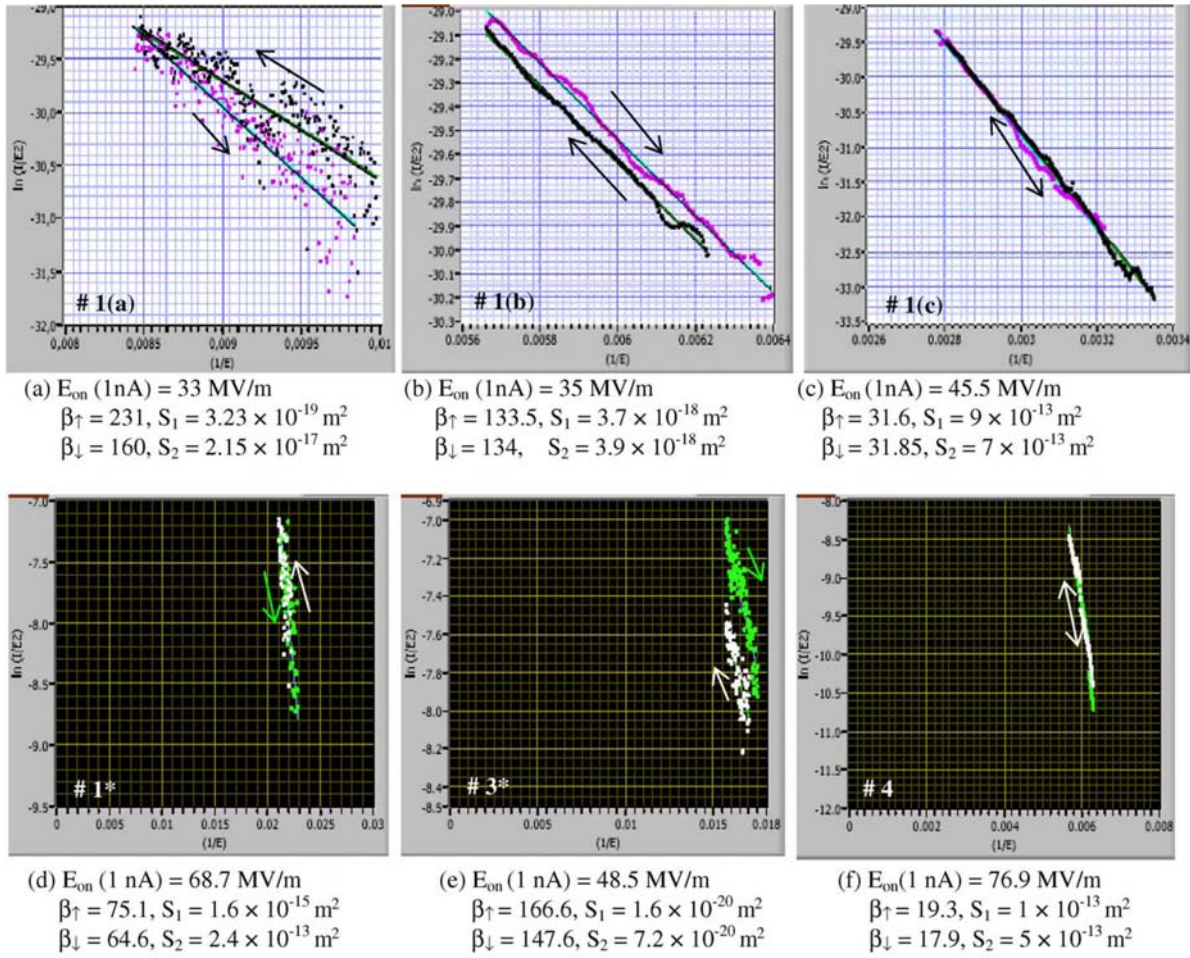


Fig. 4: FN curves of single emitters #1(a), 1(b) and 1(c) as marked in Fig. 3(b) and # 1, 3 and 4 as marked in Fig. 1(k). E_{on} is the onset field measured at 1 nA. β_{\uparrow} , β_{\downarrow} and S_1 , S_2 represent the extracted β values and S parameters from FN curves in up and down modes of changing electric field respectively.

with an E_{on} (1 nA) of 45 MV/m switches from a low β /high S into a high β /low S state, the latter being much less emissive at fields around 50 MV/m (Fig.5(a)). After HPR this emitter (#2*) shows more stable emission in the field range 54–75 MV/m with as low β values as in the initial state but S parameters comparable to the final state before HPR. This puzzle might be clarified by the high resolution SEM images of this emitter in Fig. 5(c–e). Obviously a thin object of about $100 \mu\text{m}^2$ size with a folded edge extension and sharp protrusions covers the Nb surface, which seems to be conductive according to the dark colour in SEM. Most of this object is semi-transparent for the electron beam, and the grain structure is hardly influenced. At higher magnification submicron protrusions and a rolled edge of the extension become evident. Since no foreign element ($Z > 10$) was detected by EDX analysis, this object might reflect a different Nb oxide state compared to the regular surface as observed in star bursts

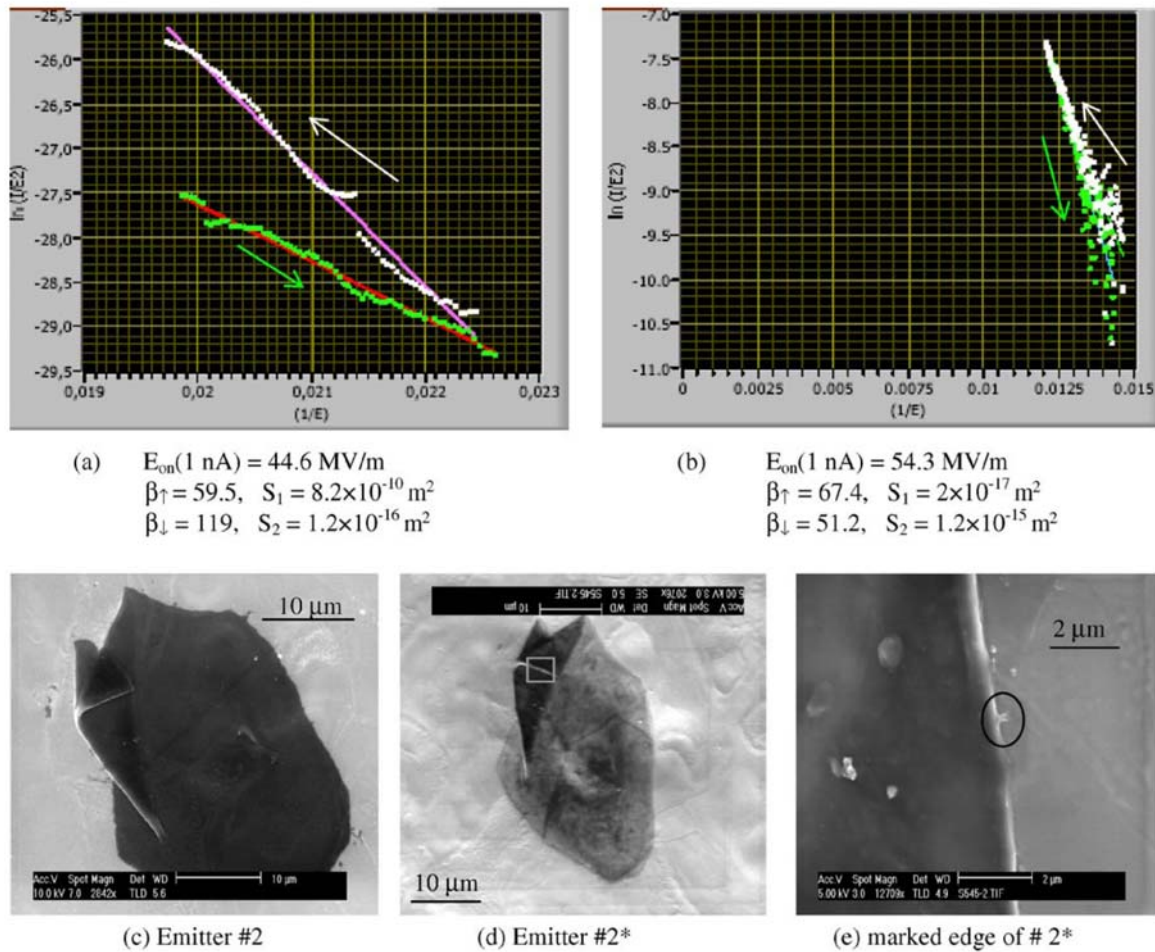


Fig. 5: FN curves and HRSEM images of the same emitter before (#2) and after HPR (#2*). Abbreviations are same as used in Fig. 4.

[9]. It is tempting to attribute the change of FE parameters to the alignment of protrusions with electric field and dulling of sharp edges by HPR, but further FESM investigations with submicron resolution are required to prove any of such correlations.

Since HPR is regularly used for the surface preparation of Nb cavities, we have tried

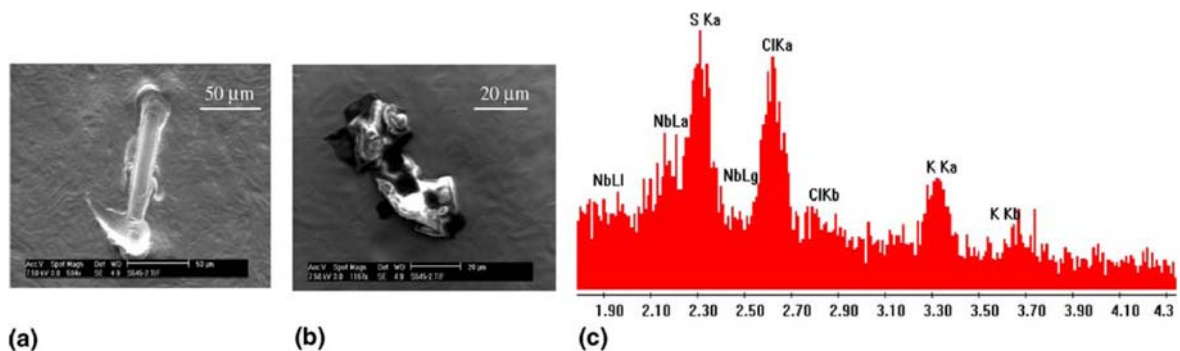


Fig. 6: SEM images of emitter #3* (a) and #4* (b). The EDX spectrum of #4* (c) shows S, Cl, K contents.

to identify all emitters found in Fig. 1(k) by SEM. While no obvious feature was found in the area of emitter #1*, pronounced objects appeared in the SEM images for emitters #3* and #4*. Fig. 6(a) shows a scratch-like surface irregularity of about 100 nm length with terraced edges probably caused by a massive tool, but EDX analysis revealed only Nb there. Therefore, strong but very local geometric field enhancement can be expected which fits to the high β and low S value of emitter #3*. In contrast Fig. 6(b) shows a crystalline particle of some 10 μm size with some edges, which fit well to the measured β and S values of emitter #4*. This particle partially consists of S, Cl and K as revealed by the EDX spectrum in Fig. 6(c). Considering the large size of all identified objects, the EFE of Nb should be reducible by improved surface preparation techniques.

3.4. Conclusions

Systematic FE scans of EP Nb samples have given onset fields of 40–60 MV/m and emitter number densities up to 30/cm² at 120 MV/m which were about halved after HPR. Since some of the emitters might have been welded on the surface by the FE current, further reduction is expected for EP samples directly cleaned by HPR. The strongest of these emitters were localized on a μm scale. Most of them showed stable FN-like I - V curves with values of 31–231 and S -parameters of 10^{-12} – 10^{-20} m² which are typical for particulates and surface irregularities on Nb. Some emitters were identified by high resolution SEM and EDX investigations. The only HPR resistant emitter turned out to be a thin conductive object with a folded edge and submicron protrusions, which mainly consists of Nb. Moreover, a scratch-like surface defect and a crystalline particle with S, Cl and K content were found as emitters after HPR. The rather large size and nature of these identified objects gives hope to avoid FE in Nb cavities by improved surface preparation techniques up to the fields required for XFEL and ILC.

Acknowledgements

We would like to acknowledge Claire Antoine and Alain Aspart from CEA Saclay for electropolishing of the samples and wish to thank the Electrical Engineering Department at the University of Wuppertal for providing SEM and EDX facilities. The support of the European Community Research Infrastructure Activity under FP6 “Structuring the European Research Area” program (CARE, contract number RII3-CT-2003-506395) is gratefully acknowledged.

References

- [1] R. Brinkmann, et al. (Eds.), TESLA XFEL Technical Design Report Supplement, DESY 2002-167, 2002; K. Floettmann, in: Proc. of 12th International Workshop on RF-Superconductivity, Cornell Univ., USA, 2005.
- [2] I.V. Bazarov, H. Padamsee, TESLA Report 2005-09, in: Proc. of 12th International Workshop on RF-Superconductivity, Cornell Univ., USA, 2005.
- [3] E. Mahner, N. Minatti, H. Piel, N. Pupter, Appl. Surf. Sci. 67 (1993) 23.
- [4] D. Lysenkov, G. Müller, Int. J. Nanotechnol. 2 (2005) 239.
- [5] D. Reschke, A. Brinkmann, D. Werner, G. Müller, in: Proc. Lin. Acc. Conf., Lübeck 2004.
- [6] T. Habermann, Thesis, University of Wuppertal, WUB-DIS 98-18 (1999).
- [7] T. Habermann, A. Göhl, D. Nau, G. Müller, H. Piel, M. Wedel, Part. Acc. 61 (1998) 137.
- [8] M. Jimenez, R.J. Noer, G. Gouve, J. Jodet, B. Bonin, J. Phys. D: Appl. Phys. 27 (1994) 1038.
- [9] J. Knobloch, H. Padamsee, Part. Acc. 61 (1998) 169.

Chapter 4

Effective removal of field emitting sites from metallic surfaces by dry ice cleaning

Arti Dangwal, Günter Müller, Detlef Reschke, Klaus Floettmann, and Xenia Singer

Journal of Applied Physics 102, 044903 (2007)

Abstract

Systematic results of the field emission properties of polycrystalline copper and niobium, and of single crystal Nb are reported. Dry ice cleaning is found to suppress enhanced field emission from metallic surfaces. The cleaning effect on the emitting sites was investigated by means of field emission scanning microscopy up to fields of 250 MV/m and high resolution scanning electron microscopy with energy dispersive X-ray analysis. The number density of emitters at given fields was drastically reduced by dry ice cleaning. Current-voltage measurements and derived Fowler-Nordheim parameters are partially discussed with respect to the morphology and impurity content of localized emitters. No emission from grain boundaries on large grain Nb samples was observed. The microscopy results prove the effective removal of field emitting particulates down to 400 nm as well as the partial smoothing of surface protrusions by DIC.

4.1. Introduction

Development of effective cleaning techniques for the removal of small particulates from metal surfaces is a primary need in high voltage vacuum devices.¹ Micron size surface irregularities can seriously affect the performance of high field accelerator cavities² by creating field emission (FE) sites,³ from where electrons are emitted at much lower electric fields than predicted by Fowler-Nordheim (FN) theory.⁴ This enhanced FE is mainly caused by particulates⁵ and surface protrusions⁶ due to local field enhancement. Such emitters originate as residues of chemical surface preparation and cleaning techniques or result from insufficient cleanroom conditions and mishandling of the surface.⁷⁻¹⁰

The removal of particulate emitters is rather difficult because these usually stick to the solid surface due to adhesion. The interaction between particulates and substrate includes van der Waals, electrostatic, and capillary forces.¹¹ All these adhesion forces F are found to be proportional to the particulate diameter d . Accordingly, a particulate of mass $m \sim d^3$ will require an acceleration $a = F / m \sim 1/d^2$, which becomes quadratically larger with decreasing size. Additionally, the number density of ambient particulates usually increases with decreasing size. Therefore, some small particulates usually remain on the surface after conventional cleaning techniques used in accelerator technology such as high pressure rinsing (HPR) with ultra pure water.¹²

Dry ice cleaning (DIC) is a powerful technique which uses a high pressure jet of pure carbon dioxide snow to loosen and remove different types of particulate contaminations from the surface by its unique combination of thermal, mechanical and chemical effects.¹³⁻¹⁶ The rapid cooling at the point of hitting brittles the particulates, thus weakening the adhesion for their efficient removal by the impact of snow particles. Unlike HPR, this technique significantly removes hydrocarbon contaminations from the cleaned surfaces,¹³ since carbon dioxide is a good solvent for non-polar chemicals. The possibility of a dry in-situ cleaning of the cavities, and already proven faster pump down rates with DIC,¹⁷ are surely advantageous for accelerator technology.

Nowadays copper and niobium sheet metals are used for the fabrication of cavities for accelerators. Dark currents caused by enhanced FE limit the accelerating field gradients in normal conducting rf guns¹⁸ and superconducting Nb cavities.¹⁹ Therefore, systematic investigations of the dc field emission properties of relevant metallic samples has proven to be helpful for the optimization of surface preparation techniques. In order to understand the origin of the emitters, field emission scanning microscopy (FESM)^{6, 20} combined with high

resolution secondary electron microscopy (SEM) and energy dispersive X-ray analysis (EDX) are required.¹⁰

Here we report on the effect of DIC on Cu and Nb surfaces by (i) comparing the number density of FE sites on particular sample areas scanned in FESM before and after DIC, (ii) determining the FE properties of localized emitters by current vs. voltage (I-V) measurements and FN analysis, and (iii) investigating their morphology and composition by SEM and EDX. This comprehensive study will prove that DIC reduces FE efficiently by removal of micron and submicron particulates as well as by smoothing of surface protrusions.

4.2. Experimental techniques

We have tested four copper (7 mm squares) and six niobium (28 mm diameter) samples, of which always two were fabricated with the same techniques for reproducibility checks. Two polycrystalline Cu samples were cut from a regularly turned cavity cell and the other two from a single-point diamond-turned cavity cell. Two polycrystalline Nb samples (PolyNb) were machined from high purity niobium with a residual resistance ratio RRR of about 300 and electropolished up to 140 μm using H_2SO_4 : HF in 9:1 volume ratio, resulting in a surface roughness of less than 0.5 μm . Two large-grain ($\sim \text{cm}$) and two single-crystal Nb samples (CryNb) of RRR ~ 340 were chemically etched by buffered chemical polishing (HF: HNO_3 : H_3PO_4 in volume ratio 1:1:2) to remove the damage layer up to 30 μm , resulting in a mirror-like surface with surface roughness of less than 0.1 μm . Finally all samples were extensively rinsed with ultra pure water and HPR in case of Nb. All the samples have been especially marked during fabrication to adjust the sample position in different experimental set-ups. For the sample transfer between the laboratories, an approved protection cap system²¹ was used and opened under cleanroom or high vacuum conditions only.

A modified DIC of the samples was performed in a class 10 cleanroom. Detailed description of the DIC experimental set-up and the cleaning procedure has been already described elsewhere.²²⁻²⁴ Carbon dioxide of purity grade 4.5 ($\text{N}_2 + \text{O}_2 < 45 \text{ vol.ppm.}$, $\text{H}_2\text{O} < 5 \text{ vol.ppm.}$, $\text{C}_n\text{H}_m < 1 \text{ vol.ppm.}$) and pure nitrogen (both particle filtered to $< 0,05 \mu\text{m}$) are supplied up to pressures of 50 and 12 bar, respectively. Fig.1 shows the high pressure DIC jet coming out of a dedicated nozzle system developed at Fraunhofer Institut

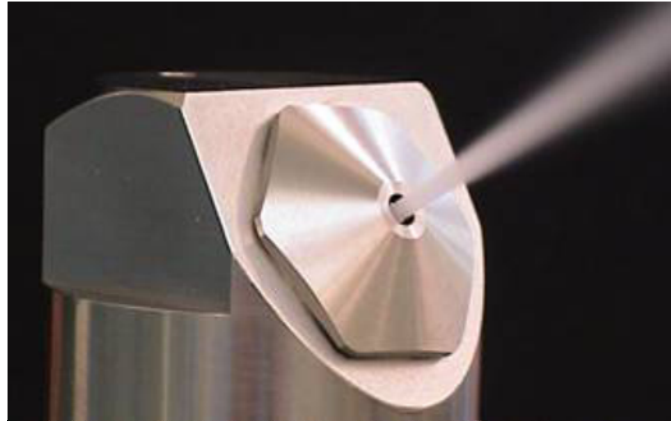


Fig. 1: High pressure dry ice jet emerging from DIC nozzle.

Produktionstechnik und Automatisierung (Stuttgart, Germany) for DESY for the cleaning of cavities. The CO₂ snow jet is surrounded by supersonic nitrogen²², which provides additional acceleration and focusing of the jet as well as a partial prevention of moisture condensation at the cleaned surface. The temperature of liquid CO₂ is maintained between -18°C to -10°C at the dedicated cooler/purifier unit¹⁶, which is connected to the nozzle by a pipe of 3 m length. This configuration keeps the fraction of snow in the jet in the order of 45%.²² An effective gas extraction system and a controlled heating system avoid recontamination and humidity condensation at the sample surface, respectively. The flat samples were cleaned by moving the DIC nozzle linearly back and forth with a constant speed. The cleaning duration of the large samples (28 mm diameter) was usually about 5 minutes, which includes the intermediate time for rotating the sample six times manually by 30°.

FESM measurements have been made in two steps: (i) scans over a selected sample area with a fixed anode at a maximum field given by a high applied voltage V regulated for a constant current I (2nA) within a few milliseconds, resulting in maps of the found emitters at correspondingly reduced field level; and (ii) local characterization of the interesting emitters observed in the scans. The scans were performed at the field levels varied as 60, 90, 120, 150, 200 and 250 MV/m for different samples by using a 5 kV power supply and adjusting the gaps between sample and anode down to 20 μm . For the scans conical anodes of diameter 300 μm or 100 μm were used depending on the area and required resolution. Local measurements were mostly performed with tip anodes of diameters 30, 10 or smaller down to 1 μm to resolve small emitting sites. Fig.2 shows a tip anode of apex radius 1 μm placed just above an emitting site on a large-grain Nb sample. The mirror-like sample surface is helpful



Fig. 2: Inner view of FESM, showing a mirror like Nb sample of 28 mm diameter below a tungsten tip anode ($\sim 1 \mu\text{m}$ apex radius).

to control the gap within an accuracy of $\pm 5 \mu\text{m}$ by observing the anode image with a long distance microscope and CCD video camera. The real electrode distance z is derived prior to any local I-V curve of an emitter by extrapolation of the measured $V(z)$ plot.²⁰ The local onset field for a current of 2 nA, $E_{\text{on}} = V/(z \cdot \alpha)$, has been corrected for the calculated tip shape factor α .

The relocalization of the emitters found with FESM in an ex-situ SEM has been ensured within an accuracy of $\pm 500 \mu\text{m}$ by using the marks on the samples. The high resolution SEM images and EDX measurements (for elements with $Z > 10$) were made by means of a Philips XL-30 with LaB_6 cathode.

4.3. Results and Discussion

4.3.1. Statistical reduction of FE by DIC

FE scans of two Cu samples (one of each type) performed with $100 \mu\text{m}$ conical anode over the area of $(5 \times 5) \text{mm}^2$ showed no emission at 60 MV/m before DIC. For the diamond-turned sample, 10 emitters have been found at 120 MV/m as shown in fig. 3(a), which reduced to 1 after DIC. This improved surface gives 6 emitters at 150 MV/m (fig.3(b)). The regularly turned Cu sample gave 8 emitters at 90 MV/m which improved after DIC to 0 (3) emitters at 90 (120) MV/m, i.e. very comparable results. Therefore the remaining Cu samples were directly dry ice cleaned. All four DIC Cu samples showed no FE up to 90 MV/m, and the best one up to 120 MV/m. No significant difference was found between the regularly and diamond-turned Cu samples.

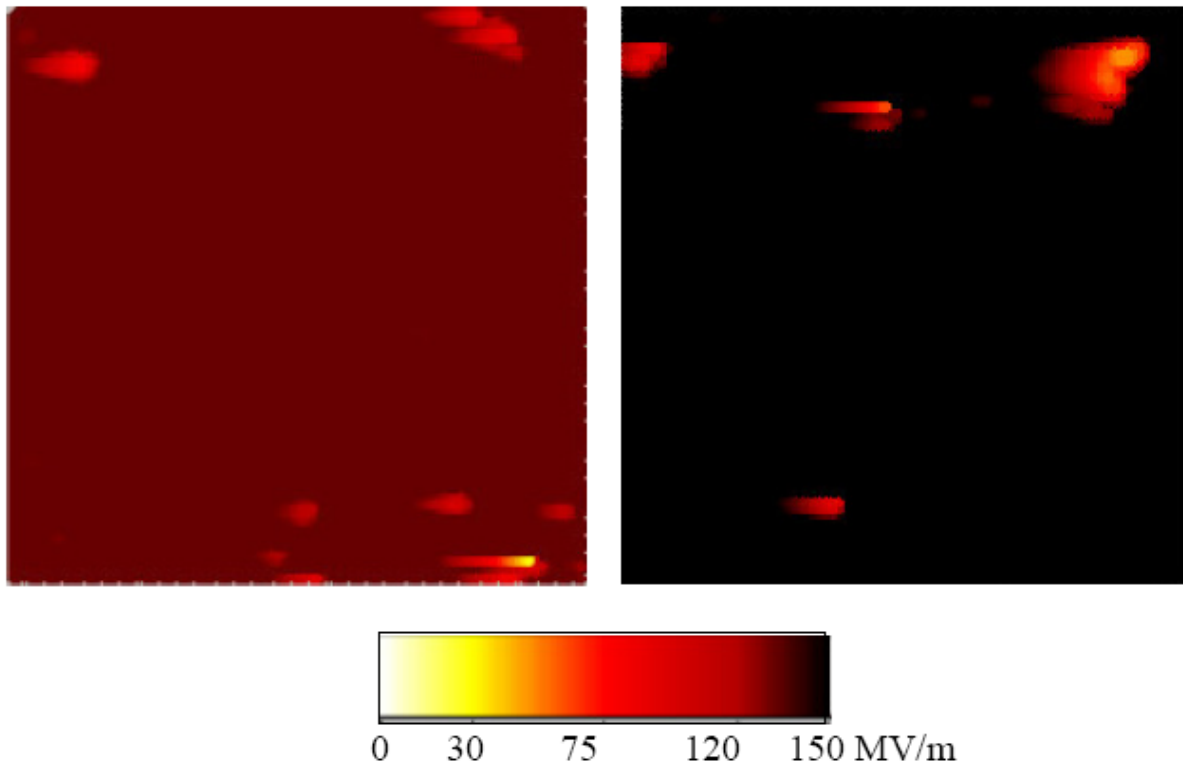


Fig. 3: FE-maps of Cu, performed with a conical anode ($100\mu\text{m}$) over the same (5×5) mm^2 area before (left) and after (right) DIC at 120 and 150 MV/m, respectively.

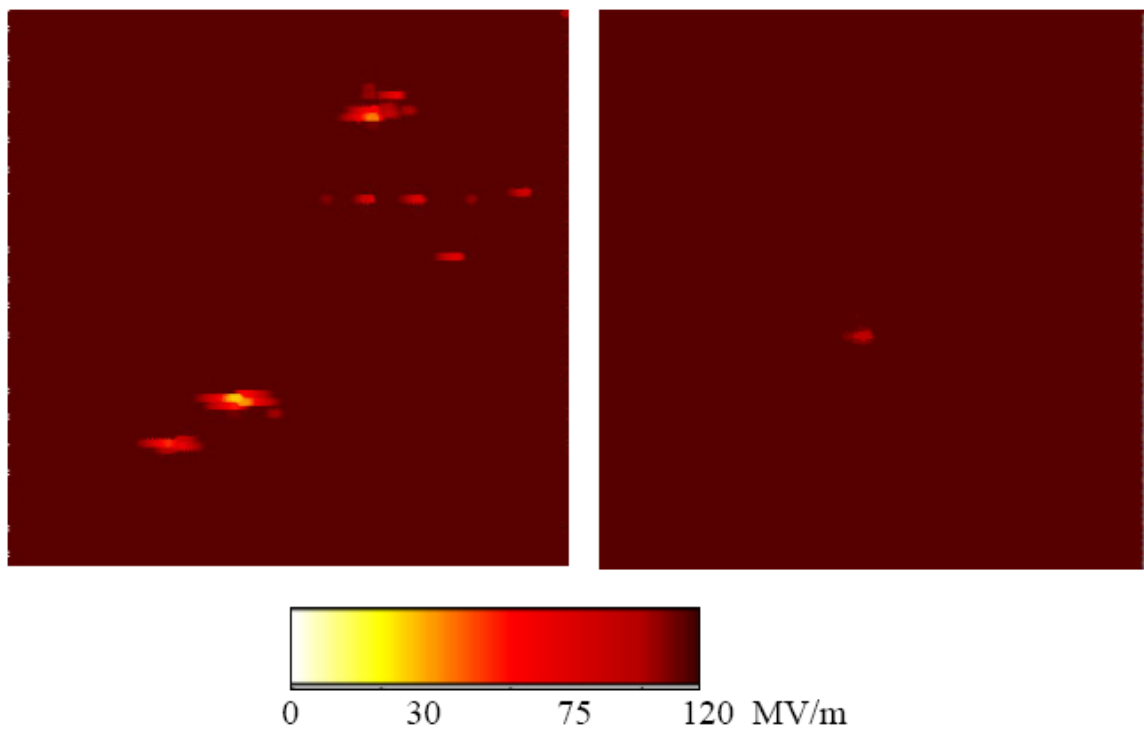


Fig. 4: FE-maps of polycrystalline Nb, performed with a conical anode ($100\mu\text{m}$) over the same (7.5×7.5) mm^2 area before (left) and after (right) DIC at 120 MV/m.

The PolyNb samples were first scanned with 300 μm anode over the area of (12×12) mm^2 at low fields (40, 60, 90 MV/m) and then with 100 μm anode over (7.5×7.5) mm^2 area at 120 MV/m. Both samples showed before DIC first emission of (1, 2) emitters at 60 MV/m, which disappeared after DIC and improved to (2, 0) emitters at 90 MV/m and (2, 3) at 120 MV/m. The great improvement after DIC for one of the samples is shown in Fig. 4. Only one emitter survived but has been weakened by DIC, as seen from the field scales of the maps. For a more detailed interpretation, strong emitters were investigated locally in FESM and SEM and will be discussed in sections (b) and (c).

FE maps of CryNb samples have shown very good results even before DIC: for large grain Nb (0, 2) at 120 MV/m, (5, 3) at 150 MV/m and (10, 12) at 200 MV/m, and for single-crystal Nb no emission up to 120 MV/m, (2, 1) emitters at 150 MV/m and (5, 9) at 200 MV/m. It is most interesting that DIC further improves such high quality surfaces. Three samples, one large grain Nb and two single crystal, were dry ice cleaned and showed no FE up to 150 MV/m, but (2, 0, 1) emitters at 200 MV/m and 250 MV/m. FE maps of one sample at the maximum fields before and after DIC are given in Fig. 5. The main observations are: (i) removal of all old emitters after DIC, showing the effectiveness of this cleaning technique; and (ii) existence of one new emitter at 250 MV/m (which occurred already at 200 MV/m).

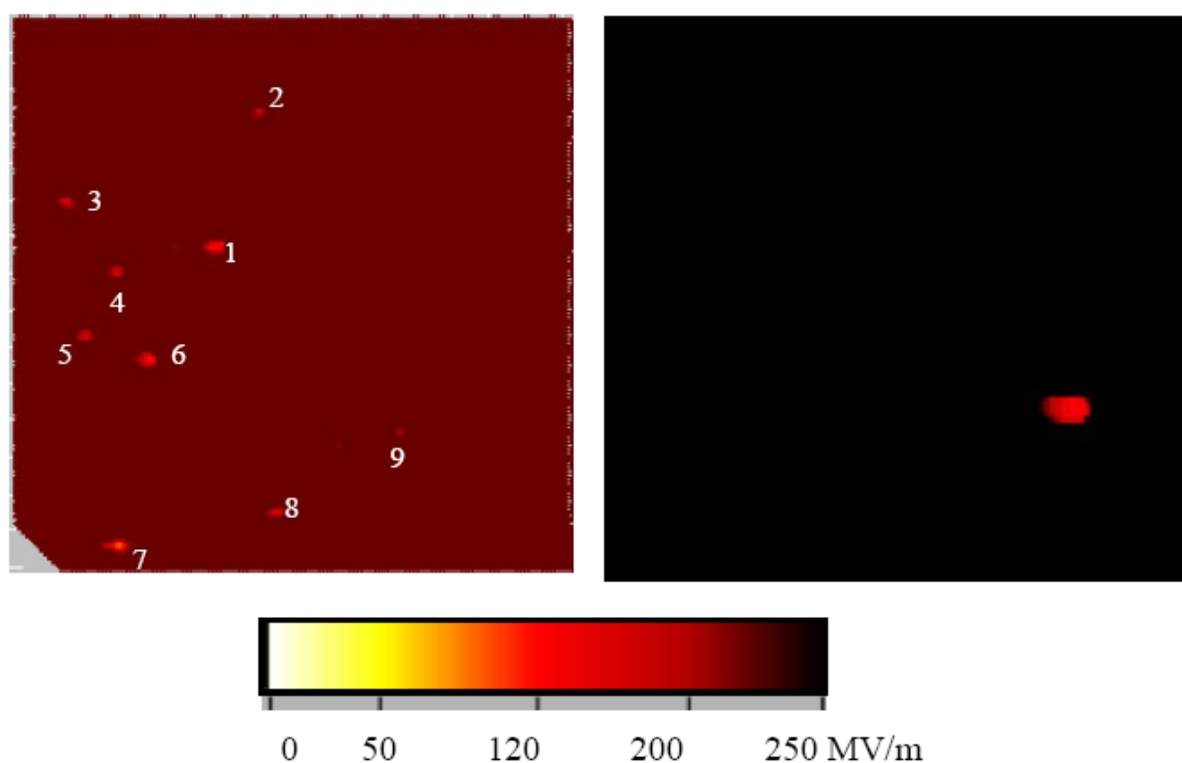


Fig. 5: FE-maps of single crystalline Nb, performed with a conical anode (100 μm) over the same (5×5) mm^2 area before (left) and after (right) DIC at 200 and 250 MV/m, respectively.

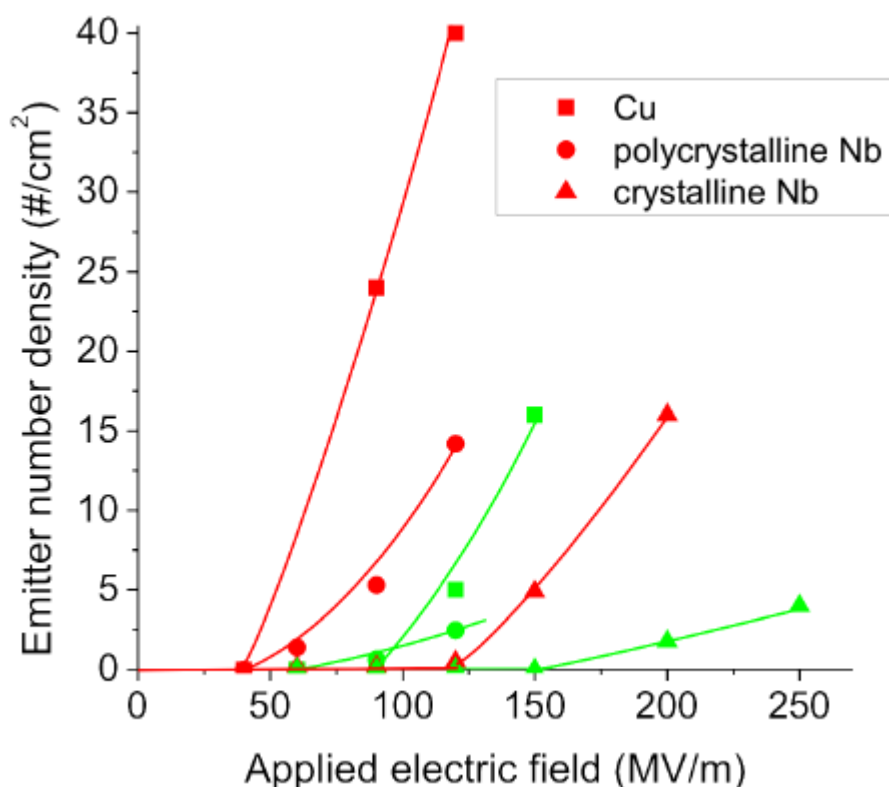


Fig. 6: Emitter number density vs. applied electric field for showing the improvement by DIC for the different materials. (Red symbols: before DIC and green symbols: after DIC).

A statistical overview of the number density of emitters N for the varying electric field E is presented in fig.6. In order to reduce the statistical error and to simplify the $N(E)$ plot, we summed up all the results for a particular kind of samples, i.e. the corresponding areas and number of emitters were added at the scanned field levels. Thus, only six lines for the three different kinds of samples before and after DIC summarize all the scan results. From the statistical plot, the beneficial effect of DIC on these metallic surfaces is obvious: (i) shift of $N(E)$ curves to right, i.e. onset of FE observed at higher fields; and (ii) $N(E)$ curves with much reduced slope, i.e. huge reduction of the number density of field emitters at a given field level. Within statistical errors, for Cu and PolyNb no FE was observed up to 60 MV/m before and 90 MV/m after DIC, and for CryNb up to 150 and 200 MV/m, respectively. It is remarkable that one of the DIC single crystal sample did not show any FE up to 250 MV/m.

4.3.2. FN analysis and stability of emitters

The majority of the localized emitters on all scanned samples were analyzed with FESM. The current-voltage characteristics of the emitting sites were found to obey the modified FN law.³ Accordingly, the linear fitting of $\ln(I/E^2)$ vs $1/E$ plot gives the field enhancement factor β for a given work function Φ from its slope and the effective emission area S from its intercept. Fig. 7 shows an I-V curve for a typical emitter on DIC Cu surface,

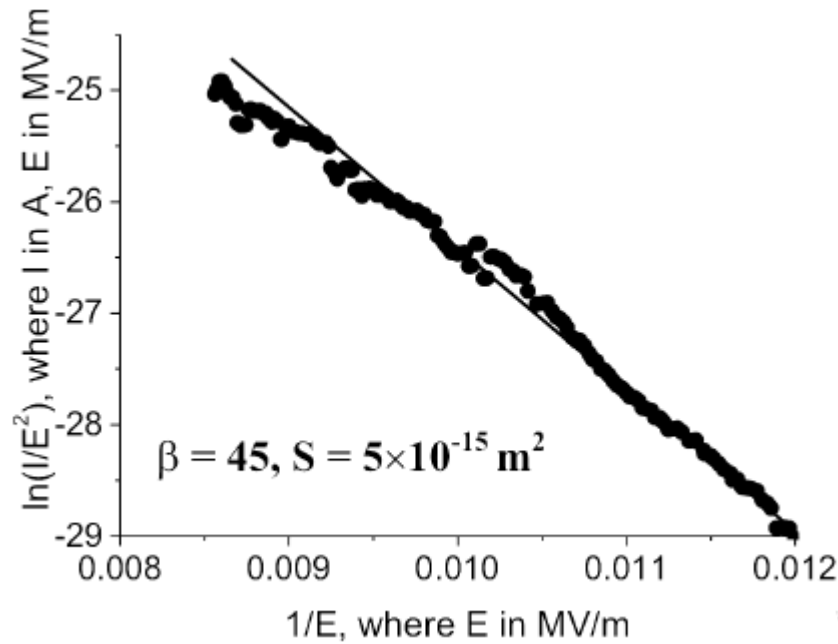


Fig. 7: I-V curve for a typical emitter on dry ice cleaned Cu sample, with β , S values derived for $\Phi = 4.4$ eV from its FN fit (solid line).

resulting in a characteristic β value of 45 and S value of $0.005 \mu\text{m}^2$. These values seem to be reasonable for a particulate or protrusion of size h ($\sim \mu\text{m}$) and sharp edge radius r (~ 10 nm), since $\beta = h/r$ and $S = r^2$.²¹

The impact of DIC on individual emitters can be seen by the changes in their respective I-V curves before and after cleaning, as shown for PolyNb in fig. 8. The large shift to the left means a drastic increase of the E_{on} values, both for a scratch and a particulate. The changes observed in the derived β and S values are: β decreased from 51 to 38 for the

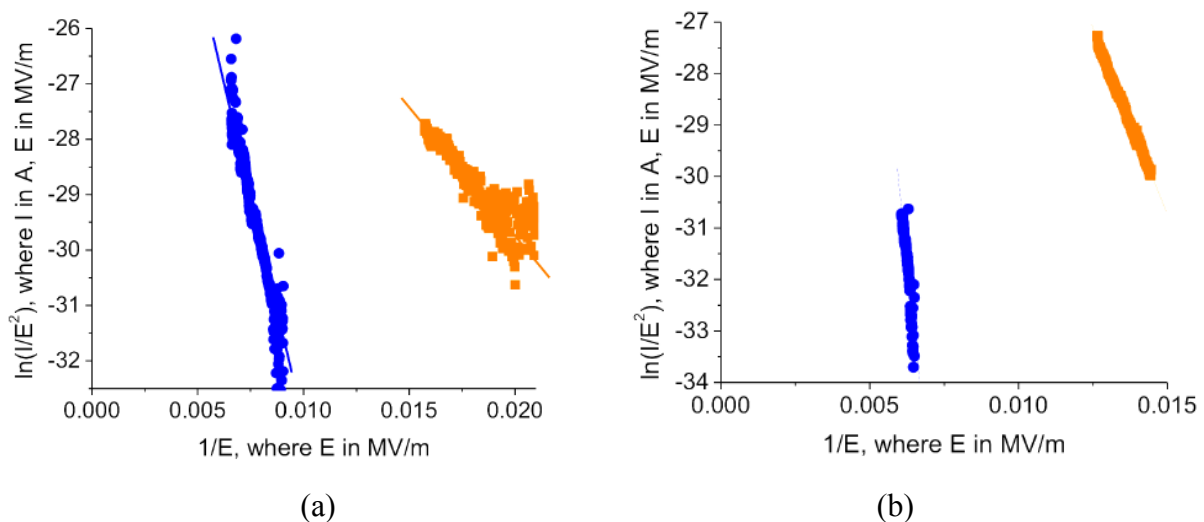


Fig. 8: FN plots for a typical particulate (a) and protrusion (b) on electropolished Nb sample before (■) and after (●) DIC.

particulate and from 148 to 31 for the scratch, while S increased from 1×10^{-15} to $2 \times 10^{-13} \text{ m}^2$ for former and from 7×10^{-20} to $3 \times 10^{-16} \text{ m}^2$ for latter. Decreased β and increased S values can be understood by the smoothed edges of the emitters after DIC. It is remarkable that the particulate shows more current fluctuation than the scratch, as expected from their relative mechanical stability.

Often such current fluctuations lead to preliminary deviations from FN behaviour, which can usually be minimized by high current processing. The I-V curves for a typical particulate on CryNb (Fig.9 a) show: (i) FN behaviour with increasing field, which seems to be saturated on reaching currents of few nA, but is finally followed by a current jump, (ii) the curve retraces more stably for decreasing field values. While the stabilized FN fit values ($\beta = 48$, $S = 9 \times 10^{-19} \text{ m}^2$) suggest an unchanged geometry of the emitter, the preliminary saturation hints for adsorbate effects.²⁵ The I-V curves for a scratch are given in fig. 9 (b), where the emitter has been irreversibly activated at a current of 30 nA and then attains a stable FN behaviour ($\beta = 61$, $S = 3 \times 10^{-19} \text{ m}^2$) in consecutive cycles of increasing and decreasing voltages. In general comparison, the I-V curves of particulates showed more instabilities than surface protrusions.

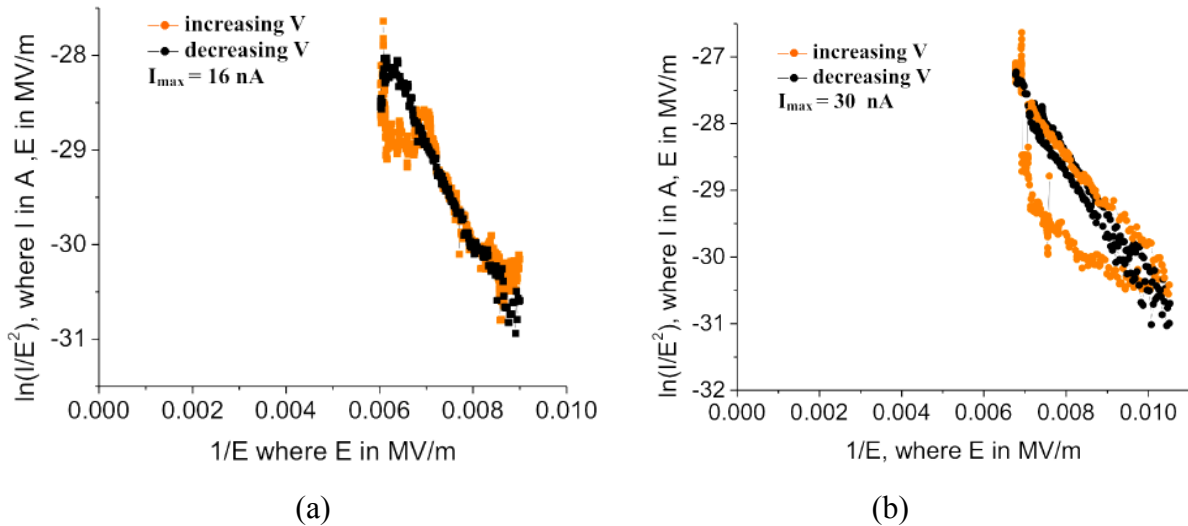


Fig. 9: FN plots for a typical particulate (a) and scratch (b) on BCP-treated single crystal Nb sample showing current processing effects.

In total 54 emitters from all samples have been measured locally for their I-V curves. Representative results for selected emitters are given in table 1, where their characteristic E_{on} , β and S values before and partially after DIC are given. The range of E_{on} in MV/m before DIC is 49 to 84 for Cu and PolyNb, and has been improved by DIC to 63 to 110 for Cu and

Sample_emitter no.	DIC	E_{on} (MV/m)	FN fit parameters		Element detected by EDX	SEM observation	Related figures
			β	$S(\mu\text{m}^2)$			
Cu1_1		67	25	30	n.m.	n.m.	
Cu1_3		84	41	2×10^{-3}	n.m.	n.m.	
Cu1_2	Y	101	38	7×10^{-4}	S, Cu	0.6 μm embedded particulate	10(a)
Cu1_4	Y	105	32	3×10^{-4}	Si, Cu	Contamination inside fissure	10(b)
Cu2_1	Y	103	41	7×10^{-4}	Cu	Scratch with delamination	10(d)
Cu4_1	Y	110	56	3×10^{-6}	Cu	10 μm mark	10(c)
PNb1_2		54	51	1×10^{-3}	Nb	20 μm particulate	8(a) and 11(c)
PNb1_2 ^a	Y	63	38	2×10^{-1}	Nb	Embedded parts	8(a) and 11(d)
PNb1_3		49	148	7×10^{-8}	Nb	Scratch	8(b)
PNb1_3 ^a	Y	103	31	3×10^{-4}	Nb	Scratch	8(b) and 11(b)
PNb1_4		77	18	5×10^{-1}	S, Cl, K	50 μm particulate	11(a)
CNb1_2		88	71	2×10^{-6}	Nb	No feature found	
CNb3_1		128	48	9×10^{-7}	Nb	1 μm particulate	9(a)
CNb4_1		127	61	3×10^{-7}	Si, Nb	Scratch & 0.5 μm particulate	9(b)
CNb4_6		142	59	7×10^{-8}	Nb	1 μm particulate	5
CNb4_5		167	75	4×10^{-9}	Nb	No feature found	5
CNb1_1	Y	116	18.6	3×10^{-2}	Nb	No feature found	
CNb1_5	Y	123	18	6×10^{-2}	Nb	No feature found	
CNb4_2	Y	186	22	4×10^{-3}	Nb	No feature found	

^aSame emitter reidentified after DIC; n.m. means not measured.

Table I: FESM and SEM/EDX results for selected emitters on 10 broad area Cu and Nb cathodes. The FN fit parameters are derived for Φ of 4.4 eV (Cu) and 4 eV (Nb). PNb and CNb corresponds to PolyNb and CryNb samples, resp.

PolyNb. Significantly higher values, i.e. a range of 88 to 167 before and 116 to 186 after DIC, were found for CryNb and underline the benefit of mirror-like surfaces for reduced FE. Most of the β -values, i.e. 25 to 56 for Cu, 18 to 148 for PolyNb and 17 to 76 for CryNb, are inversely correlated to the E_{on} values. The derived S parameters cover rather large ranges, i.e. 30 to 3×10^{-6} μm^2 for Cu and 0.2 to 3×10^{-7} μm^2 for all Nb samples, most of which are reasonable with respect to the β values. The extreme values, however, can not be understood within the modified FN theory.

In order to check if grain boundaries cause enhanced FE, the large-grain CryNb samples were scanned (1 mm^2) with 30 μm resolution over the grain boundary intersections. No emission was observed up to the highest scanned field levels. Despite of the fact that grain boundaries on Nb surfaces can be easily contaminated by segregated impurities, this result suggests that the grain boundary effects play only a minor role for enhanced FE of clean Nb samples.

4.3.3. Morphology and composition of emitters

In order to understand the nature and origin of enhanced FE from metallic surfaces, a total of 31 emitters were relocalized and examined with high resolution SEM and EDX. Figure 10 shows SEM images of various emitters on DIC Cu samples partially with the corresponding EDX spectra. The submicron particulate ($\beta = 38$) with sulphur contaminant in fig. 10 (a) seems to be embedded in the surface, and its dark contrast suggests a conducting

nature. Similar S contaminations up to 5 μm size were found at the emitting sites (β up to 41). Si impurities inside a 10 μm large fissure (fig. 10 b, $\beta = 32$) also survived after DIC. Thus, the foreign elements embedded in the surface or trapped inside the grooves could not be removed completely by DIC. Moreover, the mark of 10 μm size (fig. 10 c, $\beta = 56$) and the large scratch of about 20 μm width (fig. 10 d, $\beta = 41$) were identified as emitters with sharp edges and delaminations, thus causing the enhanced FE.

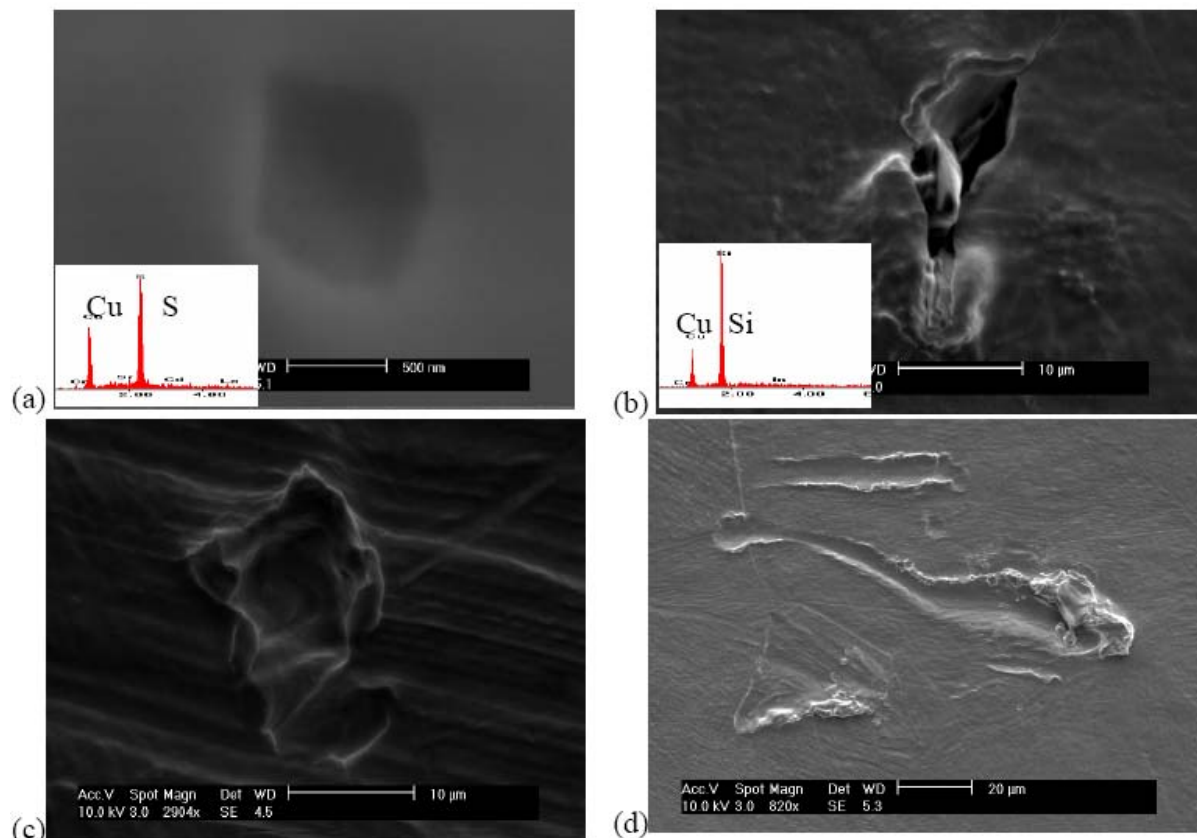


Fig. 10: SEM images with EDX spectra (inserts) of FE sites on DIC Cu: (a) sulphur contaminant of submicron size embedded in the surface, (b) silicon impurities inside a fissure, (c) surface irregularity, and (d) large scratch.

SEM images of some of the emitters found on PolyNb samples are shown in fig.11. The particulate of about 50 μm length in fig.11 (a) contains S, Cl and K and provides a rather small β of 18. Despite of its resistance against HPR, it was completely removed by DIC. Usually all the localized field emitting particulates disappeared after DIC treatment of the samples. Surface irregularities like the mark in fig. 11b reflect mishandling of the surface. In one case, a thin flake-like object of about 20 μm size (fig. 11 c) was partially destroyed by DIC and only some embedded part of it survived (fig. 11 d) and still emitted, as shown in Fig.

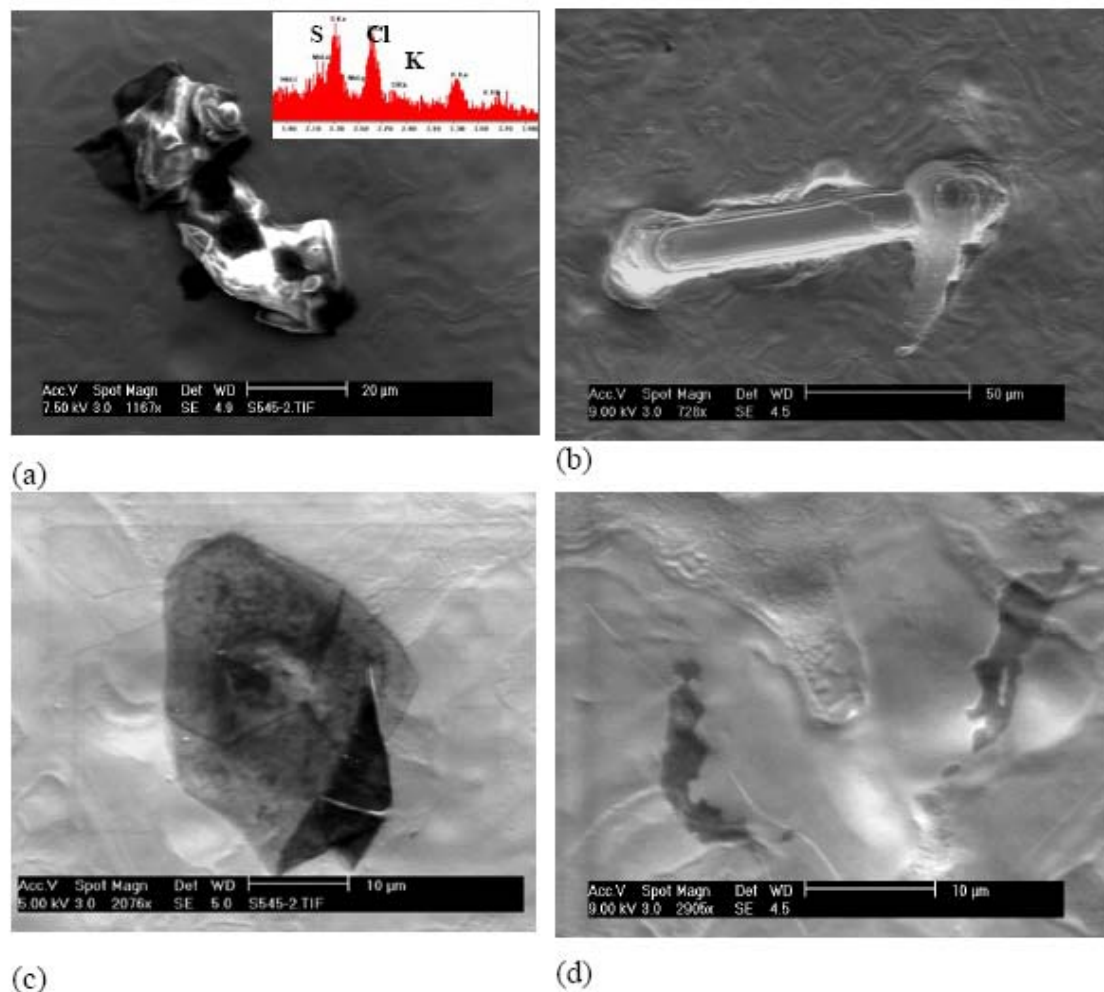


Fig. 11: SEM images of FE sites on polycrystalline Nb: (a) particulate containing sulphur, chlorine and potassium (see inserted EDX spectrum) before DIC, (b) large irregularity on the sample surface after DIC, (c) flake like object before and (d) after DIC, still giving FE.

8 (b). These facts altogether prove the mechanical and thermal effect of DIC on the particulates for the reduction of FE.

On CryNb samples, the particulates localised as emitters before DIC were always removed by DIC. The SEM images given in fig. 12 (a) and (b) prove the removal of a particulate as small as 400 nm in size by DIC from the single crystal Nb surface. The high resolution SEM images of the scratch head (figs. 12 c, d) show softened contours of some protrusions probably due to the mechanical impact of high speed dry-ice particles impinging on the surface. It is remarkable that the Si contaminant disappeared after DIC. No FE from this site is observed up to 250 MV/m, i.e. there seems to be no features with β values above about 10. These results show the strength of the DIC technique even for the removal of submicron particulates as well as for the partial smoothing of surface protrusions.

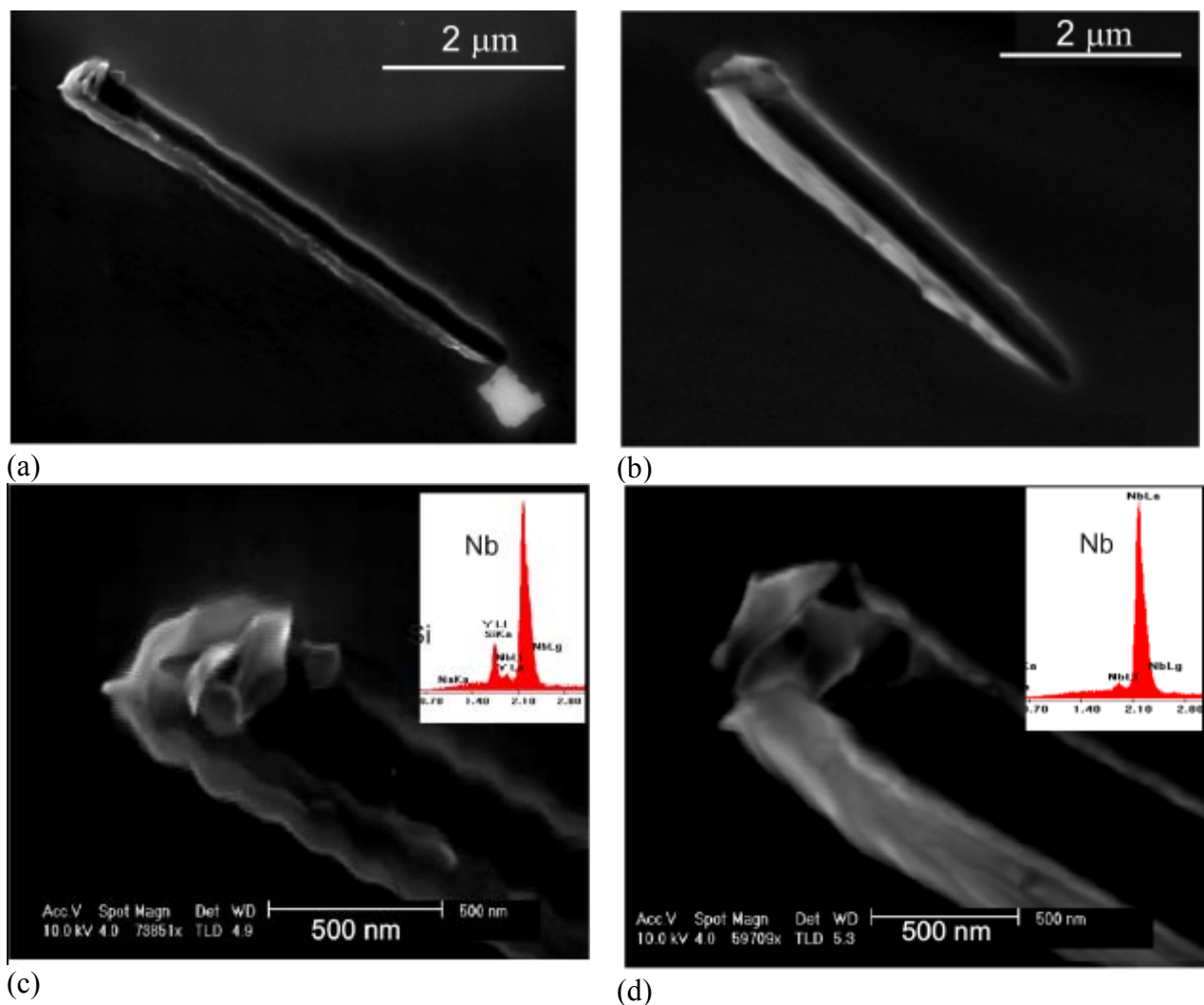


Fig. 12: SEM images of FE sites on single crystal Nb: scratch with a nearby lying submicron particulate of size ~ 400 nm before (a) and after (b) DIC, high resolution picture and EDX spectra of the scratch head before (c) and after (d) DIC.

FE properties and SEM/EDX results (Table 1), the emitters can be categorised as follows: (i) particulates with or without contaminants, (ii) features embedded in the surface, (iii) surface protrusions with or without contaminants, and (iv) grooves with trapped contaminants. DIC effectively removes emitters of type (i), and weakens emitters of type (iii), while types (ii) and (iv) are less affected. It should be remarked that 19 out of 51 localised emitters did not show any feature in high resolution (< 5 nm) SEM. This probably hints for the presence of some embedded impurities with low work function.

4.4. Conclusions

DIC has been found to be a very efficient technique for the reduction of FE sites from Cu and Nb surfaces. The remaining emitters found on various FE maps statistically appear at much higher electric fields. The best DIC single crystal Nb sample did not provide any FE up

to 250 MV/m. Selected emitters localised in FESM and identified in SEM have been categorised depending on their shape and impurity content. The I-V curves of most emitters confirm the modified FN theory with reasonable β and S values. In comparison, particulates showed more current instabilities than surface protrusions, as expected from their relative mechanical stability. E_{on} values of all emitters have been significantly improved by DIC. The highest values were achieved for CryNb, i.e. (88 – 167) MV/m before and (116 – 186) MV/m after DIC, thus, underline the benefit of mirror-like surfaces for reduced FE. Large grain Nb samples do not show any emission from grain boundaries up to 250 MV/m. SEM images of typical emitters prove that DIC removes particulates down to 400 nm size and partially smoothens the edges of protrusions.

Acknowledgments

We would like to acknowledge A. Aspart and C. Antoine from CEA Saclay for electropolishing of the polycrystalline Nb samples, A. Brinkmann and J. Ziegler from DESY as well as R. Grimme and C. Zorne from Fraunhofer IPA for experimental support of the DIC apparatus. We are thankful to the Electrical Engineering Department at BUW for access to SEM and EDX facilities. Stimulating discussions with W. Singer and D. Proch from DESY as well as C. S. Pandey from BUW are highly acknowledged. The support of the European Community Research Infrastructure Activity under FP6 “Structuring the European Research Area” program (CARE, contract number RII3-CT-2003-506395) is gratefully acknowledged.

References

- [1] R. V. Latham, *High Voltage Vacuum Insulation: Basic concepts and technological practice* (Academic Press, London, 1995).
- [2] H. Padamsee, J. Knobloch, and T. Hays, *RF Superconductivity for accelerators* (John Wiley & Sons, New York, 1998).
- [3] R. J. Noer, *Appl. Phys. A* 28, 1 (1982).
- [4] R. H. Fowler and L. Nordheim, *Proc. R. Soc. London A* 119, 173 (1928).
- [5] R. J. Noer, Ph. Niedermann, N. Sankarraman, and O. Fischer, *J. Appl. Phys.* 59, 3851 (1986).
- [6] E. Mahner, N. Minatti, H. Piel, and N. Pupeter, *Appl. Surf. Sci.* 67, 23 (1993).
- [7] N. Pupeter, T. Habermann, A. Kirschner, E. Mahner, G. Müller, and H. Piel, *Appl. Surf. Sci.* 94/95, 94 (1996).
- [8] N. Pupeter, A. Göhl, T. Habermann, A. Kirschner, E. Mahner, G. Müller, and H. Piel, *Particle Accelerators* 53, 77 (1996).
- [9] T. Wang, C. E. Reece, and R. M. Sundelin, *J. Vac. Sci. Technol. B* 21, 1230 (2003).
- [10] A. Dangwal, D. Reschke, and G. Müller, *Physica C* 441, 83 (2006).
- [11] R. A. Bowling, in *Particles on surfaces*, edited by K. L. Mittal (Plenum, New York, 1988), vol.1, p.129.
- [12] P. Kneisel and B. Lewis, *Proc. of 7th Workshop on RF Superconductivity, Gif sur Yvette, France*, ed. by B. Bonin, p. 311, (1995).
- [13] R. Sherman and W. Whitlock, *J. Vac. Sci. Technol. B* 8, 563 (1990).
- [14] R. Sherman, J. Grob, and W. Whitlock, *J. Vac. Sci. Technol. B* 9, 1970 (1991).
- [15] R. Sherman, D. Hirt, and R. Vane, *J. Vac. Sci. Technol. A* 12, 1876 (1994).
- [16] D. Proch, D. Reschke, B. Guenther, G. Müller, and D. Werner, *Proc. of 10th Workshop on RF Superconductivity, Tsukuba*, p. 463 (2001).
- [17] L. Layden and D. Wadlow, *J. Vac. Sci. Technol. A* 8, 3881 (1990).
- [18] C. Suzuki, T. Nakanishi, S. Okumi, T. Gotou, K. Togawa, F. Furuta, K. Wada, T. Nishitani, M. Yamamoto, J. Watanabe, S. Kurahashi, K. Asano, H. Matsumoto, M. Yoshioka, and H. Kobayakawa, *Nucl. Instr. and Meth. A* 462, 337 (2001).
- [19] D. Reschke, *Proc. of 12th Workshop on RF Superconductivity, Cornell Univ., SUP03* (2005).
- [20] D. Lysenkov and G. Müller, *Int. J. Nanotechnol.* 2, 239 (2005).
- [21] T. Habermann, PhD thesis, Univ. of Wuppertal (1999).
- [22] D. Werner, C. Zorn, *Proc. Precision Cleaning, Clean Tech, Frankfurt*, (2000).

- [23] D. Werner, P. Fode, H. Schöne, *Cleanroom Technology*, issue Feb 2001, p. 35.
- [24] A. Brinkmann, J. Iversen, D. Reschke, J. Ziegler, *Proc. of the Europ. Particle Accelerator Conf.*, Edinburg, p. xx (2006)
- [25] T. Habermann, A. Göhl, D. Nau, G. Müller, H. Piel, and M. Wedel, *Particle Accelerators* 61, 137 (1998).

Chapter 5

Field emission from single crystal and large grain niobium cathodes

Arti Dangwal, Günter Müller, Detlef Reschke, Xenia Singer

Submitted to 13th International Workshop on RF Superconductivity (SRF 2007)

Abstract

Appreciable suppression of field emission from metallic surfaces has been achieved by the use of improved surface cleaning techniques, and dry ice cleaning has emerged recently as a very effective tool in this respect. In order to understand the effects of surface preparation on field emission, systematic measurements were performed on five single crystal and three large grain samples of high purity ($RRR > 300$) Nb by means of AFM, XRD, SEM and dc field emission scanning microscope. The samples were treated with buffered chemical polishing (BCP), half of those for 30 μm and others for 100 μm removal of surface damage layer, followed by a final high pressure water rinsing. The samples with longer BCP treatment showed the onset of field emission at slightly higher fields. A low temperature (~ 150 °C) heat treatment in high vacuum (10^{-6} mbar) chamber for 14 hours, on a selected large grain Nb sample, gives the evidence for the grain boundary assisted FE at very high fields of 250 and 300 MV/m. Finally, an interesting correlation between sizes of all investigated emitters derived from SEM images with respect to their respective onset fields has been found, which might facilitate the quality control of superconducting radio-frequency cavities for linear accelerators.

5.1. Introduction

Highly purified fine grain niobium sheets ($RRR > 250$) have been used worldwide for the fabrication of high gradient superconducting accelerator cavities in various projects like FLASH [1], SNS [2] and RIA [3]. Much attention has been given to the surface preparation and cleanliness techniques, which has suppressed significantly the enhanced field emission (FE) of electrons from the cavity surface and thus improved the regular cavity performance at high accelerating gradients, e.g. up to about $E_{\text{acc}} = 30$ MV/m for nine-cell 1.3 GHz structures [4]. High pressure rinsing (HPR) with ultra pure water is used as standard technique for the final cleaning of such cavities [5], while dry ice cleaning (DIC) has emerged recently to be very effective tool in this respect [6]. The best DIC single crystal Nb sample did not provide any FE up to a electric surface field E_s ($\approx 2E_{\text{acc}}$) of 250 MV/m. Further, the removal of field emitting particulates down to 400 nm size and partial smoothing of edges of the protrusions by DIC of Nb surface was also reported.

An approach towards improving the cavity fabrication for future linear accelerators like XFEL [7] and ILC [8] has been made by using buffered chemically polished (BCP) large grain Nb (LGNb) or single crystal Nb (SCNb) instead of electropolished (EP) polycrystalline Nb, which might be less expensive due to the elimination of sheet fabrication and related processes. Preliminary tests of single cell cavities made from large grain Nb have yielded E_{acc} up to 45 MV/m, which is one of the highest value achieved yet. [9] Further research on multi-cell structures made from large grain or single crystal Nb is required before it can replace polycrystalline Nb. It has also been reported recently that the grain boundaries on large grain Nb cavities provide some, although not dominant, contribution to the hot spots in corresponding thermal maps. [10]. Since grain boundaries get easily contaminated by the segregation of impurities during the usual bakeout of cavities, it is interesting to investigate their role for field emission, too.

In this paper, we report on FE properties and surface characteristics of eight large grain and single crystal samples, measured by means of field emission scanning microscope (FESM) [11], scanning electron microscope (SEM), atomic force microscope (AFM), and X-ray diffraction (XRD). *In-situ* heat treatments at 150 °C were performed on two samples and then measured again to find any change in corresponding FE properties. Intrinsic FE measurements on such a high quality samples were possible due to their very smooth surfaces and the derived ϕ values for different crystal orientations will also be discussed here. Finally, a correlation between sizes of all investigated emitters derived from SEM images and their respective onset fields will be presented.

5.2. Sample preparation and surface quality control

Five single crystal and three large grain Nb samples of 28 mm diameter were fabricated at DESY Hamburg. The RRR value of the material was at least 300 with Ta content of ~ 300 ppm. Final surface preparation using BCP in HF(40%):HNO₃:(65%) H₃PO₄ (85%) in volume ratio 1:1:2 at temperature 12-18°C has resulted in a mirror-like surface. For half of the samples a surface damage layer of 30 μm and 100 μm was removed, respectively, with the intention of finding the impact of longer BCP treatment on the FE properties of the sample surface. AFM and XRD measurements were performed by means of instruments "easyScan AFM" (NanoSurf AG) and Philips PW1830. The details of samples with surface preparation, crystal orientations, and roughness are summarized in Tab. 1.

Sample	Removed damage layer using BCP	Orientation	Surface roughness
SCNb1	30 μm	(110)	11.7 nm
SCNb2	30 μm	(110)	17.6 nm
SCNb3	100 μm	(110)	7.0 nm
SCNb4	100 μm	(111)	6.2 nm
SCNb5	100 μm	(100)	7.5 nm
LGNb1	30 μm	(110), (111), (110)	100, 110.5, 62.7
LGNb2	30 μm	nm	nm
LGNb3	100 μm	(100), (110), (111)	8.8, 6.9, 6.8

Table.1: Overview of the investigated single crystal and large grain Nb samples. (nm used for not measured samples)

The high resolution optical microscopic images of samples SCNb5 and LGNb3 in Fig 1(a) and (b)) demonstrate the appearance of different grains of niobium, and the AFM image in Fig 1 (c) provides the surface roughness value of 7.5 nm for Nb(100) oriented surface (Fig. 1 (d)). 100 μm polished single crystal Nb surfaces possess less surface roughness (6-7.2 nm) than 30 μm polished ones (12-17.5 nm), while the large grain samples become as smooth only for 100 μm BCP. All the samples were especially marked during fabrication to adjust the sample position in different experimental set-ups and were finally rinsed with ultra pure water and HPR.

The FE measurements were performed on the flat Nb cathodes under ultrahigh vacuum conditions in FESM, using conical anodes. The samples were first scanned over a

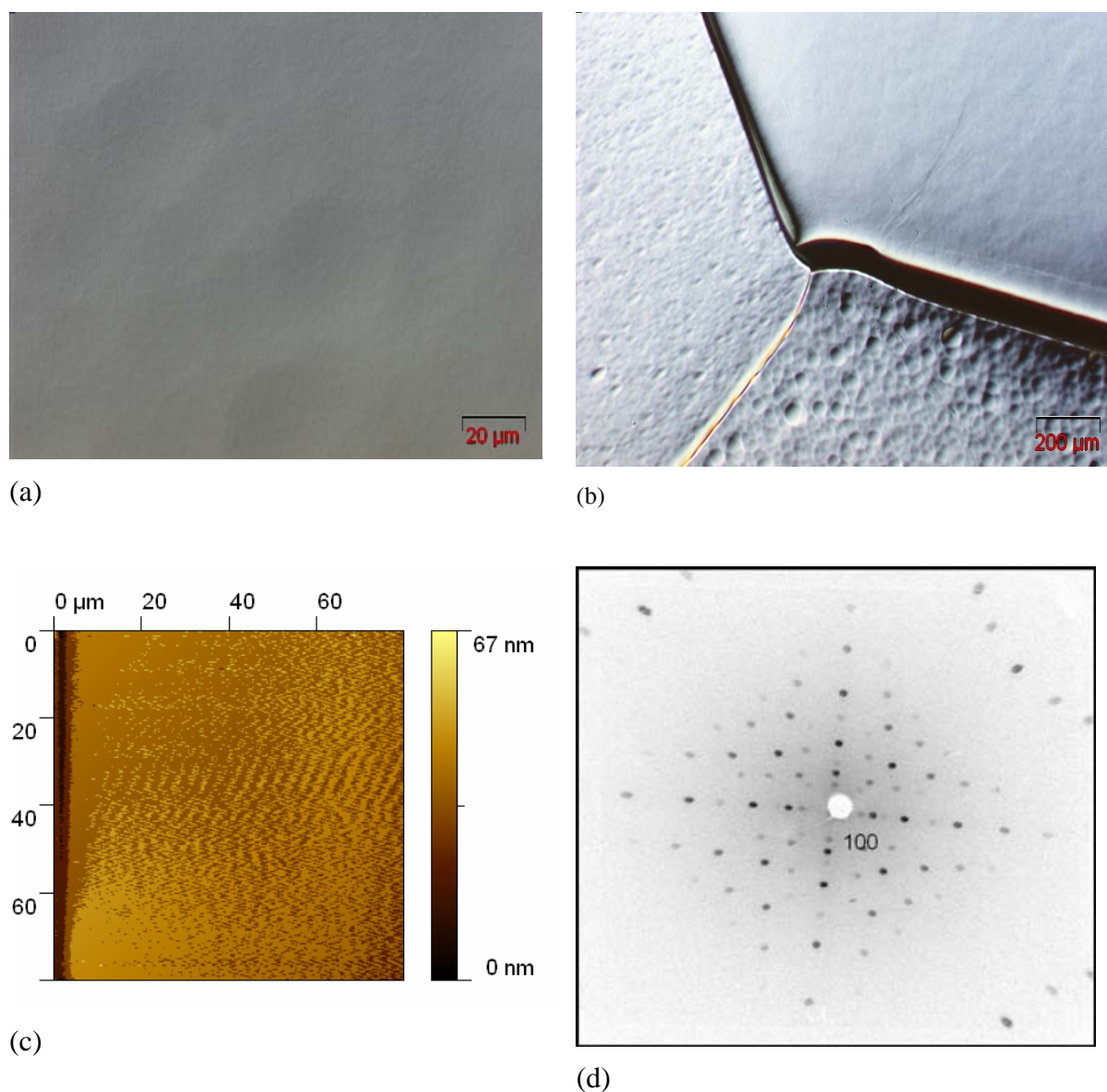


Fig. 1: (a) High resolution optical microscope image of sample SCNb5, (b) microscopic view of intersection of grain boundaries on large grain sample LGNb3, (c) AFM image of sample SCNb5 showing root mean square roughness of 7.5 nm over $(80 \times 80) \mu\text{m}^2$ area, and (d) XRD image of SCNb5 revealing (100) orientation.

selected area of (12×12) and $(10 \times 10) \text{mm}^2$ at 90 and 120 MV/m with 300 μm anode and then at 150 and 200 (or 250 and higher) MV/m with 100 μm anode over the areas of (7.5×7.5) and $(5 \times 5) \text{mm}^2$, respectively. The strong emitters in the observed electric field (E) maps were localized and studied for their individual FE properties. An oven (Kamrath and Weiss) with Pt100 resistor, installed in the high vacuum chamber of FESM, was used to heat the samples

at 150 (± 10) °C. Efforts were made finally to identify the emitters ex situ in SEM and to reveal their origin from geometrical features and chemical compositions with EDX.

5.3. Field emission results and discussion

5.3.1. Statistical overview of the emitters

All large grain and single crystal Nb samples have provided very good results, as summarized in Tab. 2. FE maps on large grain Nb samples showed the onset of FE at 120 MV/m for 30 μm and at 150 MV/m for 100 μm polished surfaces. For single crystal Nb

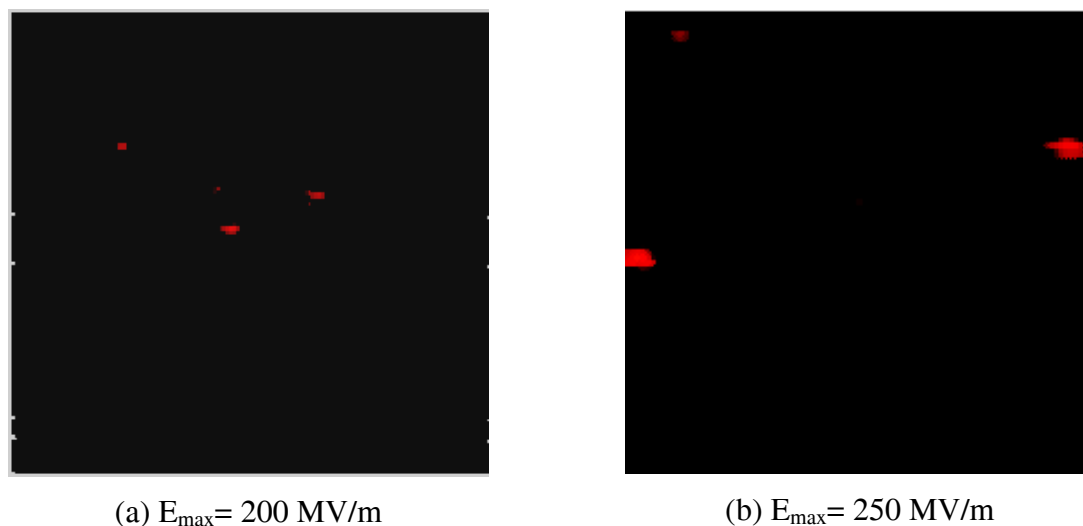


Fig. 2: E-maps for (a) SCNb1 and (b) SCNb5, over the area of $(5 \times 5) \text{ mm}^2$ using a 100 μm conical anode. The red dots reveal 5 and 3 emitters at onset fields (for 2 nA) of about 200 and 250 MV/m, respectively.

sample with 30 and 100 μm BCP, the onset of FE was observed at 150 MV/m and 200 MV/m, respectively. The typical FE maps, given in Fig. 2, show the observed emitters at the highest scanned field levels for these two cases. If we compare the number of emitters at different field levels for all samples from Table 2, a marked difference between 30 μm BCP'd LGNb samples (LGNb1 and 2) and all others is observed. It is interesting to discover that it can be directly related to the large difference in the surface roughness values, which is of the order of 100 nm for former and about 10 nm for the later (Tab. 1). Thus, FE was strongly suppressed for smoother surfaces.

Sample	Number of emitters			
	@ 120 MV/m over (10mm) ²	@ 150 MV/m over (7.5mm) ²	@ 200 MV/m over (5mm) ²	@ 250 MV/m over (5mm) ²
SCNb1	0	2	5	-
SCNb2	0	1	9	-
SCNb3	0	0	3	9
SCNb4	0	0	2	7
SCNb5	0	0	2	3
LGNb1	2	5	10	-
LGNb2	0	3	12	-
LGNb3	0	1	4	11

Table 2: Emitters observed in FE maps of all Nb samples (s. Tab. 1) at different field levels.

A statistical overview of the number density of emitters N for varying electric field E is presented in Fig.3. In order to reduce the statistical error and to simplify the $N(E)$ plot, all the results for a particular kind of samples have been summed up, i.e. the corresponding areas

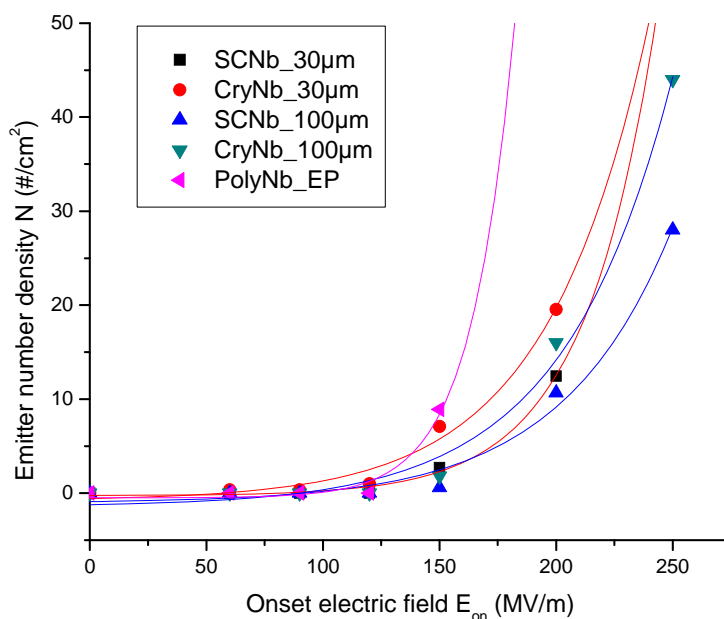


Fig. 3: Emitter number density vs. applied electric field for different damage layer removal. (Exponential fit lines: Red for 30 μm BCP, blue for 100 μm BCP, and magenta for EP polycrystalline Nb sample)

and number of emitters were added at the given scanned field levels. Within statistical errors, for LGNb with 30 and 100 μm BCP, the onset of FE was observed at 120 and 150 MV/m, while for SCNb at 150 and 200 MV/m, respectively. Despite of a significant statistical error, for more damage layer removal there is a tendency of $N(E)$ exponential fit lines to shift to the right, i.e. to higher onset fields and an evidence for reduced slopes, i.e. less number density of field emitters at a given field level. For comparison with the best quality electropolished Nb samples, the corresponding fit line has also been plotted, showing clearly the better performance of SCNb and LGNb samples. These observations are consistent with the earlier findings that the damage layer greater than 50 μm has to be removed for better cavity performance. [12, 13]

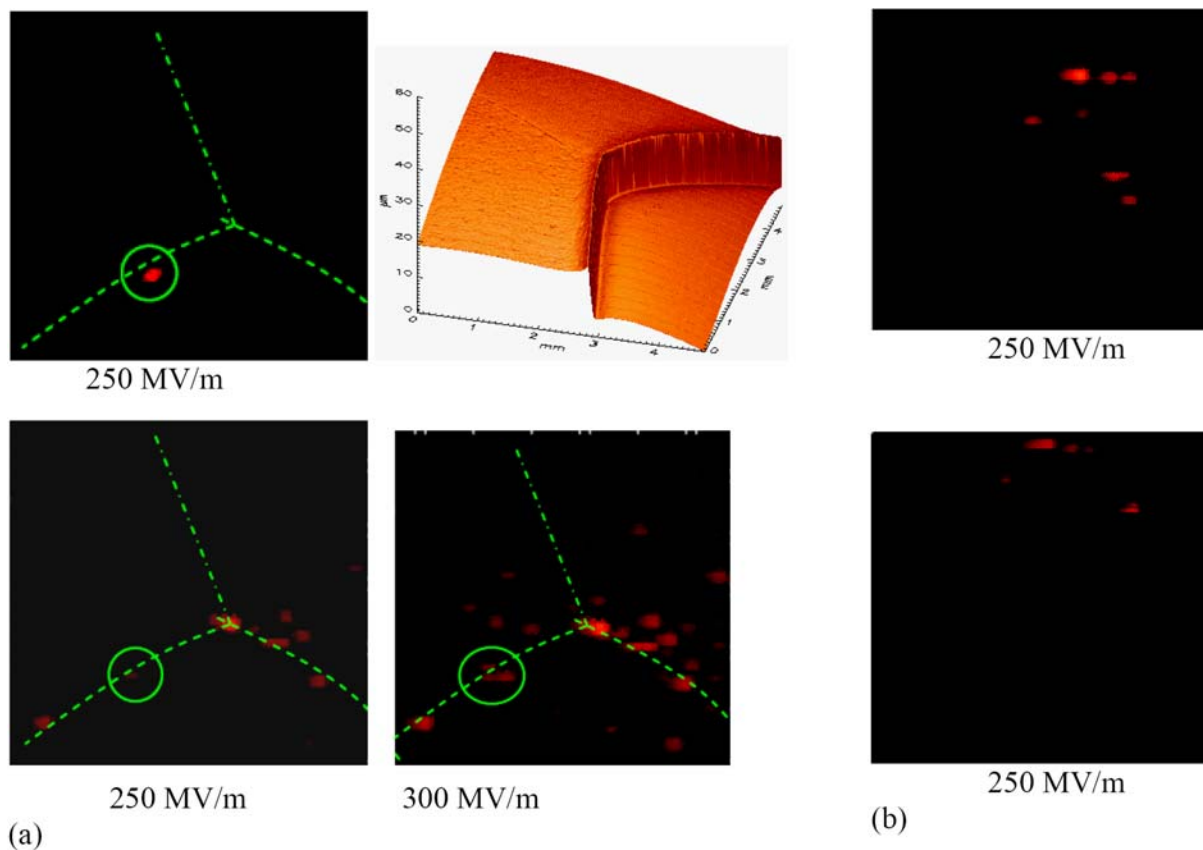


Fig. 4: (a) E-maps of LGNb3, and surface profile (measured with FRT MicroProf®) showing grain boundaries. The encircled emitter is the one activated before HT, and dotted lines in the scan represent the grain boundaries. (b) E-maps for SCNb4: the vertical shift of scans before and after HT is an experimental artifact. All the scans were made on the same area of $(5 \times 5) \text{ mm}^2$ scanned before (upper) and after 150°C heat treatment (lower row) up to the given maximum fields.

5.3.2. Grain boundary effects and low temperature heat treatment

Present high quality Nb samples should be informative to study any grain boundary effect on FE, due to the presence of either no grain boundary or very few but large grain boundaries easily visible on the sample surface. However, no FE was observed from grain boundaries up to the field of 250 MV/m from any of the as-prepared large grain Nb samples.

Heat treatment (HT) of polycrystalline Nb cavities at low temperatures (100 – 150 °C) is used as a final preparation step, which improves the quality factor of cavities probably by the diffusion of oxygen from surface oxide into the bulk niobium. [14] Analogous to this cavity treatment, we have selected two samples LGNb3 and SCNb4 for low temperature heat treatments at 150°C for 14 and 8 hours, respectively. The corresponding FE maps made after HT are shown in Fig.4. It is interesting to find that on the LGNb sample, most of the emitting sites were activated near or on the grain boundaries, which are 89% at 250 MV/m and 63% at 300 MV/m of total number of emitters. No features in SEM were observed corresponding to these emitters. Two grain boundaries possessing more emitters nearby have the step height of ~ 12-15 μm , while the third one has the step height less than 0.5 μm , as measured by the Profilometer (Fig. 4 (a)). Further it is notable that the strongest emission is observed at the intersection of three grain boundaries. On the other hand, the number of emitters for SCNb remained unchanged up to 200 MV/m as before HT, while at 250 MV/m, one new emitter appeared, and three old emitters disappeared (Fig. 4 (b)). Within statistical error, low temperature HT on SCNb did not show any change on its FE properties. Thus, first evidence for grain boundary assisted FE is observed on LGNb, but only after HT. This is due to easier segregation of impurities along grain boundaries during HT. Our results also show the need of performing similar measurements at higher temperatures for comparison with 800 °C annealing of cavities. More samples measurements are required for a better understanding of grain boundary effects on FE, and should be analyzed with SEM before and after HT.

5.3.3. Single emitter investigations

The strong emitters appearing in the FE maps of all scanned samples were localized in FESM as well as in SEM (later on) to study their individual FE characteristics with respect to their physical properties. In all cases, the observed emission confirmed FN theory with local field enhancement [15]. Moreover, the phenomenon of activation, deactivation and stabilization of the emitters were generally observed in the continuous up and down cycles of applied electric fields during I-V measurements. The features observed for emitters in SEM

investigations, were generally surface irregularities (67%) and particulates (33%) with or without foreign elements present. On 100 μm polished samples, presence of a foreign element (aluminium) was detected only in one case (Fig 5 (a)), which might have come from the Al cap used in the transport system of the samples. The corresponding FN curves are changing in different increasing and decreasing modes of electric fields showing the emitters not being stable and might not be properly connected to the surface. The retrieved β value of 26 and S value of $6 \times 10^{-6} \mu\text{m}^2$ seem reasonable for the nm size sharp features present on this flake like object, which might dominate to the local field enhancement.

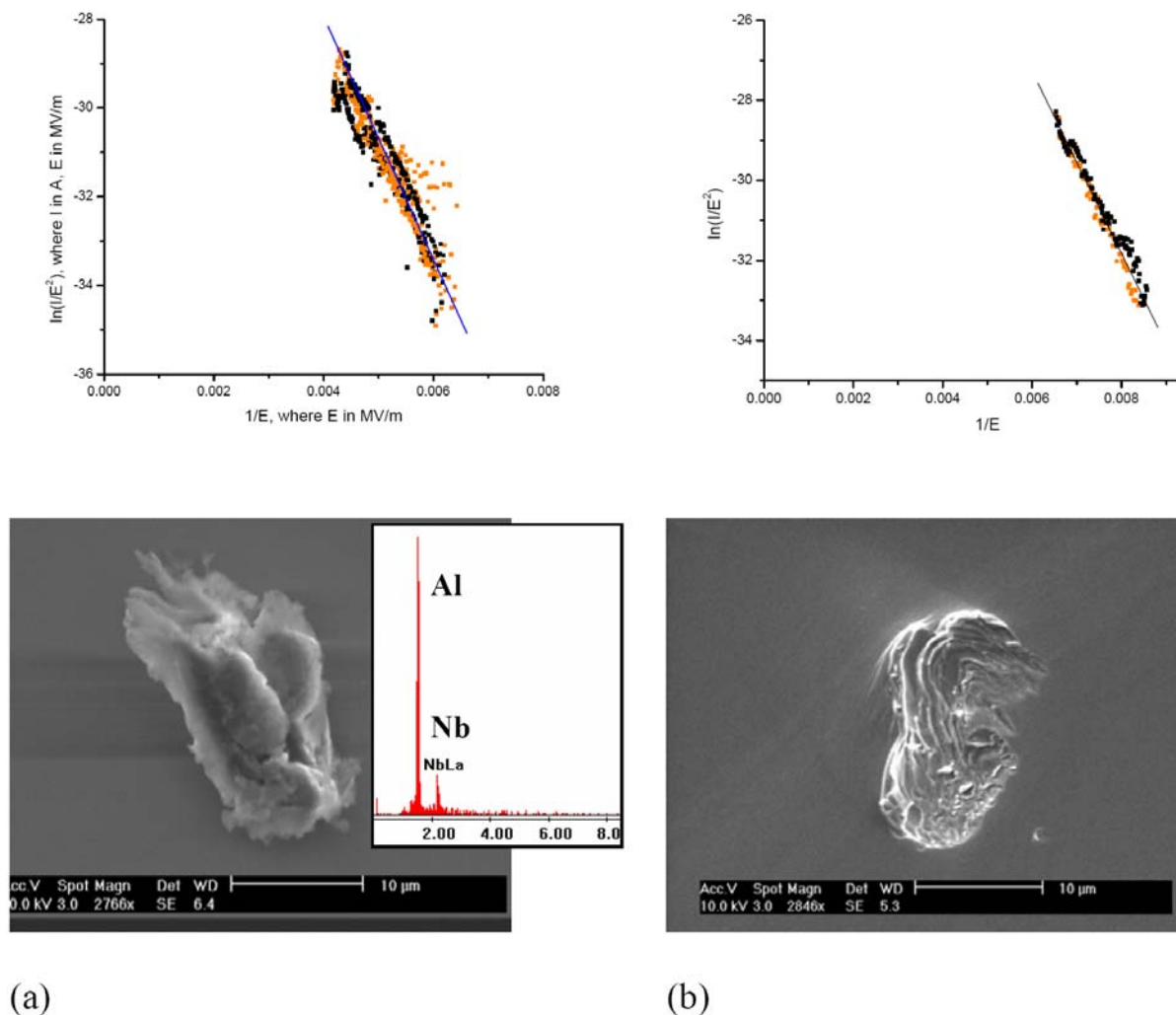


Fig. 5: I-V curves as FN plots of two emitters measured locally in FESM and corresponding SEM images (a) on SCNb7, showing an Al particulate, and (b) on SCNb4, a surface irregularity.

In the case of heat treated samples, it was interesting to find that the FN curves of all the emitters were rather straight, i.e. showing stable FN behaviour probably due to good contact of emitters with the smooth surface. A typical example is given in Fig. 5 (b). The retrieved β and S values on HT samples were found in the range of (12-57) and (10^{-3} - 10^{-7}) μm^2 , respectively, which are very reasonable for a nanometer to sub-nanometer size effective emission area.

5.3.4. Intrinsic FE measurements

The superior quality of presented single crystal Nb samples makes them suitable for intrinsic FE measurements. These measurements require absolutely clean cathode surface and anode tips, and a very small vacuum gap (down to 2 μm) for gaining high fields of ~ 1 GV/m by means of the 5 KV power supply. Samples SCNb4 of (111) and SCNb7 of (100) orientation were measured in defect free areas with the freshly prepared W anodes of 5-20 μm tip diameter. Since the measurements were very much sensitive to system vibrations, the

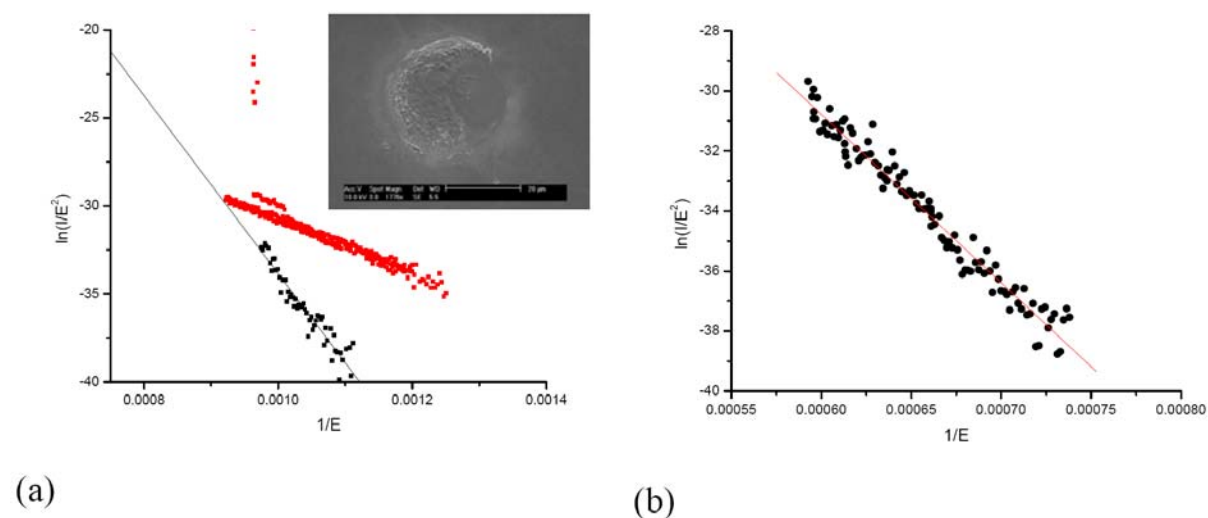


Fig. 6: I-V curves as FN plots locally measured on sample (a) SCNb4, showing the creation of an emitter by a microdischarge with resulting surface damage (inset SEM image) and (b) SCNb7, showing intrinsic field emission of Nb ($\beta = 1$, $\Phi = 4$ eV).

anode tips as well as the sample surface were often damaged during measurements by microdischarges, (inset of Fig. 6 (a)). The measured FN curves exhibit real FN-like behaviour (Fig. 6), showing the onset of FE at fields higher than 1 GV/m. Assuming β equal to one for our smooth and single crystal samples, we retrieved the ϕ values of Nb with respect to different orientations from FN curves. The fitted mean ϕ values for Nb (111) and Nb (100)

are 4.05 and 3.76 within the error of 17 % and 27 %, respectively. These values are in accordance to literature data for the given orientations of Nb. [16, 17] Earlier reported intrinsic measurements on chemically polished polycrystalline Nb have resulted in β values of about 2 on considering a work function ϕ of 4 eV for Nb. [18] On the basis of these results, we conclude that according to the effective protrusion model [19], surface roughness surely enhances the β of particulates and thus the field emission of polycrystalline Nb cavities.

5.3.5. Emitter size vs. onset electric field (E_{on})

In the last three years, we have measured many samples with different types of Nb surfaces (EP polycrystalline and BCP large grain or single crystal). The analysis of localized emitters in FESM and SEM has resulted in a suggestive plot (Fig. 7) of emitter size derived from SEM images vs. corresponding onset electric fields. Particulate emitters are represented there with their average size and surface irregularities with their widths, because e.g. for a scratch it is the parameter deciding over the height of the edges which causes EFE.

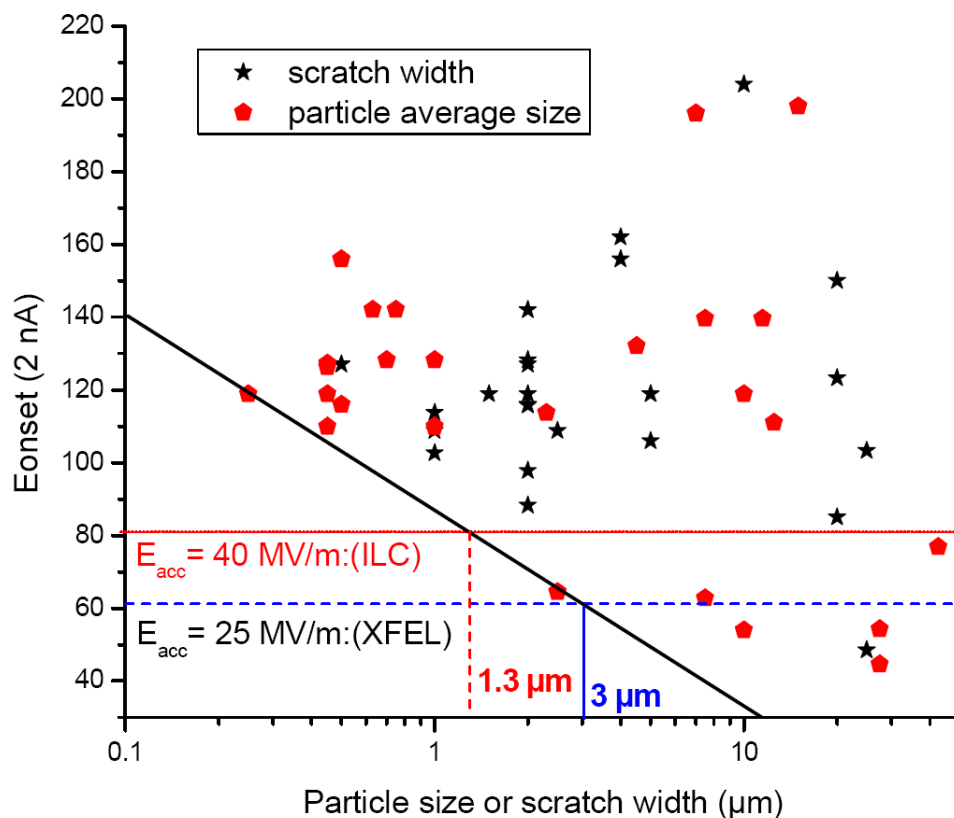


Fig. 7: Onset electric fields for 2 nA FE currents vs. geometrical size of all identified emitters found on various Nb samples during the last 3 years. The horizontal lines correspond to the proposed accelerating fields for future accelerators XFEL and ILC, and the diagonal line sets a corresponding threshold for tolerable defect sizes.

A huge spread in the emitter size is observed in the plot. The diagonal line, however, is referred as a threshold for the minimum emitter size and correspondingly achievable onset fields. Accordingly, to achieve an accelerating gradient of 30 (40) MV/m for XFEL (ILC) [7, 8], surface defects larger than 3 (1.3) μm must be avoided. This result will surely be useful for the quality control of superconducting structures during the assembly of large accelerator projects.

5.4. Conclusions

Single crystal and large grain Nb samples treated with BCP/HPR as a final surface preparation step have been found to show no FE up to surface electric fields of 150 MV/m. The onset fields were slightly higher for the samples with 100 μm removed damage layer than those with 30 μm , and also for single crystals compared to large grain samples due to reduced surface roughness. Heat treatment of large grain Nb sample at 150°C for 14 hours has given first evidence for grain boundary assisted field emission. Intrinsic FE measurements revealed anisotropic ϕ values of 4.02 and 3.8 for (111) and (100) orientations of Nb, respectively. From last three years EFE investigations on different Nb surfaces, a correlation between size of emitters and onset fields is obtained, which sets a threshold for the tolerable defect size to achieve the envisaged accelerating gradients in superconducting cavities reliably.

Acknowledgments

We would like to acknowledge C. S. Pandey from BUW for the support on the reinstallation of oven in FESM and thank the Electrical Engineering Department at BUW for access to SEM and EDX facilities. Stimulating discussions with W. Singer and D. Proch from DESY are appreciated. The support of the European Community Research Infrastructure Activity under FP6 ‘‘Structuring the European Research Area’’ program (CARE, contract number RII3-CT-2003-506395) is gratefully acknowledged.

References

- [1] <http://flash.desy.de>
- [2] <https://neutrons.ornl.gov/>
- [3] <http://www.ornl.gov/ria/>
- [4] G. Ciovati, Proc. of LINAC 2006, Knoxville, Tennessee USA
- [5] P. Kneisel and B. Lewis, Proc. of 7th Workshop on RF Superconductivity, Gif sur Yvette, France, ed. by B. Bonin, p. 311, (1995).
- [6] A. Dangwal, G. Müller, D. Reschke, K. Floettmann, and X. Singer, J.Appl. Phys. 102, 2007.
- [7] <http://xfel.desy.de>
- [8] <http://www.interactions.org/linearcollider>
- [9] P. Kneisel, G. R. Myneni, G. Ciovati, J. Sekutowicz, and T. Carneiro, Proc. 2005 Part. Acc. Conf., Knoxville, Tennessee, p3991.
- [10] G. Ciovati, P. Kneisel, and A. Gurevich, Phys. Rev. ST Accel. Beams 10, 062002 (2007).
- [11] D. Lysenkov and G. Müller, Int. J. Nanotechnol. 2, 239 (2005).
- [12] E. Mahner et al., Proc. 6th workshop on RF superconductivity, Newport News, Virginia (1993), p.1085.
- [13] P. Kneisel, Jefferson Lab, Newport News, VA 23606.
- [14] B. Visentin, Y. Gasser, and J.P. Charrier, 12th Workshop on RF Superconductivity, Ithaca USA (2005): TUP05.
- [15] R. H. Fowler and L. Nordheim, Proc. R. Soc. London A119, 173 (1928).
- [16] R. Pantel, M. Bujor, and J. Bardolle, Surf. Sci. 62, 589 (1977).
- [17] I. A. Podchernyaeva, G. V. Samsonov, and V. S. Fomenko, p721, translated from Izvestiya Vyssikh Uchebnykh Zavedenii, Fizika 12, pp. 42-47 (1969).
- [18] T. Habermann, PhD thesis, Univ. of Wuppertal (1999).
- [19] M. Jimenez, R. J. Noer, G. Jouve, J. Jodet, and B. Bonin, J. Phys. D: Appl. Phys.

Addendum to chapters 3, 4, and 5

In order to study the characteristic FE properties of an emitter observed in a FE map and to correlate its FE behaviour with its physical appearance, it has to be localized in FESM as well as in SEM. From SEM investigations, the localized emitters were mainly classified as either micro or nano particulates or surface irregularities. It was further investigated if the FN properties of these two classes of emitters also vary from each other. Some of our observations from FESM and SEM investigations are given in Fig. 1(a-d) and Fig. 2 (a-e).

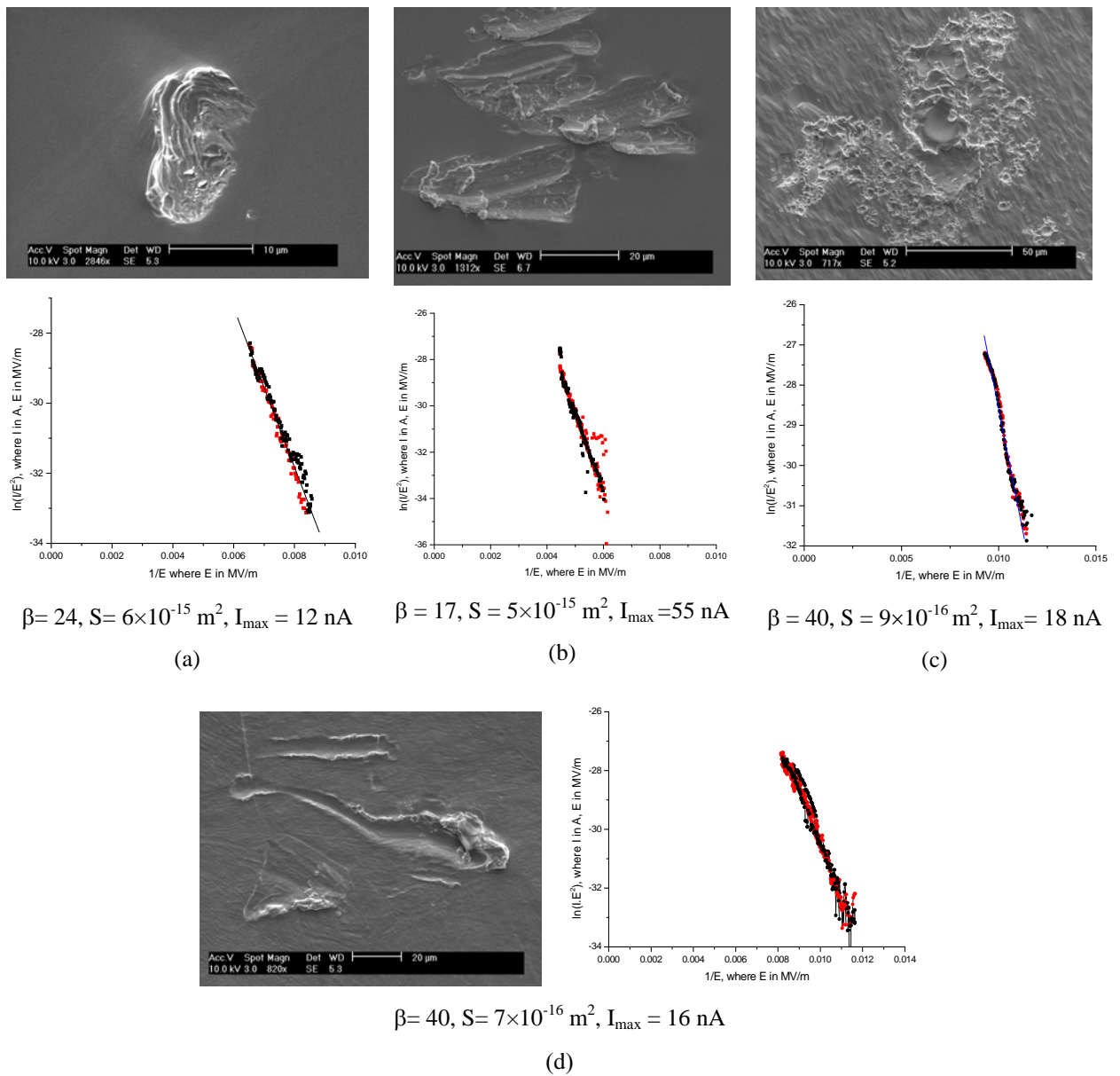


Fig. 1: SEM images and FN curves with fit parameters for various identified emitters as surface-irregularities (a – d).

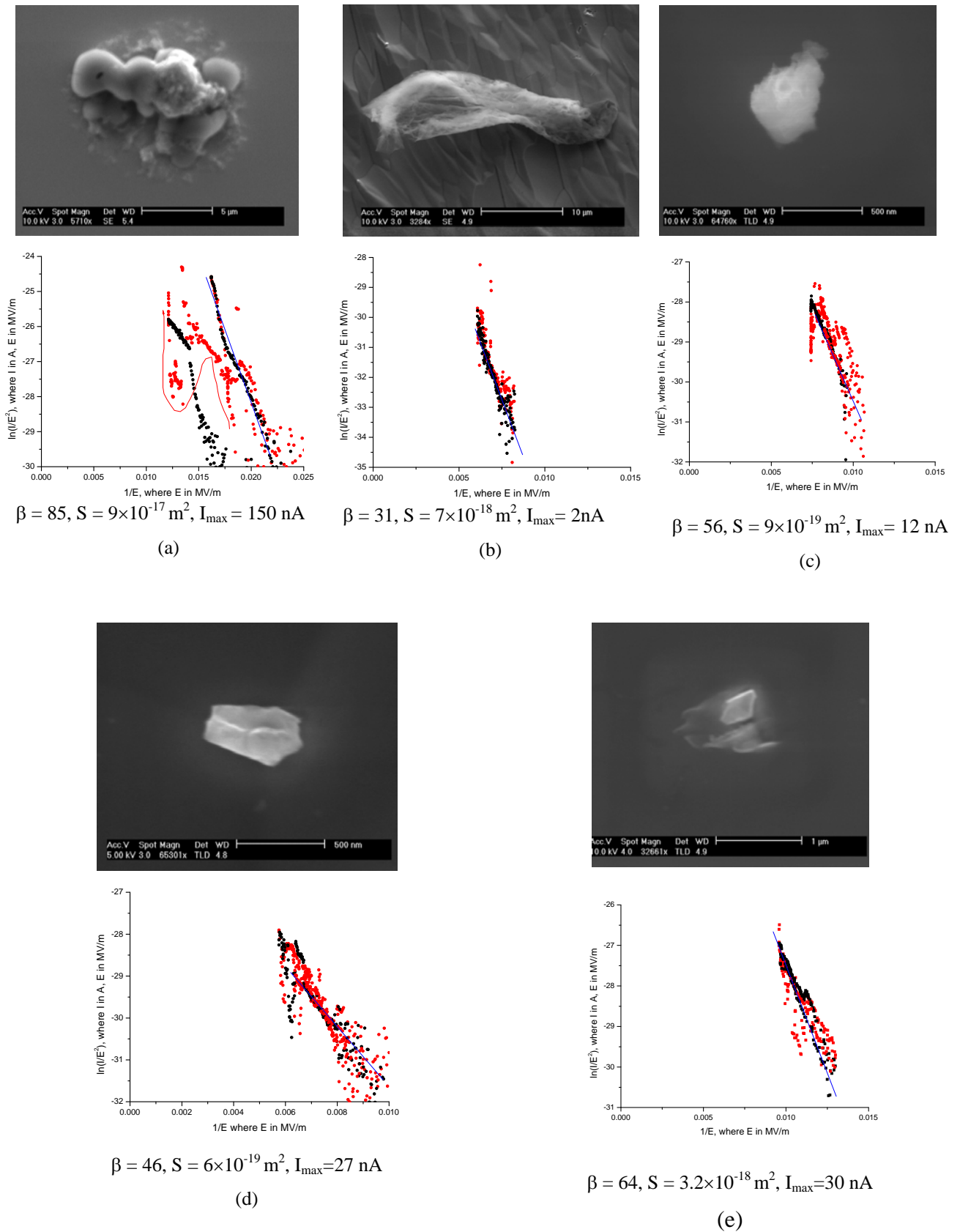


Fig. 2: SEM images and FN curves with fit parameters for various identified emitters as micro-particulates (a – e).

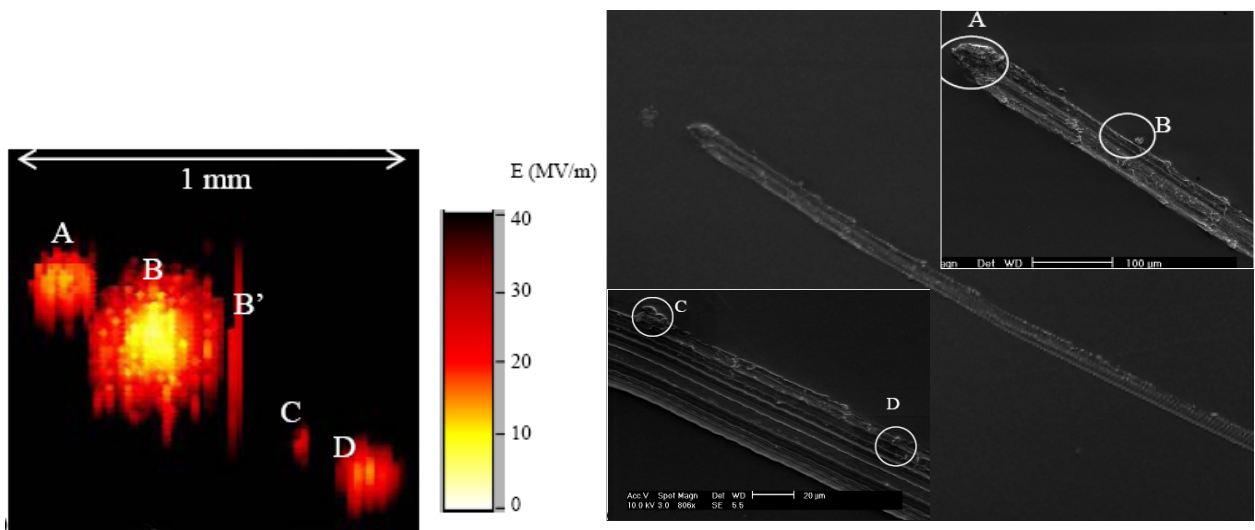


Fig. 3: High resolution E-map of the scratch using 30 μm anode (left) and SEM images of the corresponding emitting sites (right).

In general comparison, the I-V curves of particulates showed more instabilities than surface protrusions. Bad contact of emitters to the sample surface might account for this. To further confirm it, a scratch was intentionally made on a defect free surface of single crystal niobium sample inside FESM in UHV, and corresponding high resolution FE map was obtained (Fig. 3). The strongest emitter showed large fluctuations in local I-V measurement, which was not suppressed even by the emission current in μA range. This emitter was identified as a Nb microparticle, which was most probably produced during scratching of the sample and displaced near-by, and so can be assumed to be in a bad contact to the surface. Thus, the particulates being attached externally to the surface possess instability in their emission.

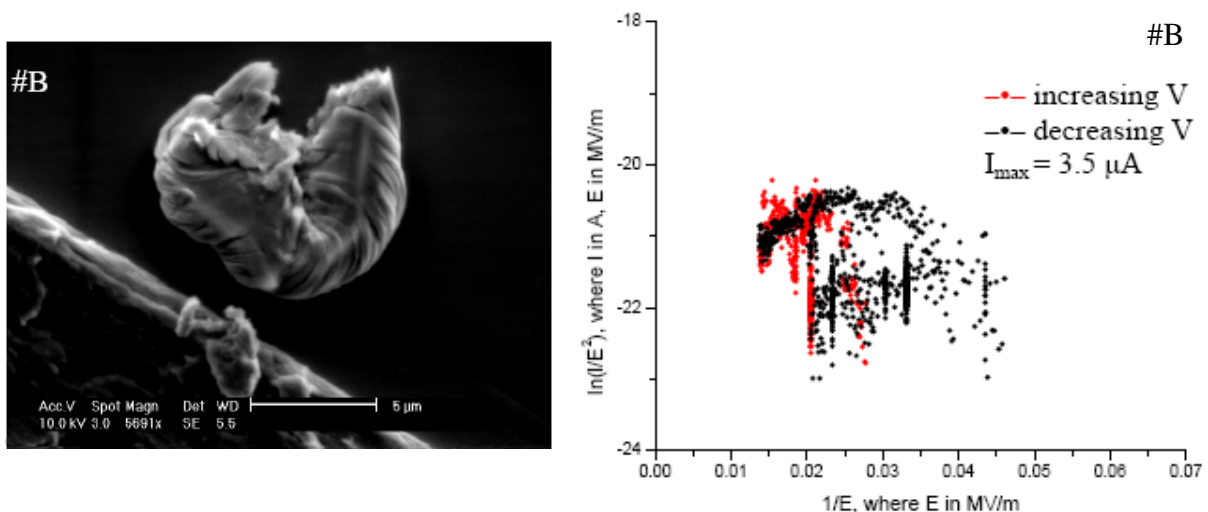


Fig. 4: Particle created by a freshly made scratch (left), and corresponding FN curve (right).

Impact of DIC on surface protrusions: microscopic results

As discussed in chapter 4, with the use of advanced cleaning techniques, the particle emitters can be removed efficiently from the metallic surface to suppress EFE, but it can not be true for already present surface irregularities like scratches. However, dry ice cleaning has shown very interesting results in this direction, as will be described now. Partial smoothing of surface irregularities has already been discussed in one case of a very small scratch (chapter 4: Fig. 12). This finding was further confirmed by next series of measurements on an intentionally made scratch (Fig 5: left) over a large grain Nb sample.

In FE maps, the scratch had shown up the field emission at 60 MV/m before DIC, while no emission up to 150 MV/m after DIC. So the cleaning effects were investigated by means of SEM. As clearly visible in the micrographs presented in Fig. 6 and 7, the smoothing of sharp features and removal of some delaminations has resulted by DIC. Thus, it evidences that DIC is able to largely suppress the EFE due to scratches, which is otherwise very difficult.

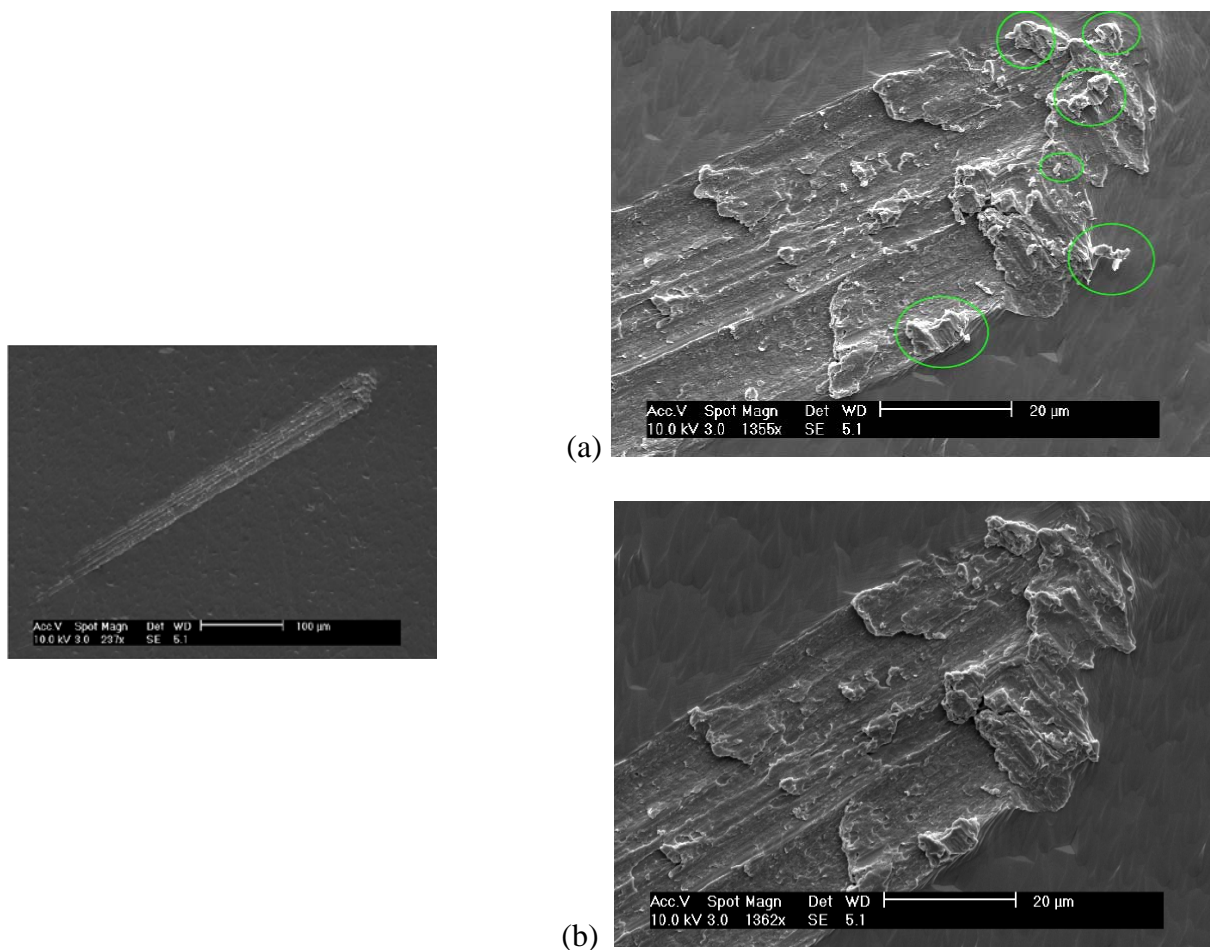


Fig. 5: Scanning micrographs of 500 μm long scratch (left), zoom view (right): (a) before DIC and (b) after DIC.

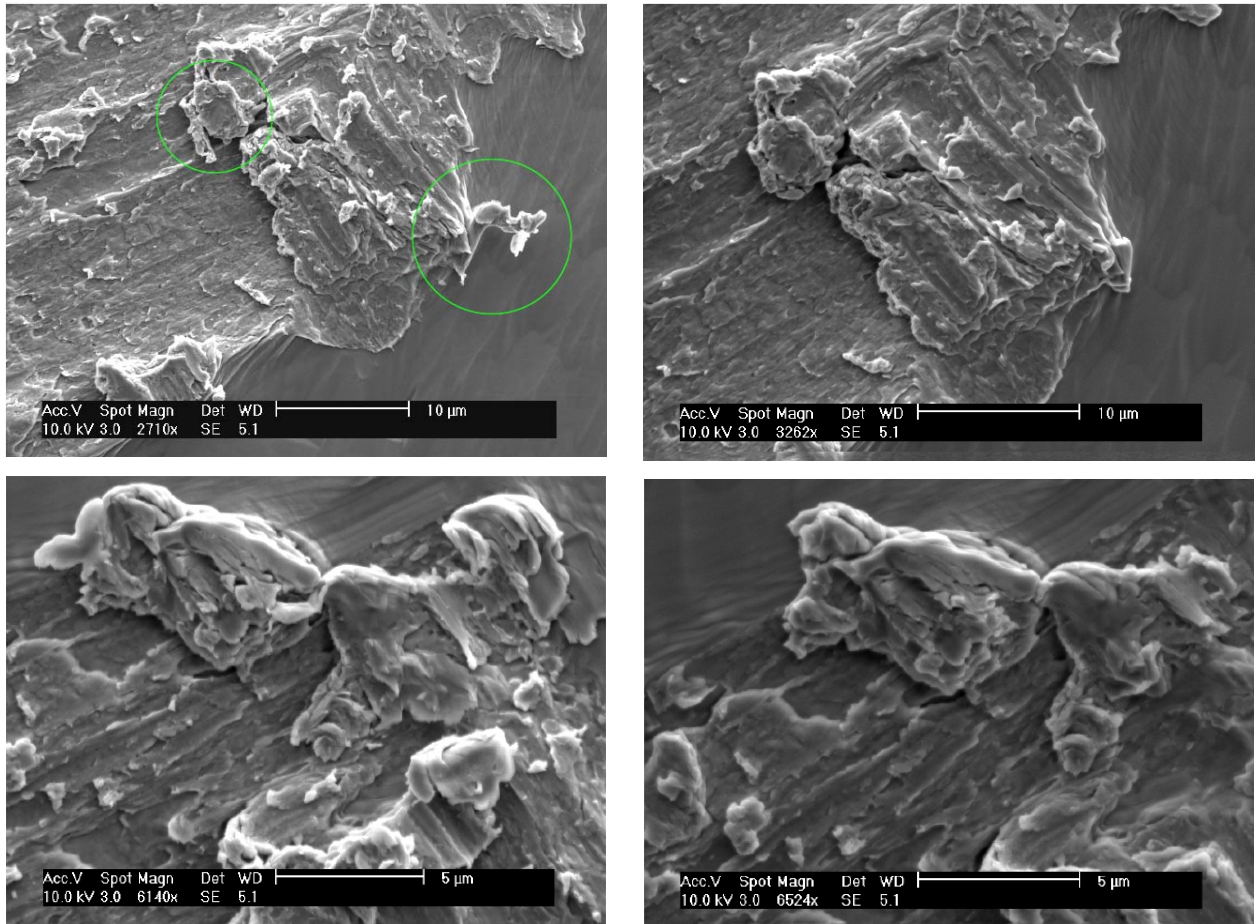


Fig. 6: SEM observations on the impact of DIC on the scratch sharp edge features and delaminations

The remaining scratch features still present after DIC produced no FE up to 150 MV/m. To find out the geometrical beta values of these features, atomic force microscopy was used. The obtained AFM scan (Fig. 7) showed that the sharpest feature present is of height (h) 1.6 μ m and the tip width (w) \sim 0.5 μ m, producing β of \sim 6.4, or less than 10, which according to FN theory will require the field \sim 300 MV/m for field emission on the clean Nb surface. It confirms our experimental observations.

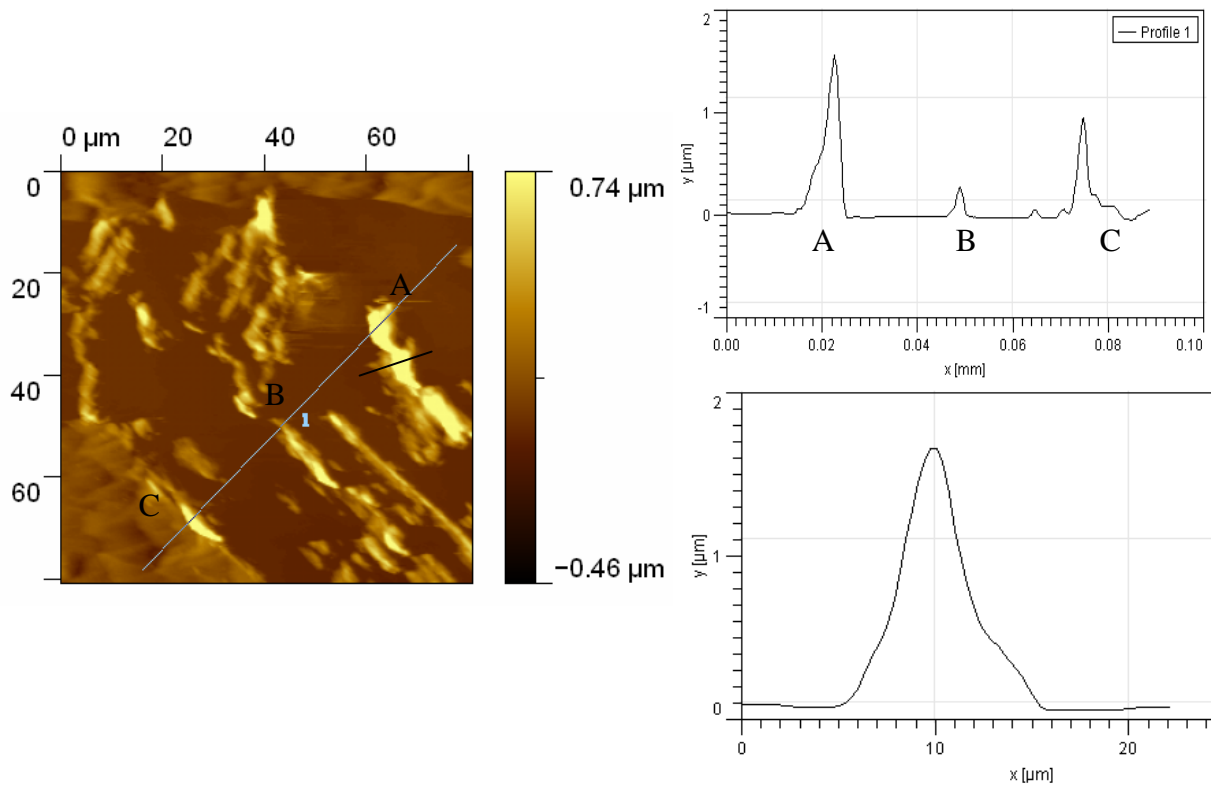


Fig. 7: (a) AFM over the scratch head after DIC, (b) profile of line ABC, and (c) Profile of the highest feature lying on black line.

Chapter 6

Field emission of copper nanowires grown in polymer ion-track membranes

*Florian Maurer, Arti Dangwal, Dmitry Lysenkov, Günter Müller,
Maria Eugenia Toimil-Molares, Christina Trautmann,
Joachim Brötz, Hartmut Fuess*

Nuclear Instruments and Methods in Physics Research B 245 (2006) 337–341

Abstract

Field emission properties of randomly distributed copper nanowires are presented. The wires were potentiostatically deposited into the pores of polycarbonate membranes produced by the ion-track etch technique. The diameter and length of the vertically aligned wires with number densities between 10^6 and 10^8 wires/cm² were in the range of 210–330 nm and 8–18 μm , respectively. By means of field emission scanning microscopy, emission site densities between $0.4 \times 10^5 \text{ cm}^{-2}$ and $1.4 \times 10^5 \text{ cm}^{-2}$ were obtained for nA currents at 6 V/lm. Two-thirds of the nanowire emitters showed Fowler–Nordheim behaviour with an average field enhancement factor of $\beta = 245$, which is about three times higher than expected for a cylindrical wire geometry with a half-sphere tip.

Keywords: Field emission; Copper; Nanowires; Heavy-ion irradiation; Ion-track etch technique; Polymeric membrane; Field emission scanning microscopy

6.1. Introduction

Quasi-one-dimensional nanostructures with high aspect ratio (length over diameter) such as nanowires, nanofibres or nanotubes are expected to provide extraordinary physical properties. At the tip of such an electrically conductive object an external applied electric field can be microscopically enhanced by several orders of magnitude [1–3]. Therefore, field electron emission (FE) by tunnelling through the surface potential occurs already at a few V/ μm . Since no elevated temperatures are required, such nanostructures could act as cold electron sources with many potential applications for vacuum nanoelectronics [4].

It is well known that the FE strength of randomly distributed nanostructures strongly depends on the mean distance between neighbouring emitters due to mutual electrostatic shielding [5,6]. The field enhancement factor β is influenced by the length and the diameter of the emitter, as was verified for single carbon nanotubes [7,8]. Compared to nanotubes, FE properties of metallic [9,10] and semiconducting [11] nanowires have been studied less systematically with respect to their geometry.

Ensembles of numerous (10^3 – 10^9cm^{-2}) metallic nanowires can be fabricated by electrochemical deposition of the respective matter into the hollow structures of a nanoporous template [12,13]. Two types of material are most common for templates: anodized aluminum-oxide (AAO) and polymeric ion-track membranes. Templates consisting of AAO contain hollow channels with uniform diameters typically between 4 and 300 nm [14]. The resulting channel density is in general very high (up to 10^{12}cm^{-2}) and the small interpore distance leads to screening effects between neighbouring emitters [15]. In contrast to AAO, the ion-track density in polymeric ion-track membranes can easily be varied over several orders of magnitude by adjusting the fluence of the heavy-ion beam. Subsequent to irradiation, the ion tracks are chemically etched into cylindrical pores. The diameter of the electrochemically deposited wires depends on the pore size which is controlled by the etching process, and the wire length is only limited by the thickness of the polymer membrane.

FE from cobalt nanowires grown in etched ion tracks was reported for a polymeric film template of a few microns spin-coated onto a solid metal substrate [16]. In our experiments, we used substrate-free commercial polymer foils as templates. Copper was chosen as material for deposition because of its well-known electrochemical properties [17] and its high electrical conductivity. It is also possible to grow single-crystalline Cu wires with distinct textures [18,19], which might improve the FE properties due to anisotropic work function, heat conductivity and reduced electron scattering on grain boundaries. First results

on the emitter number density, uniformity and FE strength of Cu nanowire samples will be presented.

Sample (see Fig. 2)	f (cm ⁻²)	$\langle a \rangle$ (μm)	d (nm)	h (μm)	Aspect ratio, h/r
(a)	$(0.76 \pm 0.2) \times 10^6$	5.7	323 ± 6	12.8 ± 0.1	80
(b)	$(1.7 \pm 0.1) \times 10^7$	1.2	210 ± 8	8 ± 1	76
(c)	$(2.0 \pm 0.2) \times 10^7$	1.1	331 ± 28	15 ± 1	90
(d)	$(1.1 \pm 0.1) \times 10^8$	0.5	213 ± 9	18 ± 2	170

Table 1: Geometrical parameters of different copper nanowire samples: Fluence f , mean spacing to nearest neighbour $\langle a \rangle$, diameter $d = 2r$, height h , and aspect ratio

6.2. Experimental

Polycarbonate foils (MAKROFOL N, Bayer Leverkusen) of 30 μm thickness were irradiated with ²³⁸U ions of energy of 11.1 MeV/nucleon with fluences varying from 10⁴ to 10⁹ cm⁻². Prior to the chemical track etching, all samples were exposed to UV light to enhance the etching rate along the tracks [20] and thus favour the formation of cylindrically shaped pores. Etching was performed at 50 °C in a 6 M NaOH solution between 5 and 10 min. A ~100 nm gold film was sputtered onto one side of the membrane to establish a conductive substrate for wire growth. The gold layer was mechanically strengthened by electrode-position of ~10 μm copper, using a commercial electrolyte solution (Cupatierbad, Riedel Company). The potentiostatic deposition of copper into the etched pores of the template was accomplished at 50 °C with an electrolyte solution of 238 g/l CuSO₄ · 5H₂O and 21 g/l H₂SO₄. The voltage applied was kept constant during wire growth but varied for different samples between -70 and -110 mV. The wires were separated from the template by dissolving the polymer in CH₂Cl₂.

The FE performance of the nanowire cathodes was first tested in diode configuration with a luminescent screen under high vacuum conditions (10⁻⁴ Pa) which resulted in rather unstable emission from a few emitters only at the edges of the samples. Therefore, more detailed FE measurements were performed with a field emission scanning microscope (FESM) under ultra-high vacuum conditions (<10⁻⁷ Pa) [21]. By means of 3D stepper motors and piezo translators, this automated instrument reveals the FE current distribution for a given voltage as well as FE properties of individual emitters with μm resolution [22].

6.3. Results and Discussion

The mean spacing $\langle a \rangle$ between the pores of the templates was analyzed by means of scanning electron microscopy (SEM) and software image processing (see inset of Fig. 1). Fig. 1 shows the variation of $\langle a \rangle$ with irradiation fluence f . Assuming a Poisson distribution of the ion tracks [23–25], the mean spacing $\langle a \rangle$ depends on the fluence f by

$$\langle a \rangle = \frac{1}{2\sqrt{f}} \quad \dots (1)$$

The experimental data shown in Fig. 1 are in excellent agreement with Eq. (1). Therefore, the spacing of the pores and nanowires $\langle a \rangle$ can be adjusted in a large regime from 50 μm to 0.1 μm by selecting a suitable irradiation fluence.

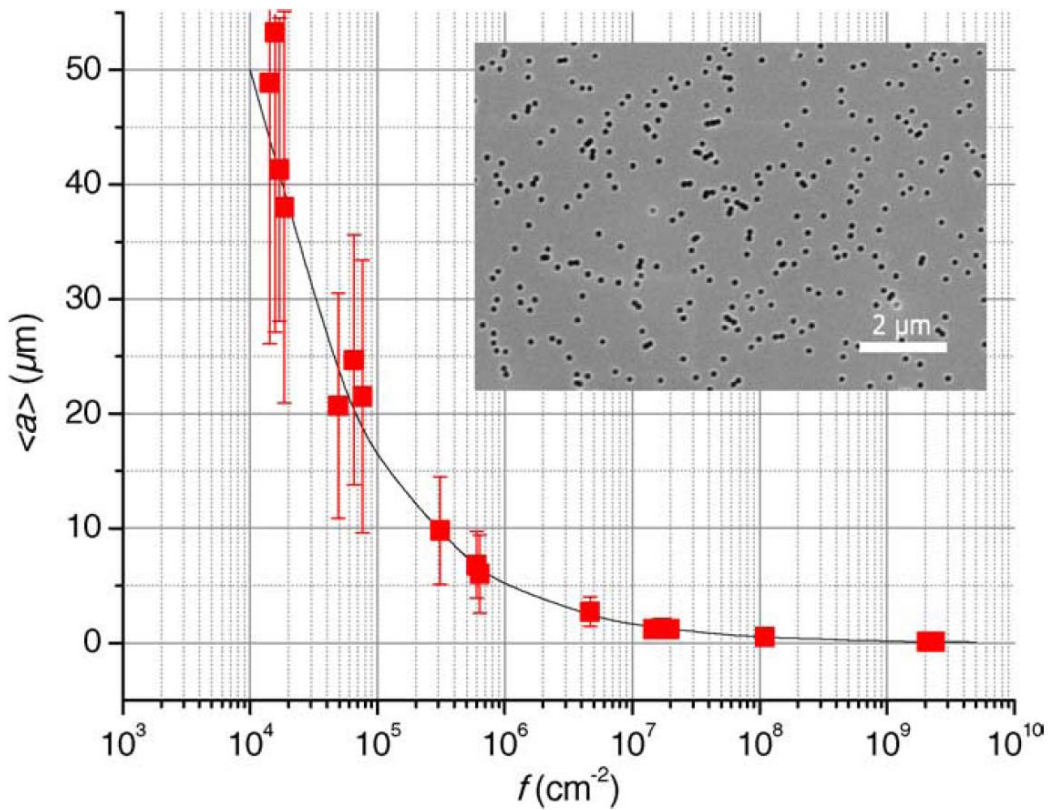


Fig. 1: Mean spacing $\langle a \rangle$ of randomly distributed pores in polycarbonate membranes as a function of the irradiation fluence f . The solid line corresponds to Eq. (1), assuming Poisson-distributed pores. Inset: SEM image of an etched ion-track template with $f = 3.7 \cdot 10^8 \text{ cm}^{-2}$, $\langle a \rangle = 0.26 \mu\text{m}$, and $d = 130 \text{ nm}$.

To produce wires of a certain length, the deposition process was interrupted when the wires reached a predefined value. By integrating the deposition current over the deposition time (online coulometry), the length of the wires was deduced, as the length of the wires is directly proportional to the deposited charge q . The growth process was immediately stopped when a predefined charge value was approached, corresponding to a certain wire length.

SEM images of four different copper wire ensembles are shown in Fig. 2(a)–(d). All wires of a given ensemble have cylindrical shape and a uniform aspect ratio, indicating a homogeneous etching and deposition process over a large area. Geometrical parameters of the different ensembles are given in Table 1. Following Eq. (1), the mean spacing between the 10^7 cm^{-2} wires in Fig. 2(b) and (c) is about $1.1 \mu\text{m}$. Because the wire density of the

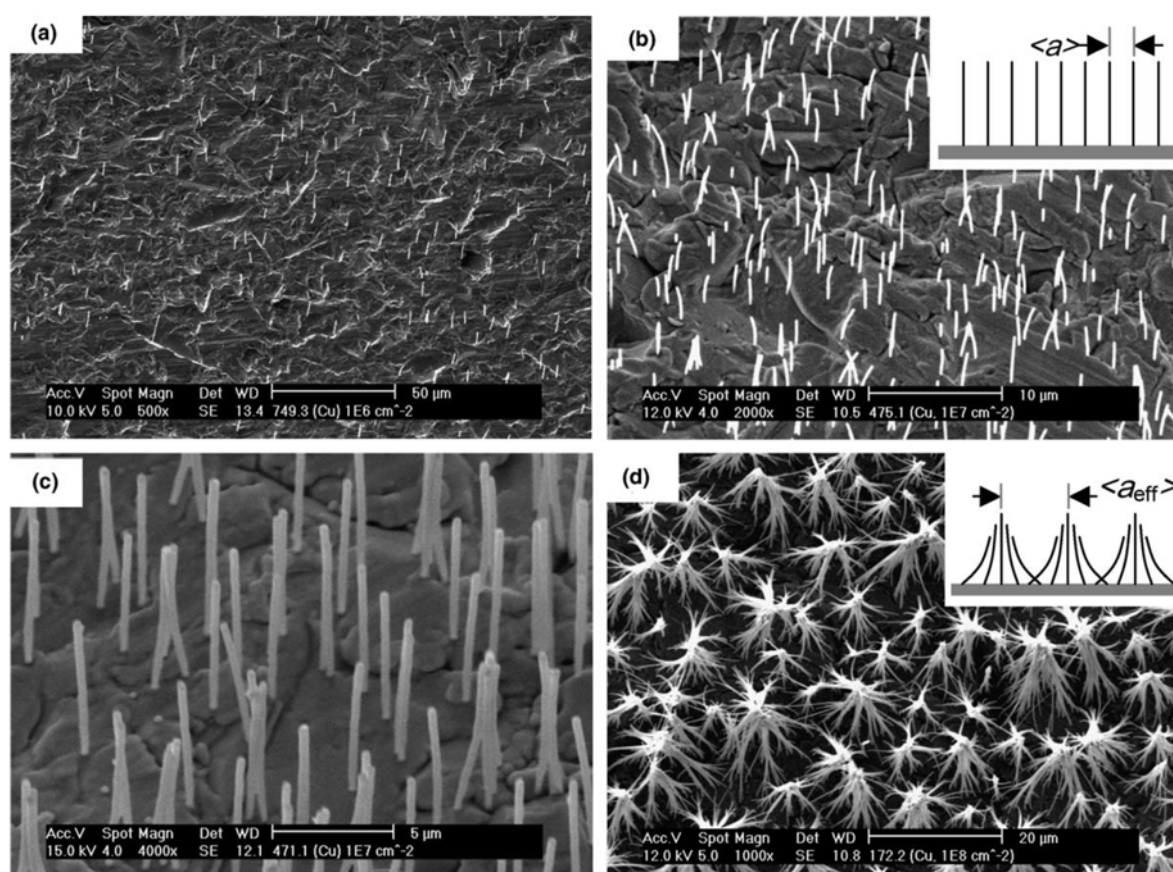


Fig. 2: SEM images of free-standing copper nanowires on Au/Cu backing layers with different spacings $\langle a \rangle$ and number densities N : (a) $\langle a \rangle \approx 10 \mu\text{m}$, $N \approx 10^6 \text{ cm}^{-2}$, (b) $\langle a \rangle \approx 1 \mu\text{m}$, $N \approx 10^7 \text{ cm}^{-2}$, (c) $\langle a \rangle \approx 1 \mu\text{m}$, $N \approx 10^7 \text{ cm}^{-2}$, with about double the wire length of sample (b), and (d) $\langle a \rangle \approx 0.5 \mu\text{m}$, $N \approx 10^8 \text{ cm}^{-2}$, single wires agglomerated to star-shaped wire bundles ($\approx 10^6 \text{ cm}^{-2}$); the agglomeration of the nanowires leads to a larger spacing $\langle a_{\text{eff}} \rangle$ between bundle centres compared to the parallel-aligned single wires.

sample in Fig. 2(d) is one order of magnitude higher (10^8 cm^{-2}), the mean spacing decreases to $0.5 \text{ }\mu\text{m}$ and leads to agglomerations of the wire tips (Fig. 2(d)). The formation of these star-shaped structures probably occurs by bending (facilitated due to their high aspect ratio) of the free-standing wires during or after dissolution of the polymeric template. As compared to Fig. 2(c), the nanowires in Fig. 2(b) have the same spacing but a shorter length. The nanowire sample with the lowest fluence ($7.6 \times 10^6 \text{ cm}^{-2}$) in Fig. 2(a) provides a much larger spacing for a similar aspect ratio.

According to the modified Fowler–Nordheim (FN) theory, the current density J from a tip-like emitter with a microscopically enhanced electric field βE is given by

$$J = \frac{A(\beta E)^2}{\phi} \exp\left(-\frac{B\phi^{1.5}}{\beta E}\right), \quad \dots (2)$$

where ϕ is the work function of the emitting material (4.5 eV for Cu). In the terms $A = 1.54 \times 10^{-10} \text{ AeV/V}^2$ and $B = 6.83 \times 10^9 \text{ V/m eV}^{1.5}$ several fundamental constants are summarized. For cylindrical emitters with a half-sphere tip, the field enhancement factor is mainly given by the height over radius aspect ratio h/r [3]:

$$\beta_{geo} = \frac{h}{r} + 2. \quad \dots (3)$$

In diode configuration, the FE properties of the Cu nanowire samples were dominated by a few emitters at the sample edges yielding integral currents up to some hundred nA at electric fields of $5\text{--}10 \text{ V}/\mu\text{m}$. Fowler-Nordheim-like $I\text{--}V$ curves with field enhancement factors $\beta = 380$ (Fig. 2(b)), 485 (Fig. 2(c)) and 800 (Fig. 2(d)) were obtained which are about a factor of 5 larger than expected from the aspect ratio, partially due to edge effects. A rather unstable maximum current around $1 \mu\text{A}$ at $6 \text{ V}/\mu\text{m}$ was obtained from about 15 emitters on sample (d).

In order to determine the intrinsic FE properties of the Cu nanowires, we performed both voltage and current scans on two nanowire samples by means of FESM. The voltage scans for 1 nA reveal the number of emitters N_e as function of the electric field. We have found 16 ($212, 1732$) emitters/ mm^2 up to 4.3 ($5.5, 8.5$) $\text{V}/\mu\text{m}$ on sample (d), and 4 ($10, 42, 76$) emitters/ mm^2 up to 6 ($9, 12, 15$) $\text{V}/\mu\text{m}$ on sample (a), respectively. The current maps in Fig. 3 confirm the higher $N_e = 1.4 \times 10^5 \text{ cm}^{-2}$ on sample (d) as compared to $N_e = 4.4 \times 10^4 \text{ cm}^{-2}$ for sample (a), both at fields around $6 \text{ V}/\mu\text{m}$. It is remarkable that compared to the wire

density only about 0.13% (sample (d)) and 6% (sample (a)) of all wires contribute to the FE. Obviously, the percentage for sample (d) (see Fig. 2(d)) must be corrected due to the

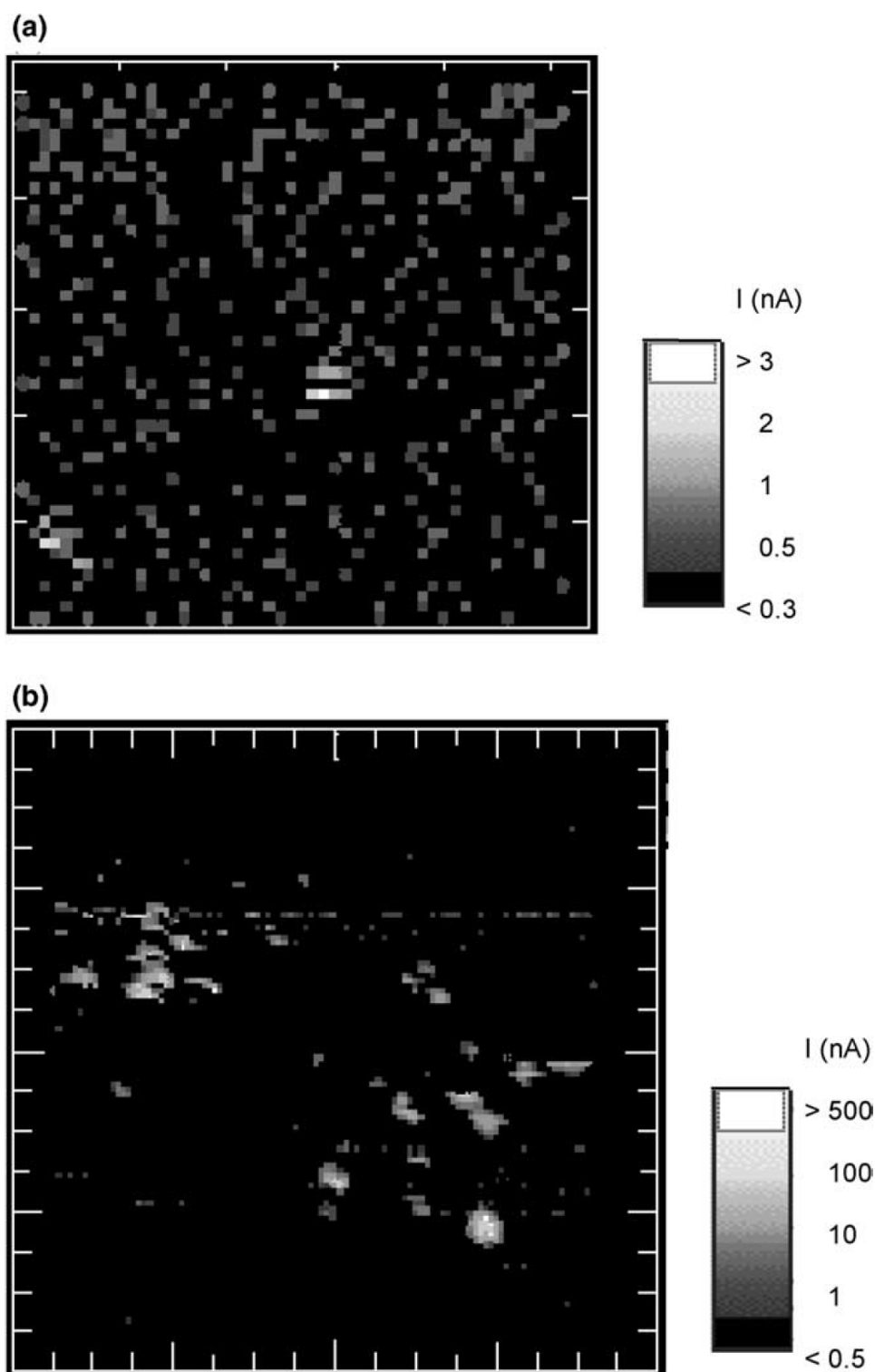


Fig. 3: Current distribution maps of Cu nanowire samples (scanned area $0.5 \times 0.5 \text{ mm}^2$) obtained with FESM for (a) sample in Fig. 2(d) with $\sim 1.4 \times 10^5$ emitters/ cm^2 at $6.4 \text{ V}/\mu\text{m}$ and (b) sample in Fig. 2(a) with $\sim 4.4 \times 10^4$ emitters/ cm^2 at $5.7 \text{ V}/\mu\text{m}$.

agglomeration of several hundred wires into a bundle which also seem to act as emitter. Unfortunately, the emission of both types of samples is still not very uniform despite of similar length and diameter of the nanowires. Therefore, we performed local FESM measurements on 20 randomly chosen emitters of sample (a) by a cycle of ascending (\uparrow) and descending (\downarrow) voltages.

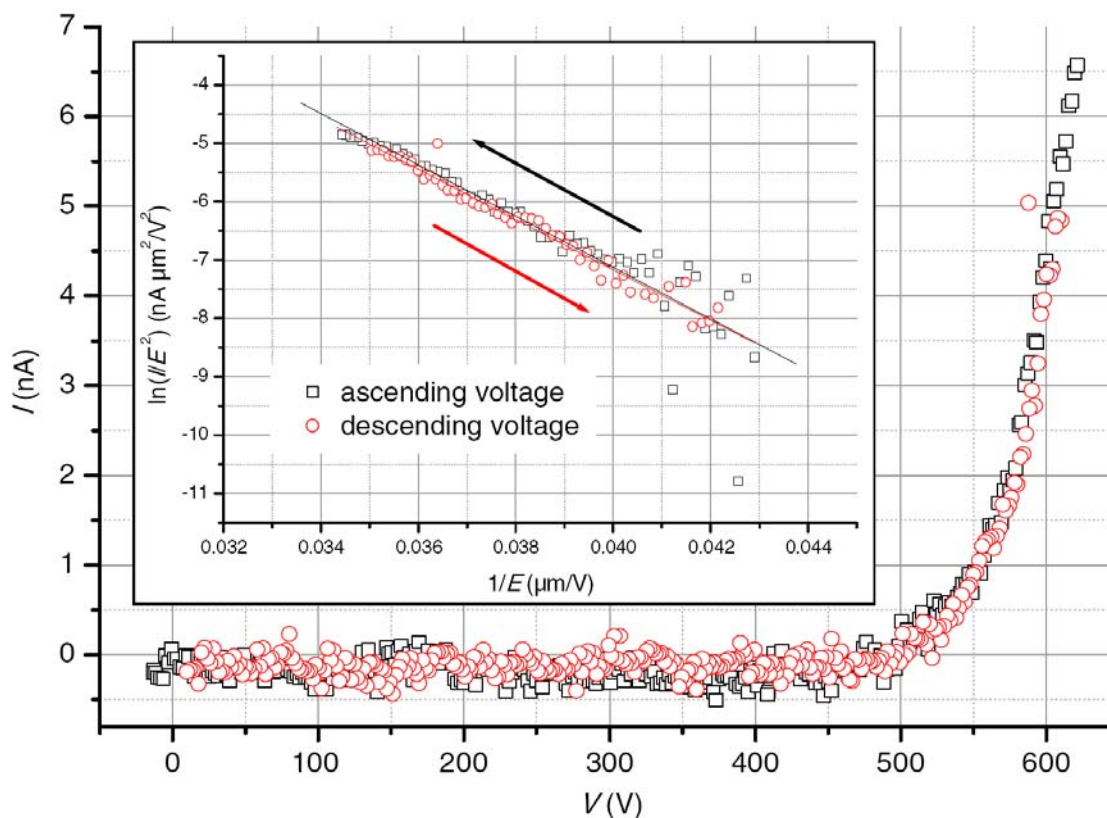


Fig. 4: I - V curve and FN plot (inset) of Cu nanowires with stable emission i.e. similar β values for ascending ($\beta_{\uparrow} = 145$) and descending ($\beta_{\downarrow} = 153$) I - V curves.

Most of the I - V curves show activation (enhanced β values at the descending cycle) or deactivation (lowered β values at the descending cycle) effects, but rarely stable FN behaviour as shown in Fig. 4. The β values extracted from all of these I - V curves can be fitted by a Gaussian distribution as shown in Fig. 5, resulting in a mean value of 245 which is about a factor of three higher than expected from the aspect ratio (Eq. (3)). This discrepancy as well as the observed inhomogeneity might be explained by the assumption that the real tip shape of the nanowires is possibly sharper than a half-sphere with pore diameter as assumed for the calculation of the β values [26].

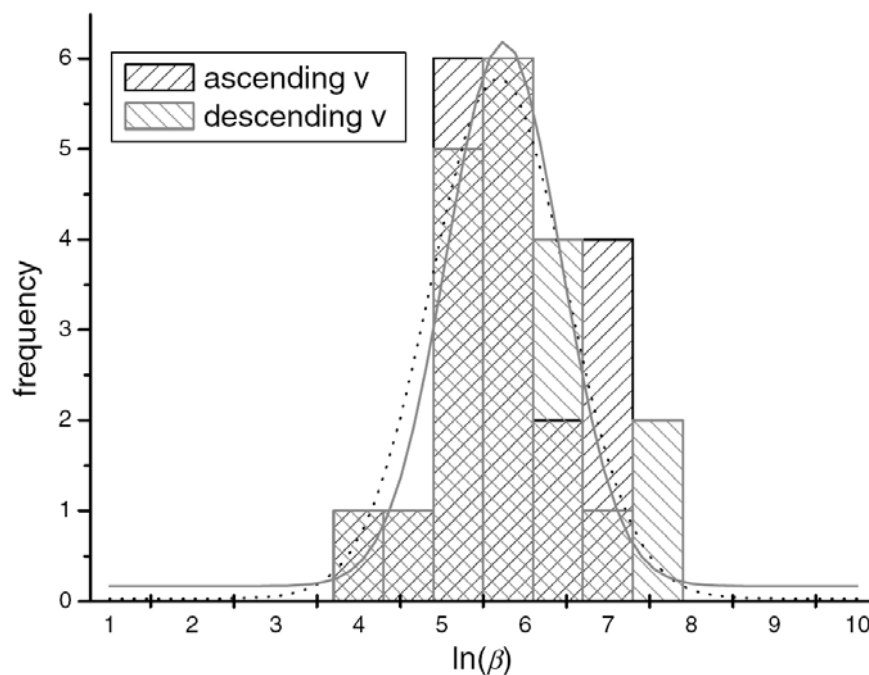


Fig. 5: Histogram and fitted Gaussian distributions (dotted line: ascending voltage, solid line: descending voltage) of β values obtained for 20 emission sites from FN curves which are slightly different for increasing and decreasing voltages. The β mean value is about 245.

6.4. Conclusions

Integral and local field-emission investigations were accomplished on ensembles with different geometrical properties, obtaining emission site densities up to $1.4 \times 10^5 \text{ cm}^{-2}$ at $6 \text{ V}/\mu\text{m}$. Only 6% of free-standing and vertically aligned nanowires were strong emitters. Nearly all wires showed unstable FN behaviour (different β values for ascending and descending voltage cycle) with a mean β value of 245, which is a factor three higher than expected from the emitter shape, possibly due to the influence of the tip geometry. For nanowires of $18\mu\text{m}$ length and submicron spacing, several hundred nanowires agglomerated into bundles, which also showed field emission. Further investigations of the influence of different emitter tip geometries on the field emission properties of different nanowire ensembles (emitter densities and aspect ratios) are in progress in order to find the most suitable parameters for field emission.

References

- [1] I. Brodie, *J. Appl. Phys.* 35 (1964) 2324.
- [2] R.V. Latham, *High Voltage Vacuum Insulation: The Physical Basis*, Plenum, London, 1981.
- [3] T. Utsumi, *IEEE Trans. Electron Dev.* 38 (1991) 2276.
- [4] N.S. Xu, S. Ejaz Huq, *Mater. Sci. Eng. R* 48 (2005) 47.
- [5] L. Nilsson, O. Groening, C. Emmenegger, O. Kuettel, E. Schaller, L. Schlappach, H. Kind, J.-M. Bonard, K. Kern, *Appl. Phys. Lett.* 76 (2000) 2071.
- [6] K.B.K. Teo, M. Chhowalla, G.A.J. Amaratunga, W.I. Milne, G. Pirio, P. Legagneux, F. Wyczisk, D. Pribat, D.G. Hasko, *Appl. Phys. Lett.* 80 (2002) 2011.
- [7] J.-M. Bonard, N. Weiss, H. Kind, T. Stöckli, L. Forro, K. Kern, A. Chatelain, *Adv. Mater.* 13 (2001) 184.
- [8] J.-M. Bonard, K.A. Dean, B.F. Coll, C. Klinke, *Phys. Rev. Lett.* 89 (2002) 197602.
- [9] D.N. Davydov, P.A. Sattari, D. AlMawlawi, A. Osika, T.L. Haslett, M. Moskovits, *J. Appl. Phys.* 86 (1999) 3983.
- [10] G.-M. Zhang, E. Roy, H.-W. Liu, W.-M. Liu, S.-M. Hou, K. Yu Zhang, Z.-Q. Xue, *Chin. Phys. Lett.* 19 (2000) 1016.
- [11] F.C.K. Au, K.W. Wong, Y.H. Tang, Y.F. Zhang, I. Bello, S.T. Lee, *Appl. Phys. Lett.* 75 (1999) 1700.
- [12] C.R. Martin, *Science* 266 (1994) 1961.
- [13] A. Huczko, *Appl. Phys. A* 70 (2000) 365.
- [14] J.S. Suh, K.S. Jeong, J.S. Lee, I. Han, *Appl. Phys. Lett.* 80 (2002) 2392.
- [15] J.J. Schneider, J. Engstler, S. Franzka, K. Hofmann, B. Albert, J. Ensling, P. Gütllich, P. Hildebrandt, S. Döpner, W. Pflöging, B. Günther, G. Müller, *Chem. Eur. J.* 7 (2001) 2888.
- [16] L. Vila, P. Vincent, L. Dauginet-De Pra, G. Pirio, E. Minoux, L. Gangloff, S. Demoustier-Champagne, N. Sarazin, E. Ferain, R. Legras, L. Piraux, P. Legagneux, *Nano Lett.* 4 (2004) 521.
- [17] I.U. Schuchert, M.E. Toimil-Molares, D. Dobrev, J. Vetter, R. Neumann, M. Martin, *J. Electrochem. Soc.* 150 (2003) C189.
- [18] M.E. Toimil-Molares, V. Buschmann, D. Dobrev, R. Neumann, R. Scholz, I.U. Schuchert, J. Vetter, *Adv. Mater.* 13 (2001) 62.
- [19] D. Dobrev, J. Vetter, N. Angert, R. Neumann, *Appl. Phys. A* 72 (2001) 729.
- [20] W. DeSorbo, *Nucl. Tracks* 3 (1979) 13.

-
- [21] E. Mahner, N. Minatti, H. Piel, N. Pupeter, *Appl. Surf. Sci.* 67 (1993) 23.
- [22] D. Lysenkov, G. Müller, *Int. J. Nanotechnol.* 2 (2005) 239.
- [23] C. Riedel, R. Spohr, *Radiat. Effects* 42 (1979) 69.
- [24] R. Spohr, *Ion Tracks and Microtechnology – Principles and Applications*, Vieweg, Braunschweig, 1990.
- [25] B.S. Barashenkov, *JINR P 14* (1977) (German translation).
- [26] T. Habermann, A. Göhl, G. Müller, N. Pupeter, H. Piel, in: S. Myers et al. (Eds.), *Proc. V Europ. Part. Acc. Conf., Sitges, IoP Bristol*, 1996, p. 2082.

Chapter 7

Field emission properties of bare and gold-coated nickel nanowires grown in polymer ion-track membranes

A. Dangwal, G. Müller, F. Maurer, J. Brötz, and H. Fuess

Journal of Vacuum Science and Technology B 25, 2, Mar/Apr 2007

Abstract

The authors have measured the field emission properties of freestanding bare and Au-coated Ni nanowires randomly distributed on thin metallic substrates. The nanowires of uniform length and diameter were grown in the etched ion-tracked pores of polycarbonate membranes by electrochemical deposition. While bare Ni samples yielded only 1.6×10^4 emitters/cm² at 10 V/μm, Au coating of the Ni nanowires improved the emission site density to 1.4×10^5 /cm² at 5 V/μm and about 1.6×10^6 emitters/cm² at 18 V/μm. Average field enhancement factors β of 331 for bare Ni and 302 for Au-coated Ni nanowires correspond well to their cylindrical shape in the scanning electron microscope images. Stable Fowler-Nordheim-like emission was obtained on average up to currents of about 0.4 and 8 μA for bare and Au-coated Ni nanowires, respectively. Locally measured I-V curves, maximum current I_{\max} , and derived β values hint for the clustering of nanowires.

7.1. Introduction

Besides carbon nanotubes metallic nanowires are one of the most attractive materials or electron field emission (FE) cathodes because of their quasi-one-dimensional structure and high electron conductivity. [1] Due to their small diameters in the nanometer range and large lengths in the micrometer range, they provide high aspect ratios which generate large electric field enhancements for FE at low operation voltages, required for the application, e.g., in FE flat panel displays. Metallic nanowires are also interesting because they can be readily fabricated by various techniques. [2] An important fabrication technique is the template assisted deposition, i.e., filling of uniform nanopores with a material of choice resulting in arrays of nanowires with uniform shape.

Electrodeposition in ion-track membranes has been used successfully to create large two-dimensional arrays of nano wires and tubes of different metals. [3–7] Etched ion-track membranes used as template provide random distribution of uniform and well-aligned pores with number densities from $10^0/\text{cm}^2$ [8] up to $10^9/\text{cm}^2$ [9] depending on the ion fluence. The FE strength of cathodes with randomly distributed nanostructures, however, is affected by a field screening effect, which depends strongly on the height and mean distance of neighboring emitters. [10] Therefore, the FE performance of such nanowire cathodes will depend on several parameters, especially the ion irradiation fluence and the choice of metal.

In this article we present the FE properties of the Ni nanowire samples electrolytically grown into the pores of etched ion-track membranes. It will be shown that coating of Ni nanowires with sputtered Au films leads to improved emitter performance due to reduced oxidation. Finally these results will be compared with those of Cu nanowires fabricated by the same technique.

7.2. Experimental techniques

The fabrication method of Ni nanowires consists of several steps, as shown in Fig. 1. At first, 30 μm thick polycarbonate foils (Makrofol N, Bayer Leverkusen) were irradiated with ^{238}U ions of energy of 11.1 MeV/nucleon with a fluence of $1.75 \times 10^7/\text{cm}^2$. Each ion interacts with the target electrons and creates a cylindrical damage zone along its trajectory which is further developed by UV light exposure. [11] Subsequent selective etching of the damaged material in 6M NaOH solution at 50 ° C leads to the formation of cylindrically shaped nanopores. The back side of this template has been coated first with a thin gold film (~100 nm) by sputtering and then with a thick Cu layer (~10 μm) by electrochemical

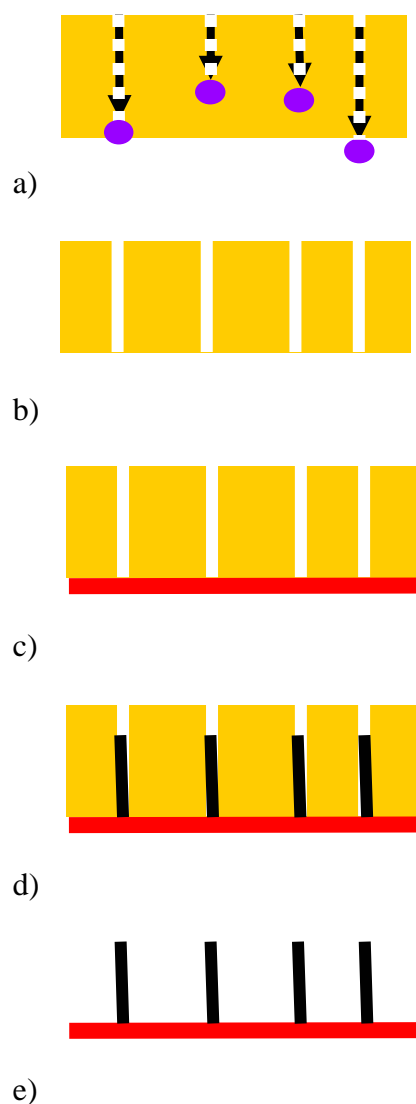


Fig.1: Schematic of the Ni nanowire fabrication: a) Irradiation of polycarbonate foil with heavy ions; b) Chemical etching of ion tracks; c) Electrochemical deposition of Cu backing layer; d) Filling of pores with Ni by electrodeposition; e) Free-standing Ni nanowires of uniform length after dissolution of polycarbonate template.

deposition. This backing layer serves as cathode and substrate for the nickel nanowire deposition which has been potentiostatically performed under alternating current conditions from a nickel Watts electrolyte solution (300 g / l $\text{NiSO}_4 \cdot 6\text{H}_2\text{O}$, 50 g / l $\text{NiCl}_2 \cdot 6\text{H}_2\text{O}$, and 40 g / l H_3BO_3) into the pores of the template at 50 °C. Finally, the polymer foil has been dissolved in CH_2Cl_2 resulting in freestanding nanowires. The whole array was subsequently cut into several pieces and one fraction was covered with a thin gold film (10 nm) to prevent corrosion.

The emission site density and current distribution of the metallic nanowire cathodes were measured with a field emission scanning microscope (FESM) under ultrahigh vacuum conditions. [12] The samples were positioned and tilt corrected with respect to the tungsten

tip anodes by means of three-dimensional stepper motors and piezotranslators, resulting in scans of 1 cm^2 area at constant electrode spacing within $\pm 1 \mu\text{m}$. The potential emission site density up to the given maximum field level has been measured nondestructively by proportional-integral-derivative-regulated voltage maps for constant currents, while the subsequent current distribution maps at constant voltage have revealed the real activated number density of emitters at a fixed electric field. Finally, local measurements of the FE properties of the nanowire samples were performed at randomly chosen emitting sites.

7.3. Results and Discussion

The typical morphology of the Au-coated Ni nanowires is shown on a scanning electron microscope (SEM) image in Fig. 2. Most of the cylindrical wires are well aligned but some have fallen down or clustered to bundles during the dissolution of the polymer foil. Statistical analysis of the wire dimensions yields a mean diameter of $132 \pm 14 \text{ nm}$, length of $9.5 \pm 0.5 \mu\text{m}$, and number density of about $10^7 / \text{cm}^2$. The acquisition of high resolution SEM images of bare Ni nanowires turned out to be very difficult due to charging effects. Considering the thickness of the Au film, the resulting aspect ratios for the bare and Au-coated Ni nanowires are 170 and 144, respectively.

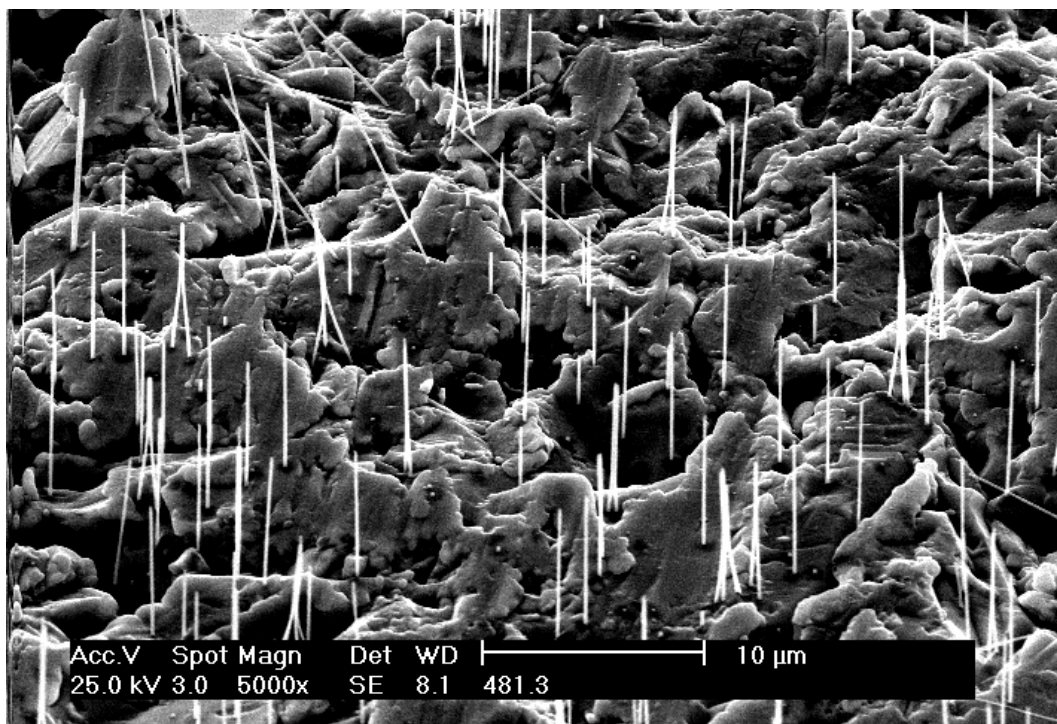


Fig.2: SEM image of Au-coated Ni nanowires.

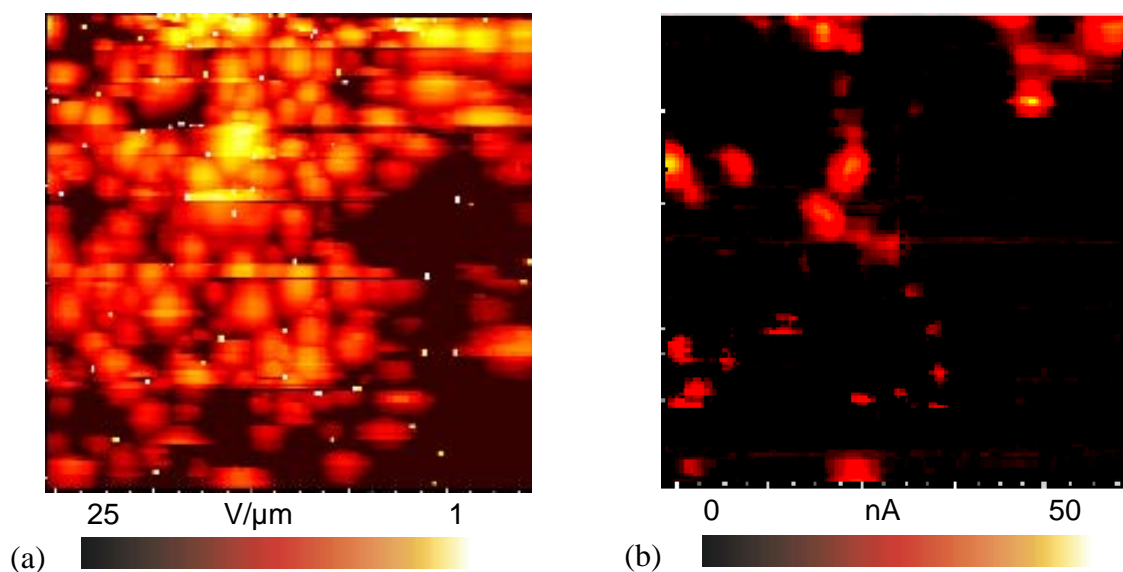


Fig.3: (a) Onset field map for 2 nA current and (b) current map (scanned areas $500 \times 500 \mu\text{m}^2$, anode diameter $\varnothing_A = 5 \mu\text{m}$, for more experimental details see ref. 12) of the bare Ni nanowire cathode showing a maximum of 1.5×10^5 emitters/ cm^2 at $25 \text{ V}/\mu\text{m}$ and 1.6×10^4 emitters/ cm^2 at $10 \text{ V}/\mu\text{m}$, respectively. Please ignore the small white spots in (a) which are an experimental artefact.

The emission site distribution on bare and Au-coated Ni nanowire samples is shown in Figs. 3 and 4, respectively. Obviously the number density of emitters N_e for bare Ni nanowires is much smaller than for Au-coated Ni nanowires. While the onset field map (as determined from the regulated voltage map divided by the electrode spacing) for bare Ni

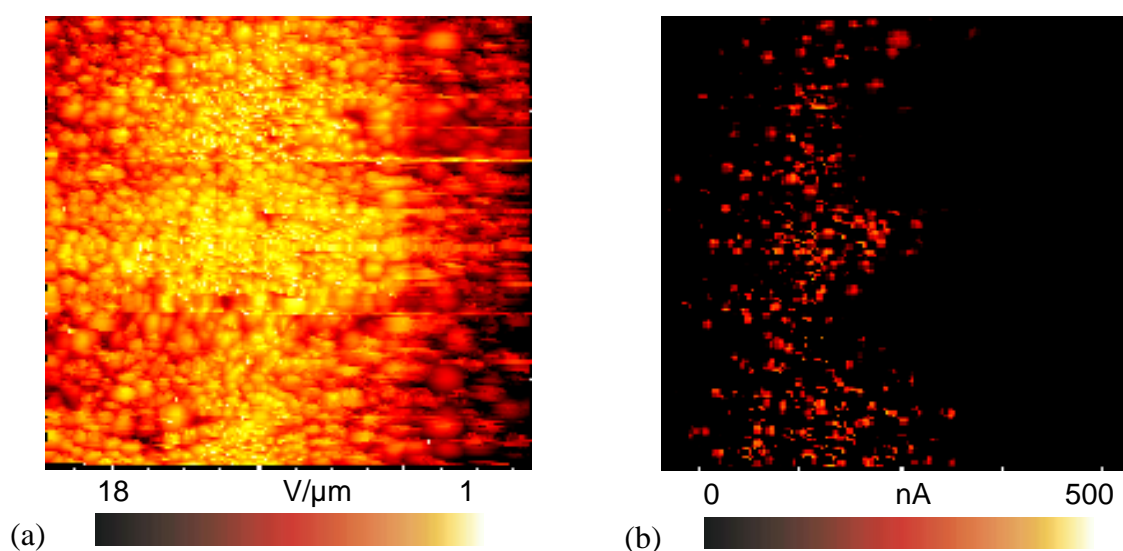


Fig. 4: (a) Onset field map for 2 nA current (scanned area $500 \times 500 \mu\text{m}^2$, anode diameter $\varnothing_A = 5 \mu\text{m}$, for more experimental details see ref. 12) and (b) current-map at $5 \text{ V}/\mu\text{m}$ (scanned area $400 \times 400 \mu\text{m}^2$, $\varnothing_A = 5 \mu\text{m}$) of the Au-coated Ni nanowire cathode showing a maximum of 1.6×10^6 emitters/ cm^2 at $18 \text{ V}/\mu\text{m}$ and 1.4×10^5 emitters/ cm^2 at $5 \text{ V}/\mu\text{m}$, respectively.

[Fig. 3 (a)] yields only 1.5×10^5 emitters/ cm^2 at $25 \text{ V}/\mu\text{m}$, Au coating leads to 1.6×10^6 emitters/ cm^2 at $18 \text{ V}/\mu\text{m}$ [Fig. 4 (a)], i.e., about 16% of the well-aligned Au-coated nanowires have been activated already. Focusing on the strongest emitters with onset fields for 2 nA below $2 \text{ V}/\mu\text{m}$, only ten are found on bare Ni compared to about 100 on Au-coated Ni. The very different FE strength is confirmed by the current maps in Figs. 3 (b) and 4 (b), which show 1.6×10^4 emitters/ cm^2 at $10 \text{ V}/\mu\text{m}$ for bare and 1.4×10^5 emitters/ cm^2 for Au-coated Ni nanowire samples at $5 \text{ V}/\mu\text{m}$. These numbers demonstrate the strong influence of the Au coating on the FE stability of Ni nanowires.

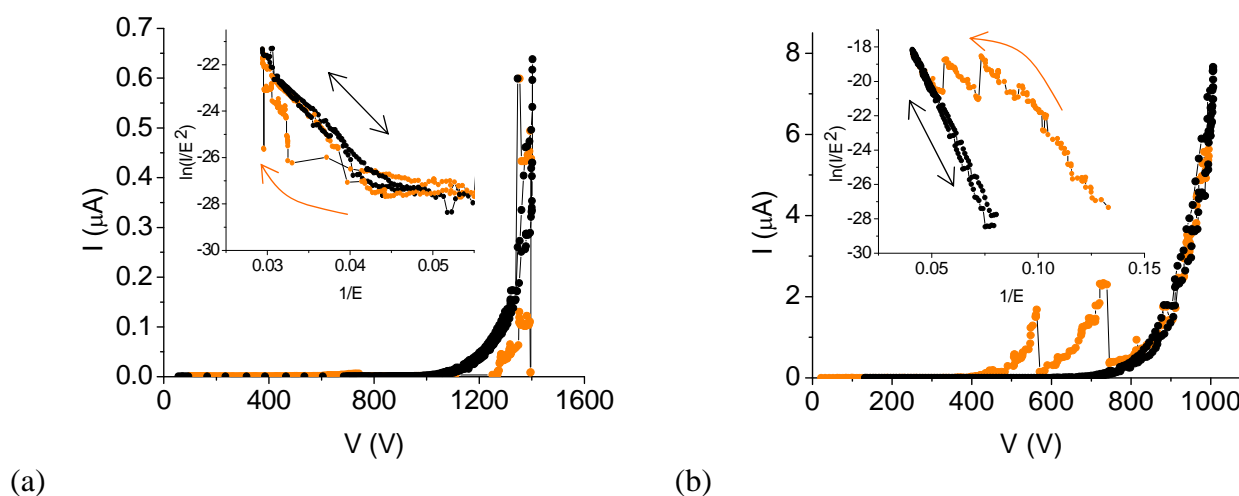


Fig. 5: Typical I - V curves and corresponding FN plots (inset) of emitting sites for a) bare and b) Au-coated Ni nanowires, showing stable FN behaviour after current processing. The arrows indicate the initial increase and reproducible voltage cycles.

In order to learn more about the nanowire emitters, local FESM measurements were performed with a lateral resolution of about $8 \mu\text{m}$. Typical examples of I - V curves of emitters on bare and Au-coated Ni nanowire samples are given in Fig. 5. Especially, the bare ones initially suffer from unstable emission which has often led to big current jumps or emitter destruction. In contrast, Au-coated ones show more stable emission in consecutive voltage cycles, sometimes, however, with strong irreversible current drops which hint for a partial destruction of nanowire bundles. After the current processing all Ni nanowire emitters usually provide stable Fowler-Nordheim (FN) emission, as shown in the insets of Fig. 5. Accordingly, field enhancement factors β have been extracted from the FN plots of all investigated emitters assuming a work function ϕ of 4.5 eV. The logarithm of these values can be fitted by Gaussian distributions, as shown in Fig. 6. The resulting mean β values of 331 for bare Ni and 302 for Au-coated Ni nanowires are about twice as large as the aspect

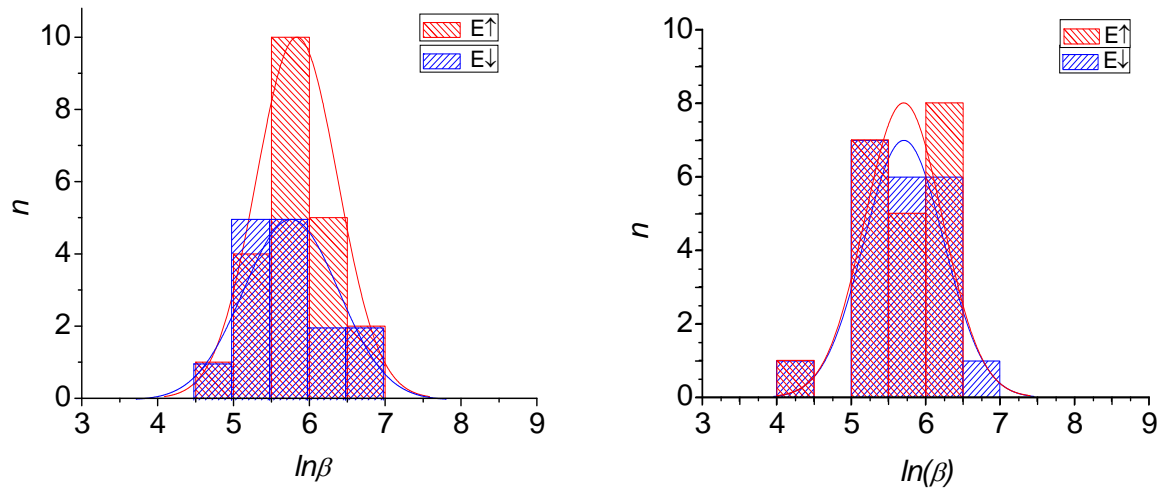


Fig. 6: Fitted Gaussian distributions of β -values extracted from I - V curves (for increasing and decreasing field E as indicated by arrows) of 20 emitting sites for bare (left) and Au-coated Ni nanowire emitters (right). The resulting mean β -values of the processed emitters are 331 and 302, respectively.

ratio estimated above and can be explained by the edge radius of the cylindrical wires which is about a quarter of the nanowire diameter, as discussed already for Cu nanowires. [7] It is remarkable that the measured reduction of about 10% for the Au-coated wires corresponds to the expected increase of the edge radius after coating. The large spread of measured values and onset fields “ E_{onset} (2 nA)” of the randomly chosen emitters on both samples is summarized in Fig. 7. For the bare Ni nanowires the current processing effect is much more

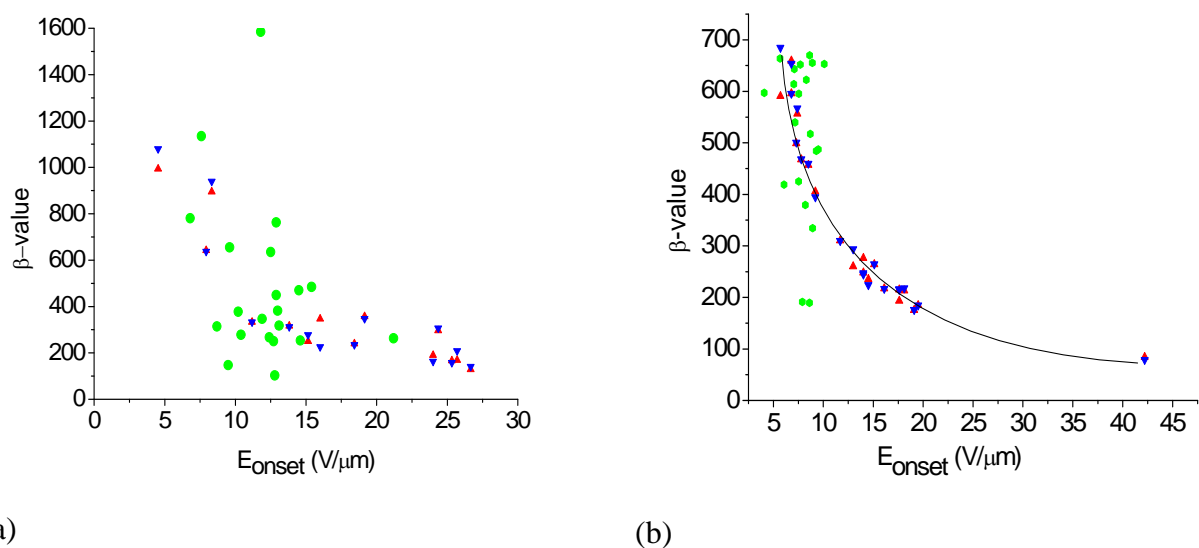


Fig. 7: Onset fields E_{onset} (2 nA) vs. β -values for (a) bare and (b) Au-coated Ni nanowire emitters. Compared are the data before any processing (\bullet) and after processing (\blacktriangle , \blacktriangledown in up and down cycles of E resp.). After processing a hyperbolic correlation (full line) becomes more evident.

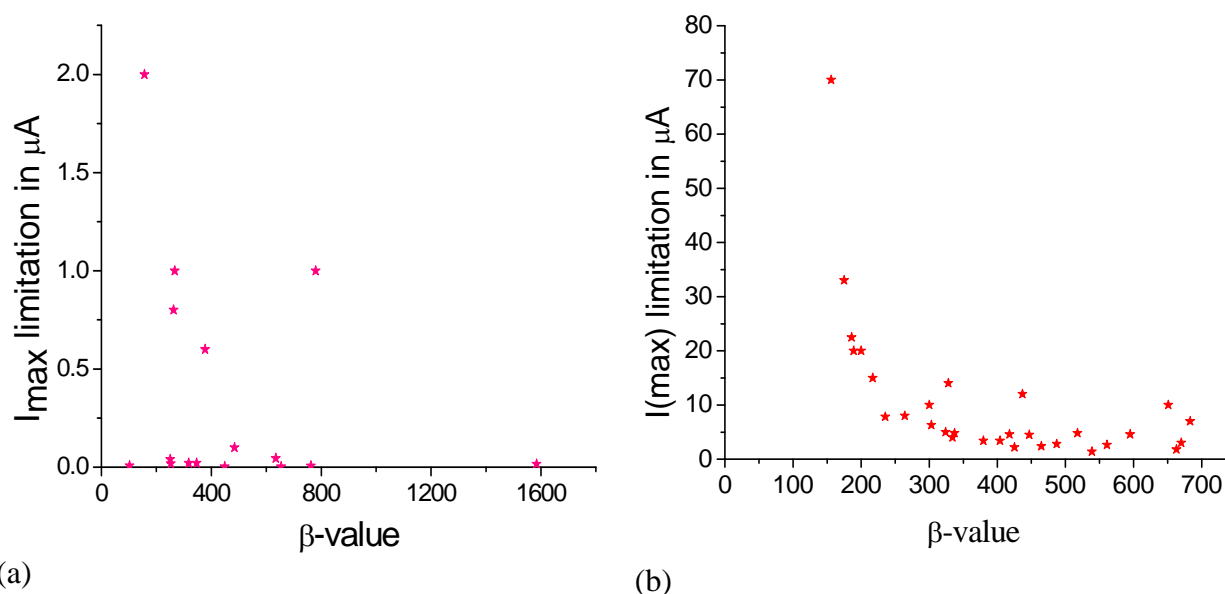


Fig. 8: Maximum achieved currents I_{max} and β -values for 16 emitting sites on the bare (a) and 30 on the Au-coated Ni nanowire sample (b).

pronounced and leads to a reduced number of stable emitters. In contrast, the processed Au-coated nanowires seem to follow a hyperbolic correlation ($\beta E_{onset} = \text{const}$) which might be expected for the given FE current. The improved emission stability of the Au-coated Ni nanowires is also demonstrated in Fig. 8 where the maximum achieved local currents I_{max} are plotted as function of the β values. On average the bare Ni emitters yielded about 0.4 μA in

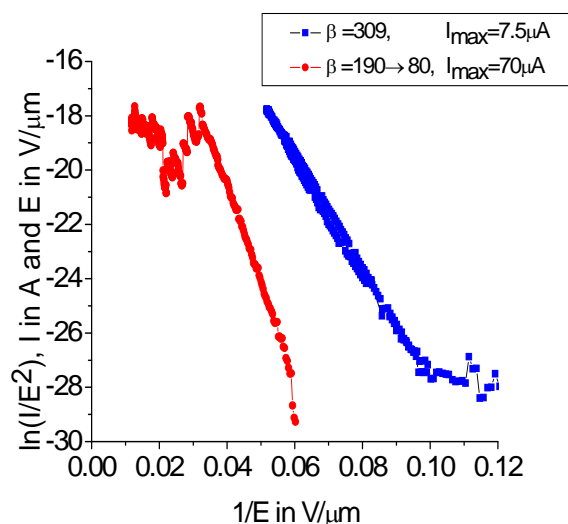


Fig. 9: Fowler-Nordheim plot of emitting sites on the Au-coated Ni nanowire cathode showing a stepwise destruction of (~9) emitters (left) or stable FN-behaviour (right).

comparison to 8 μA for the Au-coated ones. The high current carrying capability of up to 70 μA for Au-coated Ni nanowires is correlated to the β values below 200. Both observations might be explained by clusters of nanowires with enhanced current limits and mutual shielding effect. This assumption is further supported by the occurrence of multiple branches with reducing values in the I - V curves of emitters with current limits above 10 μA , as shown in Fig. 9. It is most straightforward to explain this by the successive destruction of single nano wires present at the measured spot, which might be present according to the SEM images in Fig. 2.

7.4. Conclusions

The field emission results of freestanding Ni nanowires electrochemically deposited in the pores of polymer ion-track membranes are promising. Gold coating on Ni nanowires has improved the FE properties in terms of higher emitter number density at 10 V / μm and current carrying capability of emitters due to better emission stability despite of slightly higher values before coating. At maximum $10^6/\text{cm}^2$ emitters were activated by exposing the nanowires to the field of up to 18 V / μm , thus about 10% of nanowires emitted. Most of the emitters showed stable FN behavior after current processing. The field enhancement factors of nanowires are about twice as large as the aspect ratios due to their cylindrical geometry with sharp edges. The effect of clustering of nanowires, visible in SEM, was observed nicely as successive destructive branches in the local I - V measurements. These findings indicate that with further optimization of growth and processing, Au-coated Ni nanowires are promising materials for cold cathode applications.

Acknowledgments

The authors thank the GSI for support, C. Trautmann for discussion for the fabrication of the templates, and D. Lysenkov for valuable suggestions and support. Financial support from DESY is also acknowledged.

References

- [1] N. S. Xu and S. E. Huq, *Mater. Sci. Eng.*, **R.48**, 47 (2005).
- [2] B. Bhushan, *Springer Handbook of Nanotechnology* (Springer, Berlin, 2004), p. 100.
- [3] D. Dobrev, J. Vetter, and N. Angert, *Nucl. Instrum. Methods Phys. Res. B* **149**, 207 (1999).
- [4] L. Dauginet-De Pra, E. Ferain, R. Legras, and S. Demoustier-Champagne, *Nucl. Instrum. Methods Phys. Res. B* **196**, 81 (2002).
- [5] E. Ferain and R. Legras, *Nucl. Instrum. Methods Phys. Res. B* **208**, 115 (2003).
- [6] M. E. Toimil-Molares, V. Buschmann, D. Dobrev, R. Neumann, R. Scholz, I. U. Schuchert, and J. Vetter, *Adv. Mater. Weinheim, Ger.* **13**, 62 (2001).
- [7] F. Maurer, A. Dangwal, D. Lysenkov, G. Müller, M. E. Toimil-Molares, C. Trautmann, J. Brötz, and H. Fuess, *Nucl. Instrum. Methods Phys. Res. B* **245**, 337 (2006).
- [8] I. Enculescu, Z. Siwy, D. Dobrev, C. Trautmann, M. E. Toimil-Molares, R. Neumann, K. Hjort, L. Westerberg, and R. Spohr, *Appl. Phys. A: Mater. Sci. Process.* **77**, 751 (2003).
- [9] M. E. Toimil-Molares *et al.*, *Nucl. Instrum. Methods Phys. Res. B* **185**, 192 (2001).
- [10] L. Nilsson *et al.*, *Appl. Phys. Lett.* **76**, 2071 (2000).
- [11] W. DeSorbo, *Nucl. Tracks* **3**, 13 (1979).
- [12] D. Lysenkov and G. Mueller, *Int. J. Nanotechnol.* **2**, 239 (2005).

Chapter 8

Field emission properties of electrochemically deposited gold nanowires

A. Dangwal, C. S. Pandey, G. Müller, S. Karim, T. W. Cornelius, and C. Trautmann

Submitted to Applied Physics Letters

Abstract

Field emission properties of vertically aligned gold nanowires of different aspect ratios and spatial distribution are presented. The nanowires were electrochemically deposited into the pores of etched ion-track polymer membranes. High emission site densities up to $5.7 \times 10^5 \text{ cm}^{-2}$ based on a controlled field enhancement β of individual emitting sites were observed by means of field emission scanning microscopy. Local measurements reveal stable Fowler-Nordheim behaviour of the emitters up to currents of $100 \mu\text{A}$ which are on average hyperbolically correlated to the β values. The integral emission of Au nanowires cathodes for device application is also discussed.

Electron field emission (FE) from nanostructures has attracted much attention for vacuum nanoelectronic applications, such as flat panel displays, X-ray and microwave tubes, and various sensors.[1-3] Besides carbon nanotubes (CNTs), different semiconductor [4-6] and metallic [7-9] nanowires (NWs) have been investigated for this purpose. Field enhancements from such nanostructures strongly depend on their morphology, spatial distribution and interspacing. [10, 11] Moreover, the dependence of field enhancement factor β on the vacuum gap d has become an interesting topic of research to get an optimal performance of FE devices. [12]

In this article we present the FE properties of electrochemically deposited Au NWs. The ability to create highly conductive and crystalline metallic NWs with controlled dimensions is one of the main advantages of the electrodeposition process. [13] This method is suitable for large scale synthesis of NWs with well defined aspect ratios. Cu and Ni NWs fabricated by this technique have been reported earlier and showed interesting FE properties. [14, 15] The morphologies and FE properties of Au NWs were investigated by means of scanning electron microscope and field emission scanning microscope (FESM) [16]. FE results of the integral measurements on NW cathodes as well as the local properties of typical emitting sites are discussed.

Vertically aligned Au NWs electrochemically deposited into the pores of etched ion-track membranes which were prepared at the UNILAC linear accelerator of GSI (Darmstadt) by irradiating 30- μm -thick polycarbonate foils (Makrofol N, Bayer Leverkusen) with U ions of kinetic energy ~ 2.7 GeV and fluences of 10^6 - 10^7 ions per cm^2 , and subsequently etching the ion trajectories in 6N NaOH solution. The cylindrical pores were filled electrochemically with Au by using Sodium disulfiteaurate(I) as electrolyte. The process was stopped when the wire length reached desired value as calculated from the deposited charge. Finally the polymer matrix is dissolved in dichloromethane leading to randomly distributed gold NWs of

Sample	NW Site density (cm^{-2})	Length (μm)	Diameter (nm)	Aspect ratio
A	$\sim 10^6$	7.5	257	58
B	$\sim 10^7$	5.9	250	47
C	7.6×10^6	9.3	254	73
D	3.2×10^6	14.6	265	110
E	7.2×10^6	8.8	121	145.5

Table 1: Overview of Au NWs samples reported in this letter.

lengths $\sim 6\text{-}15\ \mu\text{m}$ with a diameter $\sim 120\text{-}265\ \text{nm}$ [17, 18] as shown in Fig. 1. We have estimated the length and site densities of NWs from such SEM images as listed in Tab. 1. The NWs in all cases are free standing except for sample D, where most NWs are agglomerated due to the bending of long free-standing NWs, resulting in an increased effective spacing.

The emission site density and current distribution of all samples were measured at the pressure of 10^{-9} mbar in the FESM, using a tungsten anode of $5\ \mu\text{m}$ tip radius. Proportional-Integral-Derivative-regulated voltage scans for a constant current of $2\ \text{nA}$ provide electric field (E)-maps of the scanned areas, from which the potential emission site density N_{max} up to

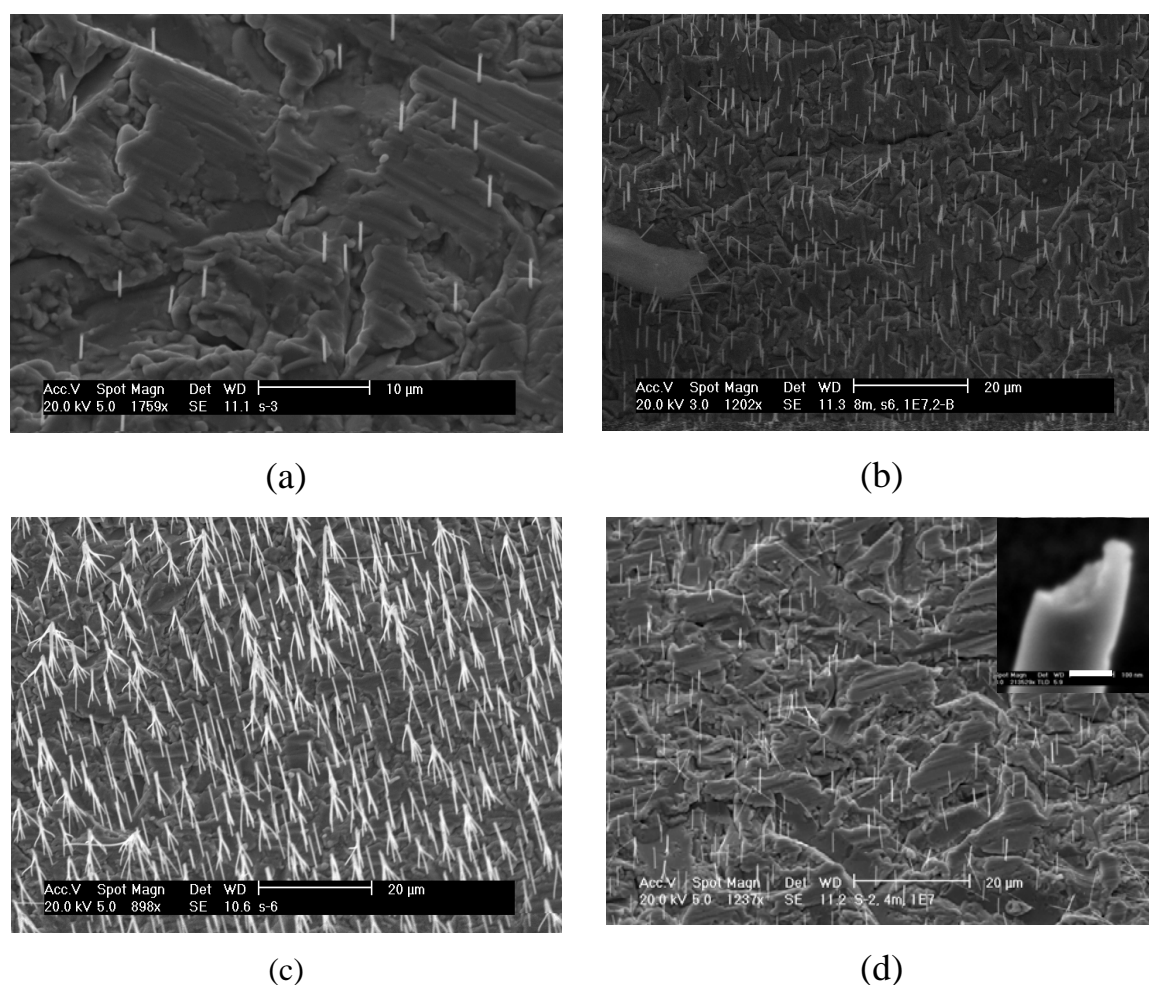


Fig. 1: SEM micrographs of samples A (a), C (b), D (c), and E (d) showing nanowires of different number densities and lengths. The inset of d shows a NW tip (scale bar = 100 nm).

the given maximum field E_{max} is determined. Such E -maps for samples A, C, D, and E in Fig. 2 obviously show the distribution of free-standing and agglomerated NW emitting sites with a lateral resolution of $5\text{-}7\ \mu\text{m}$. Resulting values of N_{max} for samples A, B, C, D, and E are: 4×10^5 , 2.4×10^5 , 5.7×10^5 , 4.4×10^5 , and 5.6×10^5 emitters/ cm^2 , at E_{max} of 33, 43, 17, 30 and 20

V/ μm . The E-map of sample A suggests that at least 40% of the NWs ($\sim 10^6 \text{cm}^{-2}$) are emitting. The lowest onset field of $\sim 4 \text{ V}/\mu\text{m}$ for the strong emitters on sample D can be accounted for the fact that lower site density for the given wire length might lead to weaker

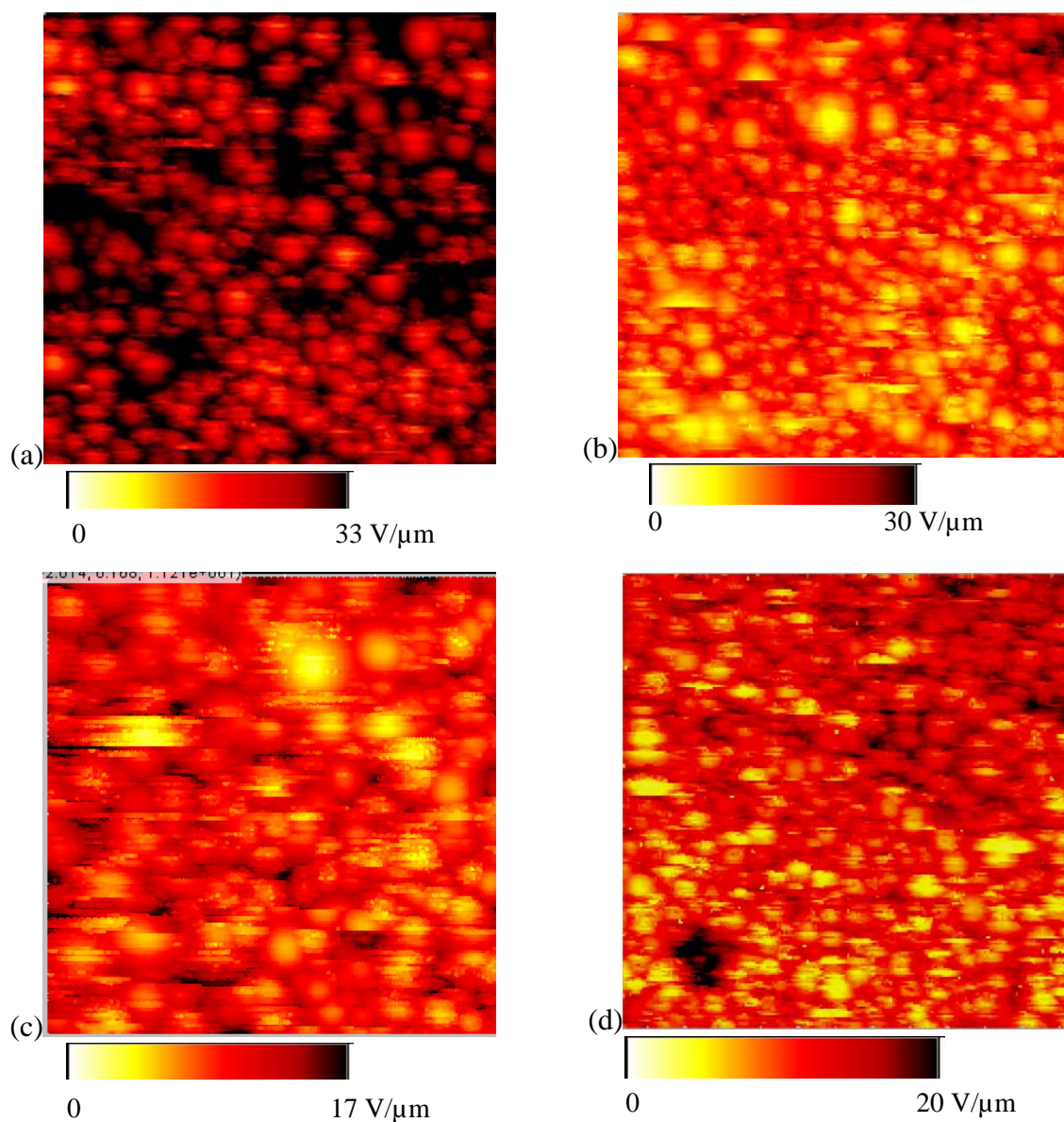


Fig. 2: Electric field maps required for a current of 2 nA for samples A, C, D, and E (W anode with tip radius $2.5 \mu\text{m}$, scanned area $0.5 \times 0.5 \text{ mm}^2$).

field-screening effect. [11] The subsequent current (I)-maps at constant voltage reveal the real activated number density N of emitting sites at a fixed electric field E . N values of $8 \times 10^4 / \text{cm}^2$ at $12 \text{ V}/\mu\text{m}$, $2.6 \times 10^4 / \text{cm}^2$ at $25 \text{ V}/\mu\text{m}$, 10^5 , 3.4×10^4 , and $1.4 \times 10^5 / \text{cm}^2$ at $6 \text{ V}/\mu\text{m}$, have been obtained for samples A, B, C, D, and E (Fig. 3 (a)), respectively. Thus, these Au NW cathodes show in comparison to CNTs much larger emitter number densities with respect to the number of deposited nanostructures.

The FE properties of Au NWs were further investigated by local FESM measurements of randomly chosen emitting sites for each sample. A typical I-E curve is shown in Fig.3 (b), which confirms the linear $\ln(I/E^2)$ vs. $1/E$ dependence expected from Fowler-Nordheim (FN) theory. [19] In general during initial increase of electric field NWs unstable emission was

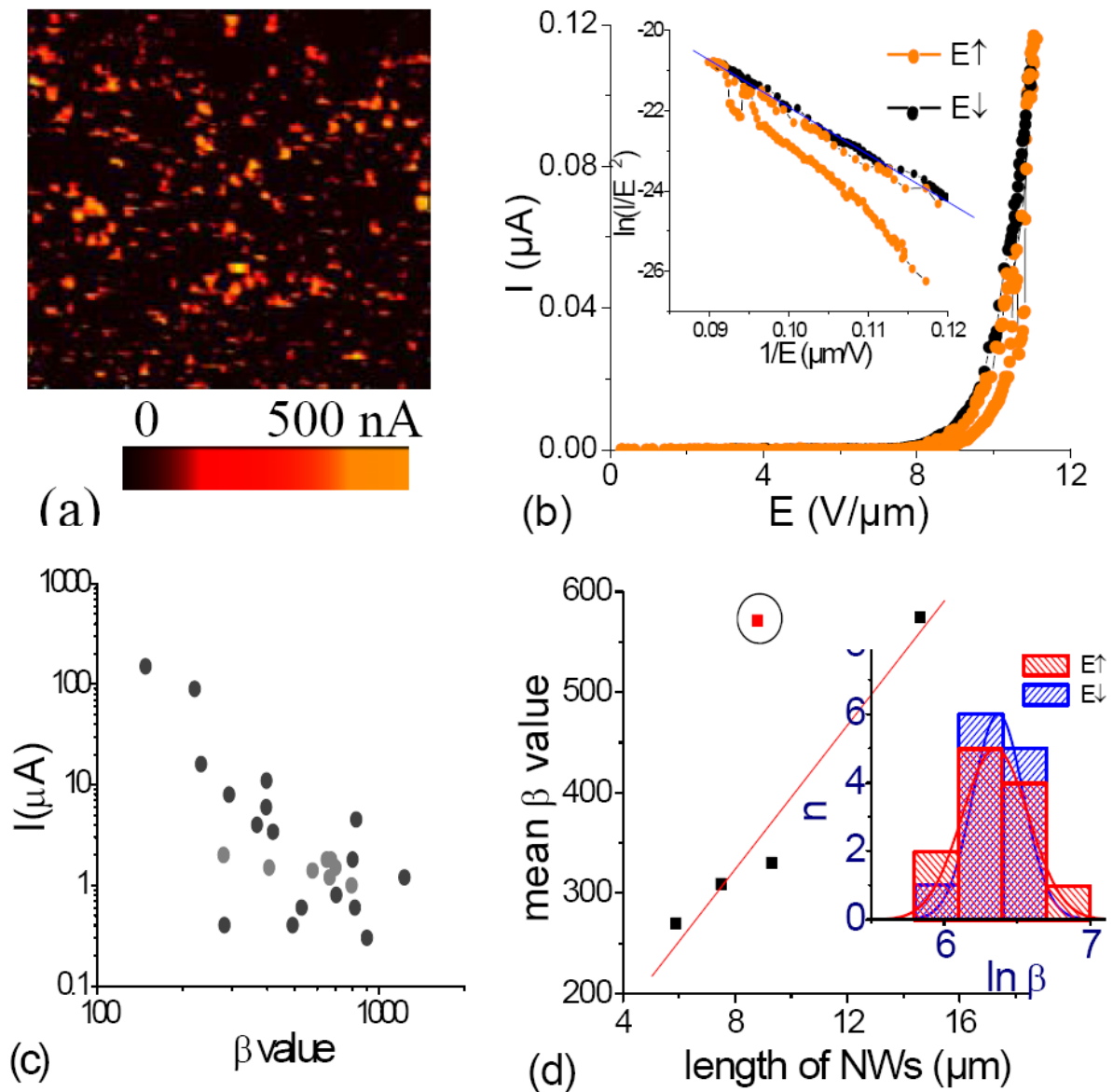


Fig. 3: (a) I-map of sample E with 1.4×10^5 emitters/cm² at 6 V/μm, (b) locally measured I-E curve and FN plot for a single emitting site, (c) FE current limits as a function of β value for sample D: black dots represent current just before partial or full destruction of emitters, while black dots correspond to survived ones, and (d) plot of mean β value vs. length of NWs for all samples, showing deviation for sample E (encircled). The inset shows the histogram of $\ln(\beta)$ for 12 stable emitting sites of sample E.

observed, probably due to adsorbates [20] or partial destruction of NW tips caused by high FE currents [15], which tends to stabilize in the succeeding up and down cycles. Such an

example is given in Fig. 3(b), where the emitting site gets activated and provides more stable emission later on. The current carrying capabilities of the emitting sites were also measured until partial or full destruction. The emitting sites on sample D possess the highest maximum current (I_{\max}) values among all samples because of the agglomerated clusters of NWs. I_{\max} vs. β plot for sample D in Fig. 3(c) shows scattered maximum current values lying between 0.5-100 μA , which are on average hyperbolically related to the β values. These observations might reflect enhanced heating effects of sharper and longer NWs and successive destruction of single NWs in agglomerated clusters, as evident from the I-V curves with multiple destructive branches. [20]

The local field enhancement factor, β_{local} , were retrieved from the FN plots of individually measured emitting sites (taking a work function of 5 eV), and the mean value was derived from a Gaussian distribution fit of the histogram of $\ln(\beta)$, as given in Fig. 3 (d) inset for sample E. The linear increase of the average β_{local} with the length of NWs and the deviation for sample E shown in Fig 3 (d) are expected from their geometrical aspect ratio. The average β_{local} values are found to be 3.9 to 5.7 times larger than the aspect ratios due the reduced edge radius at the tips of NWs, as observed in the SEM images (Fig. 1(d) inset). Different edge radii at the NW tips can also be accounted for the spread in β_{local} values. It is remarkable that the distribution of β_{local} is narrowest for thin NW sample E, with a spread factor of only 1.23 (mean $\beta_{\text{local}} = 570$, Fig 3 (d) inset) as calculated from mean width at half maximum of the Gaussian fit.. This might be explained by the fact that the variation of edge radii is reduced for reduced NW diameter. A narrow distribution of β reflects the controlled FE behavior of our NWs which is most demanding for FE homogeneity of devices.

Integral FE experiments with varying vacuum gap d were performed by using a conical W anode of 300 μm base diameter. Figure 4(a) shows the measured current-field (I-E) curves of sample D (containing clustered Au NWs) at different values of d . The macroscopic threshold field required to produce 1 mA/cm^2 is about 9, 9.7, 10, 13, and 22 $\text{V}/\mu\text{m}$ at d equal to 160, 140, 105, 63 and 28 μm , respectively. No current saturation is observed in any case and a maximum current density of 78 mA/cm^2 is achieved at 13 $\text{V}/\mu\text{m}$ for d equal to 0.16 mm. The corresponding FN plots shown in Fig. 4(b) are in excellent agreement with FN theory with retrieved β values of 277, 458, 586, 604, and 632 at d equal to 28, 63, 105, 140, and 160 μm , respectively.

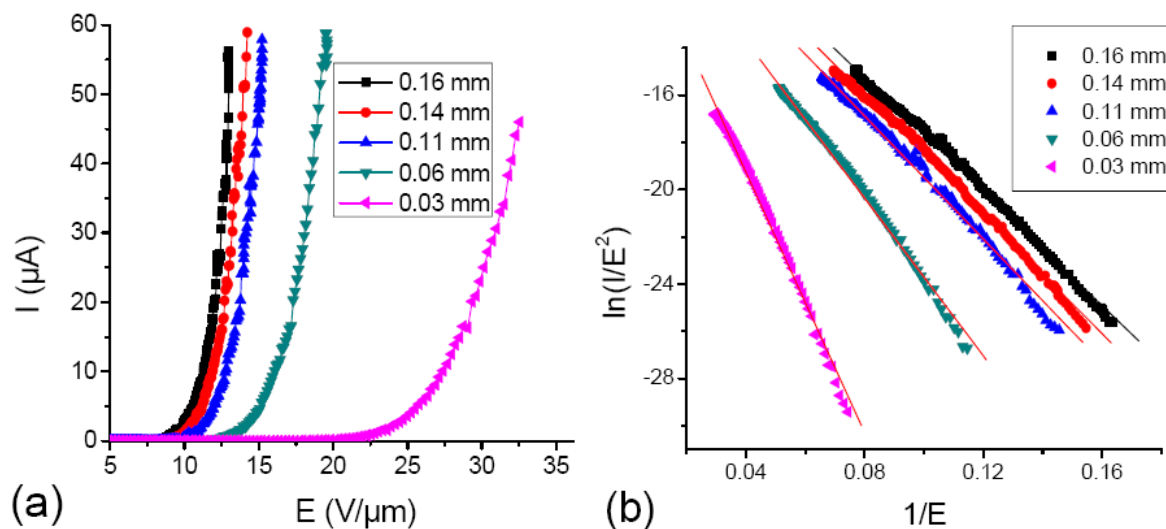


Fig. 4: Integral measurements of NWs with $300\ \mu\text{m}$ anode diameter: (a) I - E curves for thin NWs (sample E) with varying vacuum gap, and (b) corresponding FN curves.

A two-region FE model has been proposed by Zhong *et al* for explaining the β vs. d relationship. [12, 21] Figure 5 shows that for all investigated Au NW samples the experimental data fits very nicely with the universal relation when d is close to the length of NWs. [21] Sample D possess the highest β values of our NW samples, thus demonstrating the benefit of long and clustered NWs. It is noticeable that the ' β - d ' curves for samples C and E lie very close and parallel to each other due to similar site density and wire lengths despite of

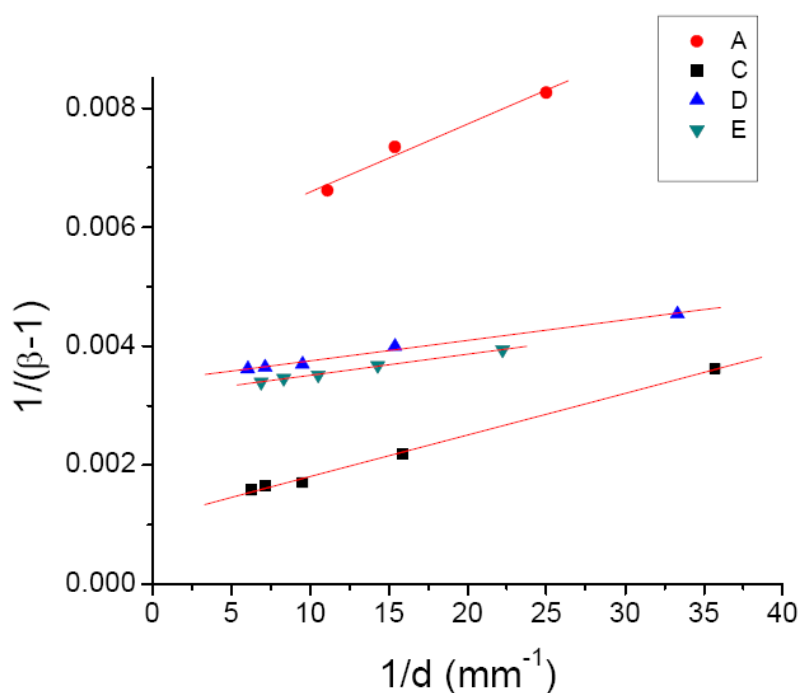


Fig. 5: $1/\beta$ vs. $1/d$ plot showing the linear dependence for all Au NW cathodes.

a factor two different wire diameters, while the curves for sample A containing free standing NWs with less density and sample D of clustered NWs show a stronger variation of β with d . These results will surely help to achieve the condition of least variation in β with respect to the vacuum gap by optimizing the fabrication parameters of NWs and so for FE devices.

In conclusion, the FE properties of vertically aligned Au NWs were presented. It was observed that up to 40 % of NWs were emitting sites. Individually measured emitters provided stable FN emission with a very low β spread factor of 1.23, thus demonstrating the controlled FE behaviour of Au NWs. The emission current density up to 78 mA/cm² was achieved from a Au NW cathode without any current saturation. The experimental data followed the universal relation between β and d and gives valuable hints for optimized fabrication parameters. Our results emphasize that electrochemically deposited Au NWs are promising materials as cold cathodes.

The authors thank Electrical Engineering Department at the University of Wuppertal for providing SEM facilities. Financial support from DESY is also acknowledged.

References

- [1] J. W. G. Wildoer, L. C. Venema, A. G. Rinzler, R. E. Smalley, and C. Dekker, *Nature* (London) 391, 59 (1998).
- [2] Z. W. Pan, Z. R. Dai, and Z. L. Wang, *Science* 291, 1947 (2001).
- [3] W. B. Choi, D. S. Chung, J. H. Kang, H. Y. Kim, Y. W. Jin, I. T. Han, Y. H. Lee, J. E. Jung, N. S. Lee, G. S. Park, and J. M. Kim., *Appl. Phys. Lett.* 75, 3129 (1999).
- [4] A. M. Morales and C. M. Lieber, *Science* 279, 208 (1998).
- [5] X. Duan, Y. Huang, Y. Cui, J. Wang, and C. M. Lieber, *Nature* 409, 66 (2001).
- [6] X. Duan, C. M. Lieber, *Adv. Mater.* 12, 298 (2000).
- [7] T. C. Wong, C. P. Li, R. Q. Zhang, and S. T. Lee, *Appl. Phys. Lett.* 84, 407 (2004).
- [8] B. E. Alaca, H. Sehitoglu, and T. Saif, *Appl. Phys. Lett.* 84, 4669 (2004).
- [9] F. Zhang, R. Barrowcliff, G. Stecker, W. Pan, D. Wang, and S. Hsu, *Jpn. J. Appl. Phys.* 44, 398 (2005).
- [10] L. Nilsson, O. Groening, C. Emmenegger, O. Kuettel, E. Schaller, L. Schlapbach, H. Kind, J. M. Bonard, and K. Kern, *Appl. Phys. Lett.* 76, 2071 (2000).
- [11] S. H. Jo, J. Y. Lao, Z. F. Ren, R. A. Farrer, T. Baldacchini, and J. T. Fourkas, *Appl. Phys. Lett.* 83, 4821 (2003).
- [12] D. Y. Zhong, G. Y. Zhang, S. Liu, T. Sakurai, and E. G. Wang, *Appl. Phys. Lett.* 80, 506 (2002).
- [13] H. He, *Encyclopedia of Nanoscience and Nanotechnology*, edited by H. S. Nalwa (American scientific publishers), ISBN: 1-58883-001-2.
- [14] F. Maurer, A. Dangwal, D. Lysenkov, G. Müller, M. E. Toimil-Molares, C. Trautmann, J. Brötz, and H. Fuess, *Nucl. Instrum. Methods Phys. Res. B* 245, 337 (2006).
- [15] A. Dangwal, G. Müller, F. Maurer, J. Brötz, and H. Fuess, *J. Vac. Sci. Technol. B* 25, 586 (2007).
- [16] D. Lysenkov and G. Mueller, *Int. J. Nanotechnol.* 2, 239 (2005).
- [17] J. Liu, J. L. Duan, M. E. Toimil-Molares, S. Karim, T. W. Cornelius, D. Dobrev, H. J. Yao, Y. M. Sun, M. D. Hou, D. Mo, Z. G. Wang, and R. Neumann, *Nanotechnology* 17, 1922 (2006).
- [18] S. Karim, M. E. Toimil-Molares, F. Maurer, G. Miehe, W. Ensinger, J. Liu, T. W. Cornelius, and R. Neumann, *Appl. Phys. A* 84, 403 (2006).
- [19] R. H. Fowler and L. W. Nordheim, *Proc. Royal Soc. (London)* A119, 173, (1928).

- [20] K. A. Dean and B. R. Chalamala, *Appl. Phys. Lett.* 76, 375 (2000).
- [21] X. Y. Xue, L. M. Li, H. C. Yu, Y. J. Chen, Y. G. Wang, and T. H. Wang, *Appl. Phys. Lett.* 89, 043118 (2006).

Summary and Outlook

The investigations performed on niobium and copper samples reported here provide a detailed and comprehensive view of the role of material properties, surface preparation and cleaning techniques in suppressing the field emission, which is otherwise disastrous for high field vacuum devices. The other part of this work was to study various nanowire structures for getting improved field emission properties useful for cold cathode applications.

The field emission scanning microscope was modernized with LabVIEW based programs, developed for faster scans and data acquisition and analysis, which significantly improved the existing system in its speed.

FE investigations on Nb and Cu surfaces

Polycrystalline niobium samples, prepared by standard electropolishing method, showed the shift of onset field emission from 40 MV/m to 60 MV/m and halved emitter density at 120 MV/m after high pressure ultra pure water rinsing (HPR). At present the intended cavity performance is $E_{acc} = 30$ MV/m for nine-cell cavities, (i.e. $E_{surface} \approx 60$ MV/m), so these samples were the examples of bad surface preparation but demonstrated the root of the problem. Still survived emitters were identified in SEM as the particles up to 60 μm size. An observed sulphur containing particle was assumed to be the residue of electropolishing process. Sulphur contamination in the regularly used electropolishing baths used for cavity preparation was observed in different laboratories (e.g. DESY Hamburg, CEA Saclay), and the efforts for avoiding or suppressing it have been started.

Apart from the conventional cleaning of HPR used in cavity fabrication, we focused our investigations on the dry-ice cleaning (DIC) technique. Systematic measurements on polycrystalline copper and niobium and single crystal niobium samples showed the shift of onset fields from 90 to 120 MV/m in the former case and from 200 to 250 MV/m in later; and huge reduction of the number density of field emitters at a given field level. In the best case, one dry ice cleaned single crystal niobium sample did not show any FE up to 250 MV/m.

The impact of DIC on individual emitters was also studied locally. Decreased β and increased S values were observed and can be understood by the smoothed edges of the emitters after DIC. SEM studies have clearly demonstrated the mechanical and thermal effect of DIC on field emitters resulting in to the partial or complete removal of contaminants and particulates down to 400 nm. Most attractive was to observe the partial smoothing of the edges of surface protrusions, clearly visible for features large up to 5 μm in size as well as

small down to 200 nm. In conclusion, DIC emerged as a very efficient tool for the reduction of FE sites from Cu and Nb surfaces. Our results strengthen the proposal of using dry-ice cleaning as the final cleaning step for superconducting niobium cavities as well as in the applications unsuitable for water like Cu gun cavities.

Large grain and single crystal niobium samples were chosen finally for field emission investigation, to compare those with presently used polycrystalline niobium material for cavity fabrication, and so to explore the possibility for their alternative use. Buffered chemical polishing of these samples yielded the mirror like surfaces of roughness $\sim 6 - 18$ nm measured over the area of $80 \times 80 \mu\text{m}^2$, which was about 15 times smoother than electropolished polycrystalline Nb material. The onset of emission observed at very high fields (150 – 200 MV/m), was the benefit of such a high quality surfaces. Thus, large grain or single crystal Nb seems to be an alternative to polycrystalline Nb for cavities of high performance accelerators like XFEL and ILC.

Since grain boundaries get easily contaminated by the segregation of impurities, their effects on enhanced FE has always been a matter of discussion, but no direct evidence was found. Also, in our investigations on as prepared large grain Nb samples, no grain boundary effect was observed in voltage-scans up to the fields of 250 MV/m. As the impurity segregation is more pronounced during the heat treatments, one large grain Nb sample was heat treated at 150 ± 10 °C in high vacuum for 14 hrs. The following voltage scans at 250 and 300 MV/m fields have shown the first proof of grain boundary assisted enhanced field emission. However, similar experiments on more samples of large grain Nb together with the SEM investigations before and after heat treatment are required for better understanding of grain boundary assisted FE.

Efforts have also been made to derive the values of work function ϕ for different crystal orientation of single crystal Nb surfaces by intrinsic FE measurements. Anisotropic ϕ values of 4.05 and 3.76 were obtained for (111) and (100) planes of Nb. These results are within the error of 17 and 27 %, respectively.

From the comprehensive study in last three years on different Nb surfaces, a correlation between sizes of all investigated emitters derived from SEM images with respect to their respective onset fields is found, which sets a threshold for the tolerable defect size up to 1.3 (3) μm to achieve the proposed accelerating gradients of 30 (40) MV/m in XFEL (ILC) cavities reliably.

FE investigations on Cu, Ni and Au nanowires:

Investigations on FE properties of electrochemically deposited Cu, Ni and Au nanowires of different aspect ratios and spatial distribution were performed.

First measurements on Cu nanowires showed that only 6% of deposited free-standing and vertically aligned nanowires were strong emitters. Nearly all wires showed unstable FN behaviour i.e. showing different β values for ascending and descending voltage cycle, resulting mean β value of 245, which is a factor three higher than expected from the emitter shape due to the influence of the tip geometry. For nanowires of 18 μm length and submicron spacing, several hundred nanowires agglomerated into bundles, which showed higher emitter densities as well as higher stable currents. This was clearly due to decreased effective spacing which has decreased the mutual shielding effect of neighbouring nanowires.

More detailed analysis on Ni nanowires has shown that gold coating improves the FE properties in terms of higher emitter number density at 10 V/ μm and current carrying capability of emitters due to better emission stability. At maximum 10^6 emitters/ cm^2 were activated by exposing the nanowires to the field of up to 18 V / μm , thus about 10% of nanowires emitted. Most of the emitters showed stable FN behavior after current processing. The field enhancement factors of nanowires were about twice as large as the aspect ratios due to their cylindrical geometry with sharp edges. The effect of clustering of nanowires, visible in SEM, was observed nicely as successive destructive branches in the local I-V measurements.

Improved FE properties of Ni nanowires achieved by gold coating lead us to investigate bare Au nanowires. Au Nanowires with site density of $10^6/\text{cm}^2$ and 7.5 μm lengths showed that up to 40 % percentage of the wires were emitting. This was the best result among all of the investigated nanowire samples, indicating that 10 μm is an optimum inter wire spacing for 7.5 μm long nanowires, which had resulted into more nanowires emitting due to minimized shielding effects.

The FE properties of randomly chosen emitting sites on each Au nanowire sample provided stable FN emission. Individual emitting sites on the agglomerated nanowire sample possess the highest maximum-current values (up to 100 μA). The average β values were found to be 3.9 to 5.7 times larger than the aspect ratios due the reduced edge radius at the tips of nanowires, as observed in the SEM images and in accordance to our previous findings. Different edge radii at the nanowire tips were also accounted for the spread in local β values of emitting sites. It is remarkable that the distribution of β is narrowest for thin NW sample

with a spread factor of only 1.23 and thus demonstrating the controlled FE behaviour of Au nanowires.

Integral FE experiments on all Au nanowire cathodes showed no current saturation in any case. In the best case (agglomerated nanowires) a maximum current density of 78 mA/cm² was achieved at 13 V/μm. For all investigated Au nanowire samples, the linear relation between field enhancement factor β of cathode and electrode spacing d was observed, which further gives valuable hints for optimized fabrication parameters.

In conclusion, among all above mentioned nanowires, the agglomerated nanowires appear to be superior to the free standing ones, in terms of current carrying capabilities as well as reduced shielding effects. Homogeneity of emission is still lacking on these samples. Fabrication of patterned nanowires would probably attain this goal, and growth of agglomerated nanowires at the well defined positions should be preferred. This would provide the advantage of agglomerated nanowires capable to carry high currents as well as the homogeneous emission over the cathode surface, as required for cold cathode applications.

Appendix A

Analysis of Current Voltage data

The user interface of the programs developed for regulated voltage – scan and analysis of the current (I) – voltage (V) measurement data performed for the emitters localized are given in Fig. A1 and A2. The program compiles all current and voltage data of interest and allows the user to examine the data in different ways. The following is a selection of the choices:

1. The option to display I – V as well as I – E curves, with the electric field (E) values corrected for the geometrical correction factor α .
2. The option to perform I – V measurements on a particular emitter for number of up and down cycles of varying fields until the emitter attains a stable emission behaviour, or depending on the user's requirements.
3. The facility to save and plot the retrieved data simultaneously during measurements.
4. The option to extract the Fowler-Nordheim parameters of the emitter in all performed up and down cycles of measurements, for two different work functions if needed.

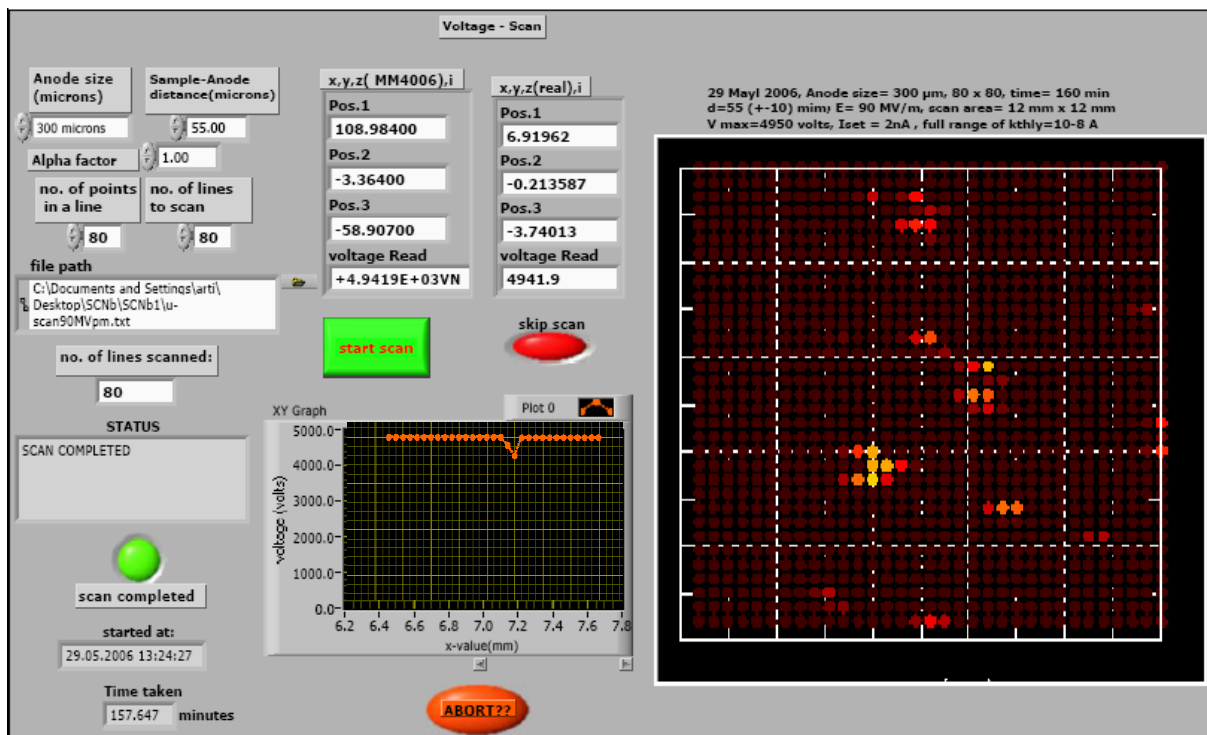


Fig. A1: User interface of the regulated voltage scan program.

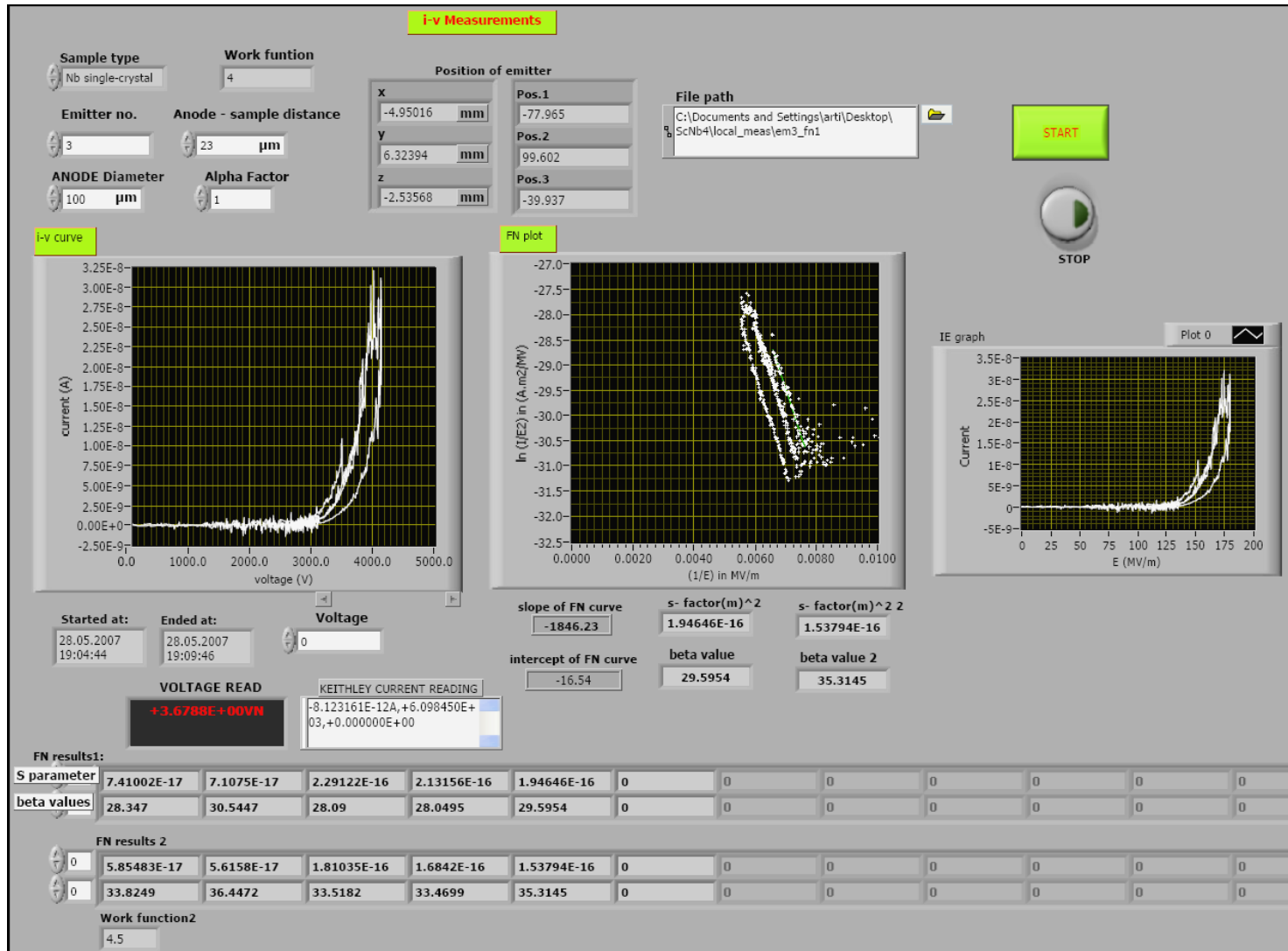


Fig. A2: User interface of the current – voltage data analysis program.

Appendix B

Interpretation of FN curves

According to FN theory, one should be able to retrieve the values of field enhancement factor β and the effective emission area S from the slope and intercept of the FN curve, respectively. However, there exists experimental problem with the measurements of current – voltage plots and so with the interpretation of corresponding FN curves. We know that I and the V are the directly measured quantities in the experiments. The measurement of I-V curves is made in step by step voltage increase mode and simultaneous retrieval of the current values. We have plotted three different FN curves for a single emitting site, with the different rates voltage increments. The hardware used were: Keithley 6485 digital picoammeter and FUG 5 KV power supply. On varying the rates of voltage variation with 1V per step, the modes for measurements were classified as: Fast for 30 steps/sec, medium for 6 steps/sec and slow for 1 step/sec.

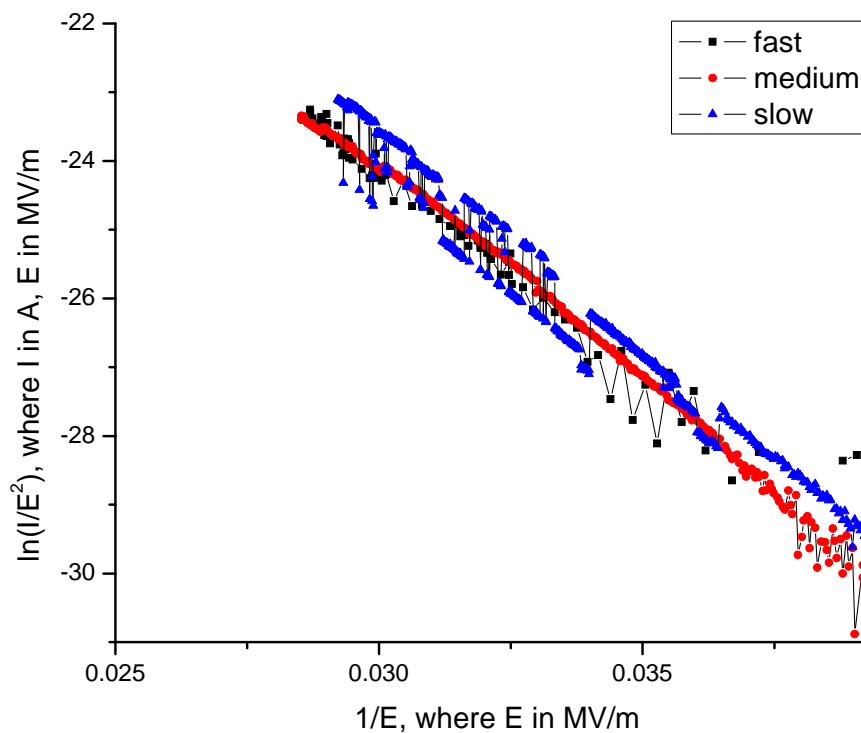


Fig. B1. FN curves on a single emitter with different measurement rates.

As observed in Fig. B1, we obtained different FN curves for different modes of voltage increments. In slow mode, the current data is scattered too much about the fit line,

possibly due to strong instability of field emission current in time, causing the changes in emitting site's parameters during measurements. Thus, the 'slow' curves are typically fluctuating and so not useful for interpretation. On the other hand, measurements with 'fast' and 'medium' modes of increasing voltage result the data points lying on the same fit line, and the fluctuation observed earlier are not visible now. It is important to note that the data points are too less in the fast mode, so, it is the medium mode of voltage increment, which gives the more reliable data for correct interpretation of FN curves.

Appendix C

Niobium surface

The studies of J. Halbritter on the oxidation of Nb have been quite detailed,¹ and focused on the interface properties of Nb and Nb oxide. Halbritter reports that the atmospheric oxidation of Nb is dominated by the solution of oxygen in Nb above 100 °C and the growth of amorphous Nb₂O₅ at the surface. The thickness of the Nb₂O₅ layer at room temperature is up to 60 Å. Both the oxide formation and the oxygen lattice gas dissolution strain the Nb/Nb₂O₅ interface heavily and thus create O segregates (mainly NbO₂ and NbO) that serrate the interface.

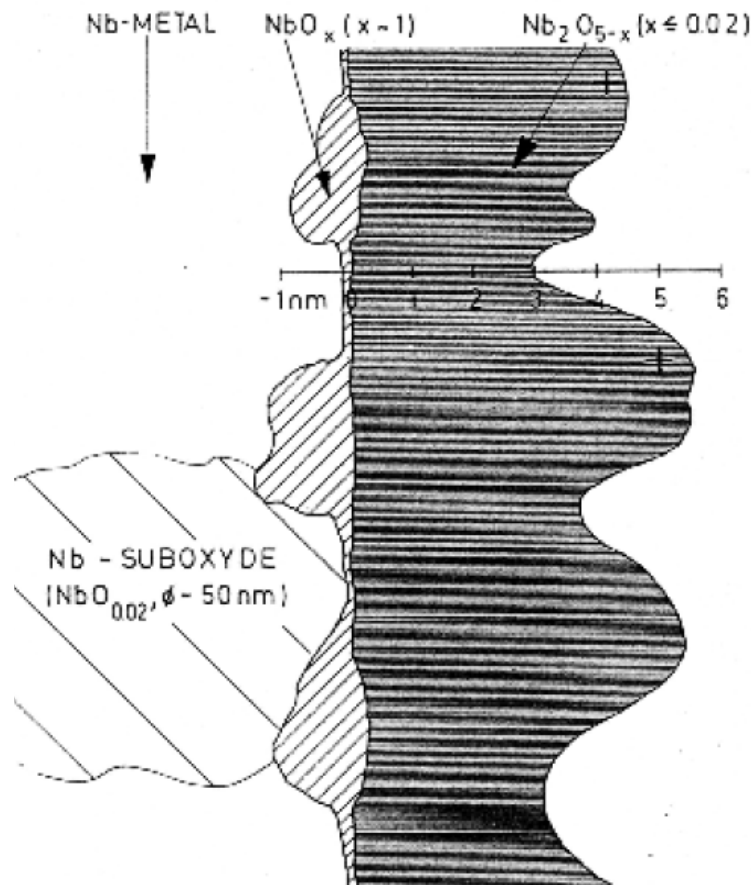


Fig. C1: Growth model for the wet (atmospheric) oxidation of a Nb surface. Beside a dielectric Nb₂O₅ layer at the surface (30-60 Å) the model assumes metallic oxide lumps (≈ NbO_{0.02}) in the Nb matrix and metallic NbO precipitates at the interface between metal and oxide. The surface roughness (20-25 Å) as well as the interface roughness (10-15 Å) is quite high and thus the thickness of the Nb₂O₅ layer is not very well defined.¹

¹ J. Halbritter, Appl. Phys. A 43 (1987) 1.

A schematic illustration of this oxide growth model is shown in Fig. C1. Halbritter proposes the following processes that occur at the Nb/Nb₂O₅ interface:

- solution in Nb and Nb₆O segregation to relax strain
- Nb₂O₅ nucleation, which strains and serrates the interface and generates defects underneath
- enhanced O diffusion by strain relaxation at defects into the Nb

Halbritter reports that atmospheric as well as dry oxidation (in 1 atmosphere O₂) result in the formation of Nb₂O₅ with a thickness between 20 and 60 Å. Although the dry oxidation is slower, the rough interface and the oxygen diffusion into the Nb remain similar as for oxidation in air.

Effect of low temperature heat treatment (110-150 °C) on niobium and its oxide

A consequence of heat treatment of Nb at ~150 °C is the interstitial oxygen diffusion from the oxidized niobium surface to the bulk material (Fig. C2). Based on the experiments performed by Palmer and Kneisel^{2, 3}, R_{BCS} change can be explained by the electron mean free path decrease due to oxygen diffusion. Further, oxygen diffusion is also treated as the probable real cause of the Q-slope improvement of niobium cavities.⁴

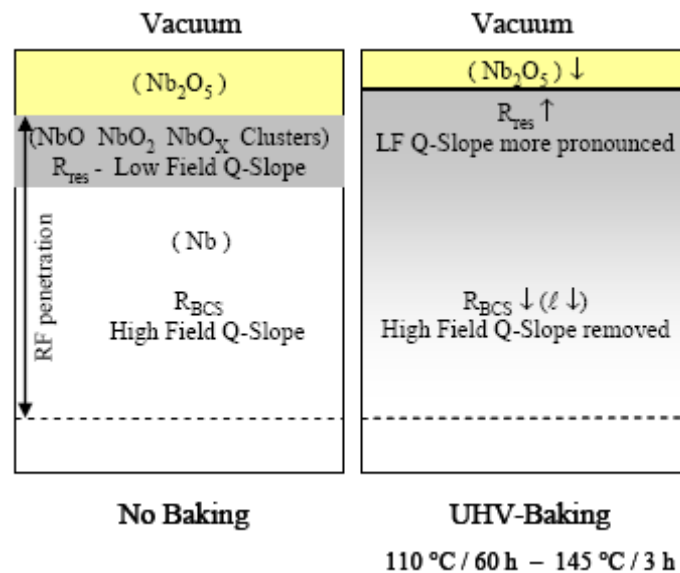


Fig.C2: Sketches of niobium surface (layer scale is not respected) summarizing experimental changes of R_{BCS} and R_{res} after heat treatments at temperatures 110 °C for 60 hrs or 145 °C for 3 hrs.⁴

² F.L. Palmer, IEEE Trans. Mag. 23, p. 1617 (1987).

³ P. Kneisel, 9th Workshop on RF Superconductivity, Santa Fe – USA (1999), TUP044.

⁴ B. Visentin #, Y. Gasser, and J.P. Charrier, 12th Workshop on RF Superconductivity, Ithaca USA (2005): TUP05.

Acknowledgements

With a sense of deep regards, I express my sincere thanks to my supervisor Prof. Dr. Günter Müller, for his inspiring guidance and support during this research work. His keen interest in research and regular discussion were helpful to enhance my scientific knowledge.

I am greatly indebted to Prof. Dr. Dieter Proch for providing all the facilities required for my work and encouragement and guidance time to time.

I would like to thank Jahan Pouryamout for solving various minor and major problems many times related to vacuum techniques with his skilful knowledge.

I thank my colleague Dr. Dmitry Lysenkov for interesting and constructive discussions during some stages of this research work.

My sincere thanks goes to DESY colleagues, firstly to Dr. Detlef Reschke for providing the high pressure rinsed and dry ice cleaned samples, for fruitful discussion as well as all time support. I thank to Dr. Waldemar Singer for valuable discussions, Dr. Xenia Singer for providing large grain and single crystal niobium samples, Dr. Klaus Floettmann for copper samples, and Mr. Axel Matheisen for electropolished niobium samples. I also acknowledge Dr. Reinhold Mayer for helping me in all the administrative levels.

I would like to thank other collaborating partners, Dr. Florian Maurer and Dr. Shafqat Karim at GSI Darmstadt for providing metallic nanowire samples.

I am grateful to Dr. Ralf Heiderhoff for providing the SEM facility in the electrical engineering department with the earliest possibility whenever required.

I owe a special word of thank to Mrs. Katrin Lando at DESY for her unfeeling care and moral support when I needed it most, which helped me to complete this work on time.

The support of the European Community Research Infrastructure Activity under FP6 “Structuring the European Research Area” program (CARE, contract number RII3-CT-2003-506395) is gratefully acknowledged.

On personal level, I would like to give special thanks to my parents for their affection and placing much importance on my education. I thank my parents-in-law for their unrestricted support and encouragement. I am blessed with the siblings giving me a wonderful family.

Finally, I would like to thank my best friend, colleague and husband, M. Tech. Chandra Shekhar Pandey for his great support and understanding during all my research work, and especially helping me to complete experiments till late night and even in the weekends. He always motivated me to work harder and do my best.